Radio Science Bulletin

ISSN 1024-4530

INTERNATIONAL
UNION OF
RADIO SCIENCE

UNION
RADIO-SCIENTIFIQUE
INTERNATIONALE

Vol. 2021, No. 378
September 2021

URSI, c/o Ghent University (INTEC)
Technologiepark - Zwijnaarde 126, B-9052 Gent (Belgium)

Contents

Cover: A Picture of W. Ross Stone, Assistant Secretary General for Publications and GASS and the Editor of the Radio Science Bulletin from 2001 until his death in March 2023.

Radio Science Bulletin Staff

Editor

W. R. Stone
Stoneware Limited
840 Armada Terrace
San Diego, CA 92106, USA
Tel: +1-619 222 1915, Fax: +1-619 222 1606
E-mail: r.stone@ieee.org

Editor-in-Chief

P. Van Daele
URSI Secretariat
Ghent University - INTEC
Technologiepark - Zwijnaarde 126
B-9052 Gent, BELGIUM
Tel: +32 9-264 33 20, Fax: +32 9-264 42 88
E-mail: Pet.VanDaele@UGent.be

Production Editor

I. Lievens
URSI Secretariat / Ghent University - INTEC
Technologiepark - Zwijnaarde 126
B-9052 Gent, BELGIUM
Tel: +32 9-264.33.20, Fax: +32 9-264.42.88
E-mail: ingeursi@ugent.be, info@ursi.org

Senior Associate Editor

A. Pellinen-Wannberg
Department of Physics
Umea University
BOX 812
SE-90187 Umea, SWEDEN
Tel: +46 90 786 74 92, Fax: +46 90 786 66 76
E-mail: asta.pellinen-wannberg@umu.se

Associate Editors, Commissions

Commission A

Amitava Sengupta
Department of Applied Sciences
The Northcap University, Sector 23 A, Gurgaon, Haryana
122017,India
E-mail: sengupta53@yahoo.com

Nosherwan Shoaib
Department of Electrical Engineering
National University of Sciences and Technology RIMMS,
H-12, Islamabad, Pakistan
E-mail: nosherwan.shoaib@seecs.edu.pk

Giovanna Signorile
INRiM (National Institute of Metrological Research)
Via Torrazza Piemonte 41, Turin, Italy
E-mail: g.signorile@inrim.it

Commission B

Henrik Wallén
Dept. Radio Science and Engineering
Aalto University
PO Box 13000, Otakaari 5 A, FI-00076 Aalto Finland
E-mail: henrik.wallen@aalto.fi

Dimitrios Tzarouchis
University of Pennsylvania
School of Engineering and Applied Science
220 South 33rd Street, 107 Towne Building Philadelphia,
PA 19104 USA
E-mail: dtz@seas.upenn.edu

Commission C

Pape Abdoulaye Fam
Dakar University, Senegal
E-mail: pafam@esp.sn

Ruisi He
State Key Lab of Rail Traffic Control and Safety
Beijing Jiaotong University
No. 3 Shangyuancun, Beijing 100044, China
E-mail: ruisi.he@bjtu.edu.cn

Alberto Tarable
CNR, Institute of Electronics, Information Engineering and Telecommunications
Corso Duca degli Abruzzi 24
10129 Torino, Italy
E-mail: alberto.tarable@ieiit.cnr.it

Commission D

Atsushi Kanno
Optical Access Technology Laboratory
Photonic ICT Research Center
Network Research Institute
National Institute of Information and Communications Technology
4-2-1 Nukui-kitamachi, Koganei
Tokyo 184-8795, Japan
E-mail: kanno@nict.go.jp

Commission E

Carlo Carobbi
Dipartimento di Ingegneria dell'Informazione
Università degli Studi di Firenze - UniFI
P.zza S.Marco, 4 - 50121 Firenze, Italy
E-mail: carlo.carobbi@unifi.it

Chaouki Kasmi
Directed Energy Research Center
Technology Innovation Institute
PO Box 9639, Masdar City
Abu Dhabi, United Arab Emirates
E-mail: Chaouki.Kasmi@tii.ae

Commission F

Swaroop Sahoo
Department of Electrical Engineering
Indian Institute of Technology Palakkad
Ahalia Integrated Campus
Kozhippara PO Palakkad, Kerala, India
E-mail: swaroop@iitpkd.ac.in

Commission G

Iwona Stanislawska
Polish Academy of Sciences
Space Research Centre
ul. Bartycka 18 A,00-716 Warsaw, Poland
E-mail: stanis@cbk.waw.pl

Commission H

Craig Rodger
Department of Physics
University of Otago
PO Box 56, Dunedin 9016, New Zealand
E-mail: craig.rodger@otago.ac.nz

Commission J

Richard Bradley
Technology Center
National Radio Astronomy Observatory
1180 Boxwood Estate Road
Charlottesville VA 22903, USA
E-mail: rbradley@nrao.edu

Commission K

Emily Porter
Electrical and Computer Engineering
University of Texas Austin
2501 Speedway, C0803
Austin, TX 78712 USA
E-mail: emily.e.porter@ieee.org

Associate Editors, Columns

Book Reviews

G. Trichopoulos
Electrical, Computer & Energy Engineering ISTB4 555D
Arizona State University
781 E Terrace Road, Tempe, AZ, 85287 USA
Tel: +1 (614) 364-2090
E-mail: gtrichop@asu.edu

Historical Papers

J. D. Mathews
Communications and Space Sciences Lab (CSSL)
The Pennsylvania State University
323A, EE East
University Park, PA 16802-2707, USA
Tel: +1(814) 777-5875, Fax: +1 814 863 8457
E-mail: JDMathews@psu.edu

Et Cetera

T. Akgül
Dept. of Electronics and Communications Engineering
Telecommunications Division
Istanbul Technical University
80626 Maslak Istanbul, TURKEY
Tel: +90 212 285 3605, Fax: +90 212 285 3565
E-mail: tayfunakgul@itu.edu.tr.

Women in Radio Science

A. Pellinen-Wannberg
Department of Physics and Swedish Institute of Space Physics
Umeå University
S-90187 Umeå, Sweden
Tel: +46 90 786 7492
E-mail: asta.pellinen-wannberg@umu.se

Ethically Speaking

R. L. Haupt
Colorado School of Mines
Brown Building 249
1510 Illinois Street, Golden, CO 80401 USA
Tel: +1 (303) 273 3721
E-mail: haupt@ieee.org

A. J. Shockley
E-mail: aj4317@gmail.com

Solution Box

Ö. Ergül
Department of Electrical and Electronics Engineering
Middle East Technical University
TR-06800, Ankara, Turkey
E-mail: ozgur.ergul@eee.metu.edu.tr

Telecommunications Health & Safety

J. C. Lin
University of Illinois at Chicago
851 South Morgan Street, M/C 154
Chicago, IL 60607-7053 USA
Tel: +1 312 413 1052, Fax: +1 312 996 6465
E-mail: lin@uic.edu

Historical Column

G. Pelosi
Department of Information Engineering
University of Florence
Via di S. Marta, 3, 50139 Florence, Italy
E-mail: giuseppe.pelosi@unifi.it

Early Career Representative Column

Nosherwan Shoaib
Research Institute for Microwave and Millimeter-Wave Studies (RIMMS)
School of Electrical Engineering and Computer Science (SEECS)
National University of Sciences and Technology (NUST)
H-12, Islamabad, Pakistan
E-mail: nosherwan.shoaib@seecs.edu.pk

Education Column

Madhu Chandra
Microwave Engineering and Electromagnetic Theory
Technische Universität Chemnitz
Reichenhainerstrasse 70
09126 Germany
E-mail: madhu.chandra@etit.tu-chemnitz.de

URSI Officers and Secretariat

Officers triennium 2020-2023

President

P. L. E. Uslenghi
Dept. of ECE (MC 154)
University of Illinois at Chicago 851
S. Morgan Street
Chicago, IL 60607-7053
USA
Tel: +1 312 996-6059
Fax: +1 312 996 8664
E-mail: uslenghi@uic.edu

Vice President

K. Kobayashi
Dept of Electrical, and Comm. Eng.
Chuo University
1-13-27 Kasuga, Bunkyo-ku
TOKYO, 112-8551
JAPAN
Tel. +81 3 3817 1846/69
Fax +81 3 3817 1847
E-mail kazuya@tamacc.chuo-u.ac.jp

Past President

M. Ando
Senior Executive Director
National Institute of Technology
701-2, Higashi Asakawa, Hachioji,
Tokyo 193-0834, Japan
Tel:+81-42-662-3123,
Fax: +81-42-662-3131
E-mail: ando@kosen-k.go.jp,
mando@antenna.ee.titech.ac.jp

Vice President

G. Manara
Dip. di Ingegn.
dell'Informazione
Universita di Pisa
Via G. Caruso 16
56122 Pisa
ITALY
Tel. +39-050-2217552
Fax +39-050-2217522
E-mail g.manara@iet.unipi.it

Secretary General

P. Van Daele
URSI Secretariat
Ghent University - INTEC
Technologiepark - Zwijnaarde 126
B-9052 Gent
BELGIUM
Tel: +32 9-264 33 20
Fax: +32 9-264 42 88
E-mail: Pet.VanDaele@UGent.be

Vice President

A. Sihvola
Electronic Science Department Aalto
University
School of Electrical Engineering
PO Box 13000
FI-00076 AALTO
FINLAND
Tel: +358 50 5871286
E-mail: Ari.Sihvola@aalto.fi

Vice President

P. Doherty
Boston College
Institute for Scientific Research,
885 Centre Street
Newton, MA 2459, USA
Tel. +1 617 552 8767
Fax +1 617 552 2818
E-mail Patricia.Doherty@bc.edu

Deceased 13 July 2022

Officers NEW triennium 2023-2026

At the GASS 2023, held in Sapporo, Japan (19-26 August 2023), the Board Members were chosen for the new triennium 2023-2026.

President

A. Sihvola
Electronic Science Department Aalto University
School of Electrical Engineering
PO Box 13000
FI-00076 AALTO
FINLAND
Tel: +358 50 5871286
E-mail: Ari.Sihvola@aalto.fi

Vice President

K. Kobayashi
Dept of Electrical, and Comm. Eng.
Chuo University
1-13-27 Kasuga, Bunkyo-ku
TOKYO, 112-8551
JAPAN
Tel. +81 3 3817 1846/69
Fax +81 3 3817 1847
E-mail kazuya@tamacc.chuo-u.ac.jp

Past President

P. L. E. Uslenghi
Dept. of ECE (MC 154)
University of Illinois at Chicago 851
S. Morgan Street
Chicago, IL 60607-7053
USA
Tel: +1 312 996-6059
Fax: +1 312 996 8664
E-mail: uslenghi@uic.edu

Vice President

G. Manara
Dip. di Ingegn.
dell'Informazione
Universita di Pisa
Via G. Caruso 16
56122 Pisa
ITALY
Tel. +39-050-2217552
Fax +39-050-2217522
E-mail g.manara@iet.unipi.it

Vice President

S. Salous
Department of Engineering
Durham University
Lower Mountjoy
South Road
Durham, DH13LE
UNITED KINGDOM
Tel: +44 1913342532
E-mail sana.salous@durham.ac.uk

Vice President

O. Santolik
Department of Space Physics
CAS
Bocni II 1401
141 31 Prague
CZECH REPUBLIC
Tel: +420 272 764 336
E-mail: os@ufa.cas.cz

Secretary General

P. Van Daele
URSI Secretariat
Ghent University - INTEC
Technologiepark - Zwijnaarde 126
B-9052 Gent
BELGIUM
Tel: +32 9-264 33 20
Fax: +32 9-264 42 88
E-mail: Pet.VanDaele@UGent.be

URSI Secretariat

Secretary General

P. Van Daele
URSI Secretariat
Ghent University - INTEC
Technologiepark - Zwijnaarde 126
B-9052 Gent
BELGIUM
Tel: +32 9-264 33 20
Fax: +32 9-264 42 88
E-mail: Pet.VanDaele@UGent.be

Assistant Secretary General AP-RASC

K. Kobayashi
Dept. of Electr and Commun. Eng,
Chuo University
1-13-27 Kasuga, Bunkyo-ku
Tokyo, 112-8551, JAPAN
Tel: +81 3 3817 1846/69
Fax: +81 3 3817 1847
E-mail: kazuya@tamacc.chuo-u.ac.jp

Assistant Secretary General

Stefan J. Wijnholds
Netherlands Institute for
Radio Astronomy
Oude Hoogeveensedijk 4
7991 PD Dwingeloo
The Netherlands
E-mail: wijnholds@astron.nl

Assistant Secretary General AT-RASC

W. Baan
Astron
Asserweg 45
9411 LP Beilen
THE NETHERLANDS
Tel: +31 521-595 773/100
Fax: +31 521-595 101
E-mail: baan@astron.nl

Assistant Secretary General Publications & GASS

W. R. Stone
840 Armada Terrace
San Diego, CA 92106
USA
Tel: +1-619 222 1915
Fax: +1-619 222 1606
E-mail: r.stone@ieee.org

Deceased March 2023

Executive Secretary

I. Heleu
URSI Secretariat
Ghent University - INTEC
Technologiepark - Zwijnaarde 126
B-9052 Gent
BELGIUM
Tel. +32 9-264.33.20
Fax +32 9-264.42.88
E-mail info@ursi.org

Congress Manager

I. Lievens
URSI Secretariat
Ghent University - INTEC
Technologiepark - Zwijnaarde 126
B-9052 Gent
BELGIUM
Tel: +32 9-264.33.20
Fax: +32 9-264.42.88
E-mail: ingeursi@ugent.be

URSI Secretariat NEW triennium 2023-2026

At the GASS 2023, held in Sapporo, Japan (19-26 August 2023), the Members of the Secretariat were chosen for the new triennium 2023-2026.

Secretary General

P. Van Daele
URSI Secretariat
Ghent University - INTEC
Technologiepark - Zwijnaarde 126
B-9052 Gent
BELGIUM
Tel: +32 9-264 33 20
Fax: +32 9-264 42 88
E-mail: Pet.VanDaele@UGent.be

Assistant Secretary General GASS & AP-RASC

K. Kobayashi
Dept. of Electr and Commun. Eng,
Chuo University
1-13-27 Kasuga, Bunkyo-ku
Tokyo, 112-8551, JAPAN
Tel: +81 3 3817 1846/69
Fax: +81 3 3817 1847
E-mail: kazuya@tamacc.chuo-u.ac.jp

Assistant Secretary General & AT-RASC

Stefan J. Wijnholds
Netherlands Institute for
Radio Astronomy
Oude Hoogeveensedijk 4
7991 PD Dwingeloo
The Netherlands
E-mail: wijnholds@astron.nl

Assistant Secretary General WIRS & ITU

S. Salous
Department of Engineering
Durham University
Lower Mountjoy
South Road
Durham, DH13LE
UNITED KINGDOM
Tel: +44 1913342532
E-mail sana.salous@durham.ac.uk

Assistant Secretary General Publications

P. L. E. Uslenghi
Dept. of ECE (MC 154)
University of Illinois at Chicago 851
S. Morgan Street
Chicago, IL 60607-7053
USA
Tel: +1 312 996-6059
Fax: +1 312 996 8664
E-mail: uslenghi@uic.edu

Associate Secretary General GASS

J. Volakis
College of Engineering and Computing
Florida International University
10555 W. Flagler Street
Miami, FL 33174
USA
Tel: +1 305.348.5338
E-mail: jvolakis@fiu.edu

Executive Secretary

I. Heleu
URSI Secretariat
Ghent University - INTEC
Technologiepark - Zwijnaarde 126
B-9052 Gent
BELGIUM
Tel. +32 9-264.33.20
Fax +32 9-264.42.88
E-mail info@ursi.org

Congress Manager

I. Lievens
URSI Secretariat
Ghent University - INTEC
Technologiepark - Zwijnaarde 126
B-9052 Gent
BELGIUM
Tel: +32 9-264.33.20
Fax: +32 9-264.42.88
E-mail: ingeursi@ugent.be

Announcement of the Final Issue of the RSB by the URSI Secretary General

Dear Colleagues, Dear Radioscientists,

All of us in the URSI community and beyond were shocked by the passing away of Dr. Ross Stone, the Editor of the Radio Science Bulletin, also serving as URSI Assistant Secretary General for GASS and Publications. Ross has been an URSI scientist for many decades and was committed to contribute and serve our community.

Because of Ross Stone's long illness, the Radio Science Bulletin was two years behind schedule, the last issue having been published in June 2021. Thus, the Radio Science Bulletin became in serious violation of the guidelines for indexing, which require timely publishing. After Ross Stone's death on 29 March 2023, the Board examined the possibility of bringing the Radio Science Bulletin up to date in a short time, but concluded that this solution was not feasible, both operationally and financially. Consequently, the Board decided to discontinue publication of the Radio Science Bulletin and accepted the offer by Kazuya Kobayashi to act as Interim Editor for this last issue of the Radio Science Bulletin.

The origins of the Radio Science Bulletin lay in the merger of 2 URSI publications, namely, the "Bulletin" and "The Radio Scientist" under a new name "INFORMATION BULLETIN D'INFORMATION". This decision was taken at the General Assembly in Kyoto in 1993. The name quickly changed into "Radio Science Bulletin" in 1994 with Prof. Paul Delogne as editor.

Dr. Ross Stone became editor for the Radio Science Bulletin in September 2001. Shortly after that, in September 2002, the Radio Science Bulletin was published electronically and distributed via e-mail and made available for download from the URSI Website. The Secretariat is currently working on making all previous issues of the Radio Science Bulletin, which were at that time printed on paper and distributed through mail, also available for download.

The Board have now decided to replace the Radio Science Bulletin with a much simpler URSI Newsletter, that will not be indexed and will be edited by the Secretary General with the assistance of his staff. The Newsletter will be distributed electronically to all member committees and individual members. It will contain informational items, such as minutes of the Board, reports of working groups, calendar of conferences, etc.

The 1993 Kyoto General Assembly lead to the start of the "Radio Science Bulletin" and now 30 years later, shortly after our 2023 General Assembly in Sapporo, the final issue is being published. The Radio Science Bulletin has been one of the major communication channels within our community and has offered an extra and unique channel for many of our URSI scientists to publish results. We hope you will enjoy this final issue, but as in many situations, we have to be flexible and adapt to new circumstances and new challenges.

Together with the Board, we hope we will be able to fulfill the communication needs with the new URSI Newsletter,

Peter Van Daele
URSI Secretary General

In Memoriam: W. Ross Stone
26 August 1947 - 29 March 2023

It is with great sadness that we inform all radio scientists of the passing of Ross Stone, Editor of the *URSI Radio Science Bulletin.* Ross was born in San Diego, California, USA on August 26, 1947. He grew up and went to school in San Diego, where he received his BA in geophysics in 1967 at the age of 19, and his M.Sc. and Ph.D. degrees in applied physics in 1973 and 1978, all from the University of California, San Diego. He died in San Diego on March 29, 2023, after a long illness.

Ross was the president of Stoneware Limited, a consulting engineering company which he founded in 1976. He also served as chief scientist and on the governing boards of several engineering companies and was an Adjunct Professor at the Beijing Jiaotong University.. He devoted an enormous amount of time and energy to the development of professional societies in all areas of electrical and computer engineering. In addition to URSI, his contributions to IEEE, EuCAP, ISAP and MAPE have left a permanent, beneficial imprint on those organizations. Ross was the inventor of the holographic radio camera and the editor of several books. Among the many honors he received are Fellow of URSI, Fellow of the IEEE, Fellow of the Electromagnetics Academy, Fellow of the Chinese Institute of Electronics, recipient of the IEEE Third Millennium Medal and of the IEEE AP-S Distinguished Achievement Award, and Honorary Life Member of the Administrative Committee of the IEEE Antennas and Propagation Society. He was the EIC of the *IEEE AP-S Newsletter* from 1984 and transformed it into the *IEEE AP-S Magazine* in 1990, therefrom editing it until 2014.

Ross was a member of USNC-URSI Commissions A, B, E, F and G and served on many committees within the USNC. Among the many positions which he held in international URSI, he was Assistant Secretary General for Publications and GASS and the Editor of the *Radio Science Bulletin* from 2001 until his death. Through years of pain and hospital stays, Ross fought hard to regain his health, never lost hope, never waivered in his commitments and never relinquished any of the many chores which he had taken on to benefit professional societies.

Ross' passing has left a large void among his family, friends and colleagues. Those who knew him will cherish the memory of, and miss, his kindness, congeniality, sense of humor, willingness to help, and encyclopedic knowledge. He will be remembered fondly for a very long time. The deepest condolences of the URSI Board, of the URSI Secretariat, of the staff of the *Radio Science Bulletin,* and of the entire radio science community go to his wife Sue, his daughter Michele, and their family.

Piergiorgio L. E. Uslenghi
URSI President
Peter Van Daele
URSI Secretary General

Maxwell Foundation Newsletter Available

The latest editions of the James Clerk Maxwell Foundation's *Newsletter* are now available. Issue No. 17 contains an article by Dusa McDuff and David Forfar, "Some Advances in Pure Mathematics Made in the 19th Century." Issue No. 18 contains an article by Naomi C. Robertson, "An Introduction to Black Holes." The issues are available for free at:

https://clerkmaxwellfoundation.org/Newsletter_2022_Summer_V17.pdf

https://clerkmaxwellfoundation.org/Newsletter_2022_Summer_V18.pdf

Correction

Two figure captions in the article "In Memoriam: Oleg Alexandrovich Tretyakov" (*URSI Radio Science Bulletin*, 377, June 2021, pp. 60-61) contained mis-prints. The correct captions are as follows:

Figure 1. Oleg A. Tretyakov on December 19th, 2016.

Figure 3. Oleg A. Tretyakov and his wife, Tetyana Tretyakova, lived in Istanbul from 1998 to 2022, until he passed away.

Introduction to the Special Issue of the Student Paper Contest of the 15th Congress of the URSI Portuguese National Meeting 2021

With the aim of encouraging young Portuguese authors, ANACOM sponsored the Best Student Paper Award, given to the three best papers presented by students (first authors) at the 15th Congress of the URSI Portuguese Committee, which was held on November 24, 2021, using a hybrid model.

Subject of the conferrence was "Environmental sustainability in the use of radio spectrum". Sustainable development is a concept that combines economic and social development with preservation of the environment, providing a response to current needs without undermining the capacity of future generations to satisfy their own needs.

Following the presentations made during the morning session, the jury, chaired by António Topa (Instituto de Telecomunicações - IT) and including Pedro Cruz (Bosch) and José Pedro Borrego (ANACOM), agreed unanimously to award the prize to:

- 1st place - Mário António Patrício Carreira Vala from Instituto Superior Técnico and IT-Leiria, with the paper "Complex Permittivity Study of a Pinus Pinaster Needle Bed on Fire".
- 2nd place - Tiago Emanuel da Silva Oliveira from Instituto Politécnico de Leiria, with the paper "A Waning Crescent Quasi-Yagi Microstrip Antenna for Wireless Sensing Networks".
- 3rd place - José Miguel Neves from Universidade do Porto, with the paper "Design and Experimental Evaluation of Square Loop CPW Feed Patch Antenna at 100 GHz".

These awards were presented at the closing session of the Congress by ANACOM's Board Member, Sandro Mendonça, and the Chair of the URSI Portuguese Committee, Luísa Mendes.

This special issue includes the papers of the three awarded authors and two other papers also presented in the Best Student Paper Award session:

- A preventive Maintenance Approach to optimize Fault Management using Machine Learning
  Marcio Filipe Godinho Pereira, Instituto Superior de Engenharia de Lisboa
- Study of radio coverage for IoT networks in the subway tunnels
  Catarina Sousa, Instituto Superior de Engenharia de Lisboa

Figure 1. Winners of the Best Student Paper Award; Luísa Mendes, Chair of the URSI . Portuguese Committee; Sandro Mendonça, Member of ANACOM's Board of Directors

Complex Permittivity Study of a Pinus Pinaster Needle Bed on Fire

Mário Vala[1,3], Stefânia Faria[1,2,3], Nuno Leonor[1,2], João M. Felício[1,3,4], Carlos Fernandes[1,3], Carlos Salema[1,3], and Rafael Caldeirinha[1,2]

[1]Instituto de Telecomunicações
Leiria, Portugal
E-mail: mario.vala@co.it.pt

[2]Polytechnic of Leiria
Leiria, Portugal

[3]Instituto Superior Técnico
University of Lisbon
Lisbon, Portugal

[4]Centro de Investigação Naval
Escola Naval
Almada, Portugal

Abstract

In this paper, a range of complex permittivity values, estimated from a *Pinus Pinaster* fuel bed on fire is presented. The Fire Dynamics Simulator (FDS) was used to model the fire environment and the Cold Plasma Model (CPM) was applied to evaluate the complex permittivities of such turbulent media. The retrieved values served as input parameters describing the propagation medium, enabling a full-wave analysis based on the Finite-Difference Time-Domain (FDTD) method to evaluate and ascertain the impact of a weakly ionised plasma generated during vegetation combustion on radiowave propagation. Comparisons were obtained against two other methods, namely the Transmission-Line Method (TLM) and the Full-Stack (FS) technique, as a way to reduce the computational time. These analyses yielded attenuation values up to 6 dB for the simulated scenario, in which good agreement among techniques was obtained. Preliminary results clearly indicated that fire may degrade communications in real fire situations.

1. Introduction

Wildfires have been a constant problem all around the world. Depending on the fuel area dimensions and weather conditions, they can rapidly spread from the initial source and cause enormous damage to communities and natural landscapes and heritages [1]. During wildfire-suppression operations, radiowave communication systems are massively employed by firefighters and civil protection personnel. In this case, the technology usually operates in frequency bands lower than mobile network frequencies and allows fast and independent communications between radio terminals [2]. Such communications are termed mission-critical push-to-talk (MC-PTP) communications.

However, extensive fire environments may have the effect of suppressing radiowaves in the Very- and Ultra-High frequency ranges. Such conditions may impact the capability for coordinating and controlling wildfire outbreaks by firefighters, as reported, e.g., during the Dwellingup (1961) and Lara (1969) bushfire disasters in Australia [3].

Initial research has been performed on the estimation of the impact of fires on signal propagation. This was the case in [4] and [5], where authors demonstrated that a controlled pine-litter fire could cause signal losses between 1.6 dB and 5.8 dB, especially in the VHF and UHF frequency bands. In [6], the dependency of the attenuation caused by fire with frequency was studied, where values of 5.43 dB and 0.26 dB were measured at 360 MHz and 400 MHz, respectively.

One of the causes of signal attenuation in wildfires is the formation of an ionized plume in the fire region. This plume, also defined as a plasma, is composed of free electrons released from alkali and alkaline-earth metals (A-AEM) during vegetation combustion [7]. The generated plume can thus be electrically characterized and modeled by the Cold Plasma Model (CPM) [8]. The Cold Plasma Model requires previous knowledge of the collision-frequency and electron-density profiles from the environment in order to calculate the medium's permittivity and, later, attenuation values.

In this paper, a fire spreading in a flat terrain is modeled considering two ignition lines with different incident angles over a uniformly *Pinus Pinaster* needle bed using the Fire Dynamics Simulator (FDS). From the results, the impact of the estimated permittivity values was analyzed on radiowave propagation using the Finite-Difference Time-Domain model (FDTD). A delay and an advance in the wave's electric field was detected, in addition to the excess attenuation introduced by the fire. Fire parameters such as the heat-release rate (HRR) and mass-loss rate (MLR) are presented.

This paper is organized as follows. In Section 2, the Cold Plasma Model is presented. Fire modeling using the Fire Dynamics Simulator is defined in Section 3, and the electromagnetic analysis of the estimated complex permittivity applying the Finite-Difference Time-Domain model, the Transmission-Line Method, and the Full-Stack technique are demonstrated in Section 4. Final considerations are presented in Section 5.

2. The Cold Plasma Model and Radiowave Absorption

As previously mentioned, the input parameters to the Cold Plasma Model are the electron density of a plasma and the effective collision frequency of the air molecules present in the medium [9]. The electron density can be calculated using Equation (1) [10]:

$$N_e = \left(K_1 N_a\right)^{1/2}\left[\left(1+\frac{K_1}{4N_a}\right)^{1/2}-\left(\frac{K_1}{4N_a}\right)^{1/2}\right]\left[\mathrm{m}^{-3}\right] \quad (1)$$

with K_1 being the ionization equilibrium constant, given by Saha's equation [10]:

$$K_1 = 2\frac{g_i}{g_0}\frac{\left(2\pi m_e kT\right)^{3/2}}{h^3}e^{-\frac{eV_i}{kT}}, \quad (2)$$

where g_i and g_0 are the internal partition functions of ions and neutrons, respectively; m_e is the electron mass $(9.109\times10^{-31}\ \mathrm{kg})$; k is Boltzmann's constant $(1.381\times10^{-23}\ \mathrm{J/K})$; h is Planck's constant $(6.626\times10^{-34}\ \mathrm{Js})$; e is the electron charge $(1.602\times10^{-19}\ \mathrm{C})$; T is the absolute temperature; and V_i is the ionization energy.

Still referring to Equation (1), N_a is the total density $\left(\mathrm{m}^{-3}\right)$ of alkali and alkaline-earth particles, ions, and atoms, given by [10]

$$N_a = n_0 + n_e = 7.335\times10^{27}\frac{\xi}{T}, \quad (3)$$

where n_0 and n_e are the densities per cubic meter of neutral particles and electrons, respectively, and ξ is the pressure expressed in atmospheres (atm) applied by the alkali and alkaline-earth at a given temperature, T.

When considering the electron-neutral collisions as the dominant interactions, the effective collision frequency between these particles can be computed by Equation (4) [4]:

$$\nu_{eff} = 7.33\times10^{3} N_m a^2\sqrt{T}\left[\mathrm{s}^{-1}\right], \quad (4)$$

where N_m is the density of air molecules, a is the radius of air element molecules, and T is the absolute temperature.

From the electron density and the effective collision frequency, it is possible to estimate the medium's complex permittivity as in [11]:

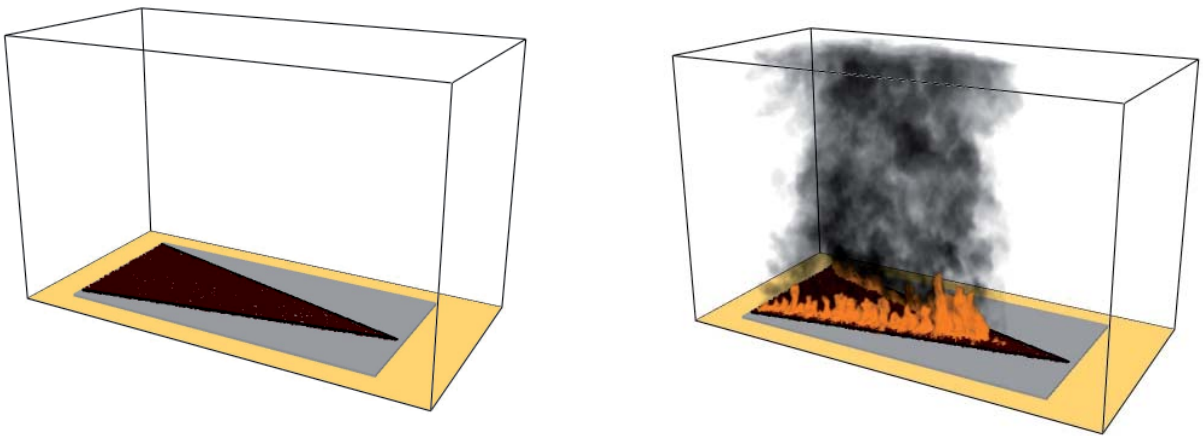

Figure 1. The designed scenario in the Fire Dynamics Simulator for (a) $t = 0$ s; b) $t = 49.68$ s.

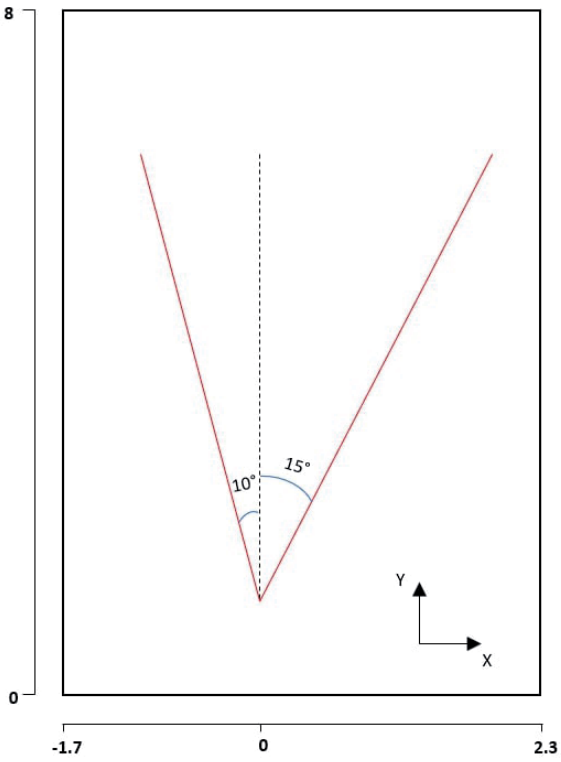

Figure 2. The design of the structure.

$$\varepsilon = \varepsilon_0 \varepsilon_r = \varepsilon_0 \left[1 + \frac{\omega_p^2}{\omega\left(i\nu_{eff} - \omega\right)} \right], \tag{5}$$

where ω is the electric field angular frequency and ω_p^2 is the plasma frequency given by Equation (6) [12]:

$$\omega_p^2 = \frac{N_e e^2}{m_e \varepsilon_0}. \tag{6}$$

Still referring to Equation 6, e is the electron charge $(1.602\times10^{-19}\ \text{C})$, m_e is the electron mass $(9.109\times10^{-31}\ \text{kg})$, and ε_0 is the vacuum permittivity $(8.854\cdot10^{-12}\ \text{F/m})$.

3. Fire Modeling

The fire environment was modeled using the Fire Dynamics Simulator (FDS) [13]. This is a computational-fluid-dynamics software program from which both temperature and density profiles of the medium were extracted in order to characterize the generated plasma. Fire parameters such as heat-release rate, mass-loss rate, and fuel consumption were also assessed for a typical flat terrain consumed by two distinct fire fronts.

3.1 Flat Terrain Design

A triangular *Pinus Pinaster* needle bed was designed, as depicted in Figure 1. The fuel-bed mass was 5.72 kg and the alkali and alkaline-earth pine needle content was established as $K = 0.45\%$, $Ca = 0.25\%$ and $Mg = 0.13\%$ The full computational volume of $4\ \text{m}\times8\ \text{m}\times5\ \text{m}$ was discretized in cubic unit cells of $2.5\ \text{cm}\times2.5\ \text{cm}\times2.5\ \text{cm}$ generating a matrix of $160\times320\times200$ cells. Each cell corresponded to an independent permittivity value that was calculated punctually from the Fire Dynamics Simulator parameters. The simulation ran 109 s.

The structure designed is illustrated in more detail in Figure 2. A linear burner was allocated along each of the red lines and the fuel was uniformly distributed inside the triangle, taking into consideration the informed angle disposition.

This scenario was implemented in order to analyze the impact of the junction of two independent fire fronts on radiowave propagation and, subsequently, to estimate the complex permittivities of such media from their electron densities and effective collision frequencies.

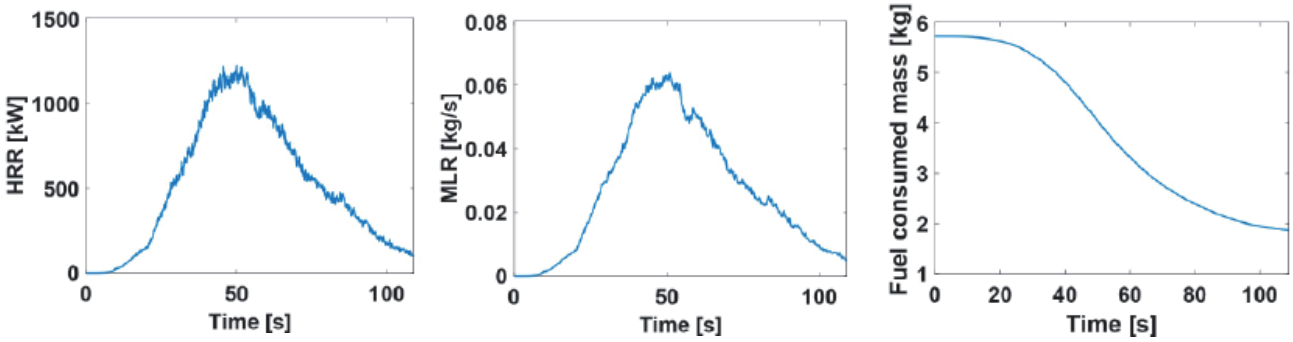

Figure 3. The flat-terrain fire parameters: (a) The heat- release rate (HRR); (b) the mass-loss rate (MLR); and (c) the fuel consumption.

3.2 Fire Parameters

From the results obtained, a temperature increase was observed when the junction of the two fire fronts happened. The heat-release rate, mass-loss rate, and fuel heap consumption parameters are presented in Figure 3. At the end of the simulation (109 s), there was still 1.85 kg of biomass to be consumed.

4. Electromagnetic Simulation and Results Analysis

4.1 Finite-Difference Time-Domain Method

In the previous sections, how the fire propagated through a flat terrain and how to obtain the complex permittivities of fire media were explained. However, it is important to ascertain how this variation in permittivities of the fire environment may affect the propagation of radio signals. Since the majority of the scenario at each given time instant is comprised of cells with the dielectric properties of air, there is no necessity to individually analyze each cell. For this particular study, only the ε_r of the cells with the maximum and minimum magnitudes of complex permittivities were considered, as the remaining cells would have an impact in between these two values. A Fire Dynamics Simulator simulation time instant of 49.68 s was considered, where values of complex ε_r ranging from $0.98-0.09j$ to $0.85-1.25j$ were observed. For ease of understanding, these values will henceforth be identified as *dielectric1* and *dielectric2*, respectively.

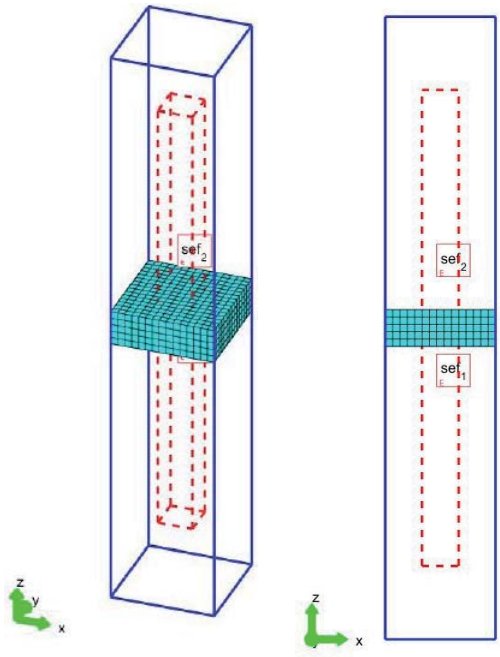

Figure 4. The FDTD simulation environment: (a) top view, and (b) side view.

To achieve and quantize the impact of this variation of permittivities in a propagating wave, a set of simulations using the Finite-Difference Time-Domain (FDTD) method was carried out [12]. The FDTD method provides a full-wave electromagnetic analysis by solving Maxwell's equations, allowing the calculation of the electric and magnetic fields in the time domain.

The simulation environment considered for this set of simulations is presented in Figure 4. From this figure, it can be seen that the scenario was composed of only one dielectric slab with dimensions of $7.5\ \text{cm} \times 7.5\ \text{cm} \times 2.5\ \text{cm}$ and two electric-field probes. The field probes were placed below and above the dielectric slab to register the electric fields reflected and transmitted through the slab, respectively. Moreover, a plane wave with a Gaussian waveform traveling in the positive *z* direction was used as excitation for the simulation.

Three different simulations were performed, in which only the dielectric properties of the slab were altered. In the first simulation, the slab was defined as having the same characteristics as air ($\varepsilon_r = 1$ and conductivity, $\sigma = 0$) to serve as a reference. The remaining two simulations were performed with the characteristics of *dielectric1* and *dielectric2* previously described. However, in order to characterize a dielectric material in the FDTD simulation, its permittivity, ε_r, and conductivity, σ, are needed. Both these values could be obtained from the complex permittivity: ε_r is the real part, while σ is obtained using Equation (7):

$$\sigma = \left|\varepsilon r'' \omega \varepsilon_0\right|, \tag{7}$$

where $\varepsilon r''$ is the imaginary part of the complex permittivity, ω is the angular frequency, and ε_0 is the vacuum permittivity. Using this formula, and considering a frequency of 700 MHz (the frequency used to calculate the permittivities from the Fire Dynamics Simulator data), the conductivities of *dielectric1* and *dielectric2* were 0.004 S/m and 0.049 S/m, respectively.

After the simulations were performed, the results were divided into two distinct analyses: one in the time domain and the other in the frequency domain. The results of the time domain are presented in Figure 5 for both probes. Figure 5a is the result corresponding to the electric-field probe placed below the slab that shows the electric field reflected, and Figure 5b corresponds to the probe above the slab that measured the electric field measured after the wave was transmitted through the dielectric. As can be seen from the reflected electric fields, in the simulation with *dielectric2* the values were higher than the remaining values, due to the impedance mismatch in the air-slab interface. There was electric field that was reflected on *dielectric1*, but since the impedance mismatch of the interface air-substrate was not as pronounced as in the previous case,

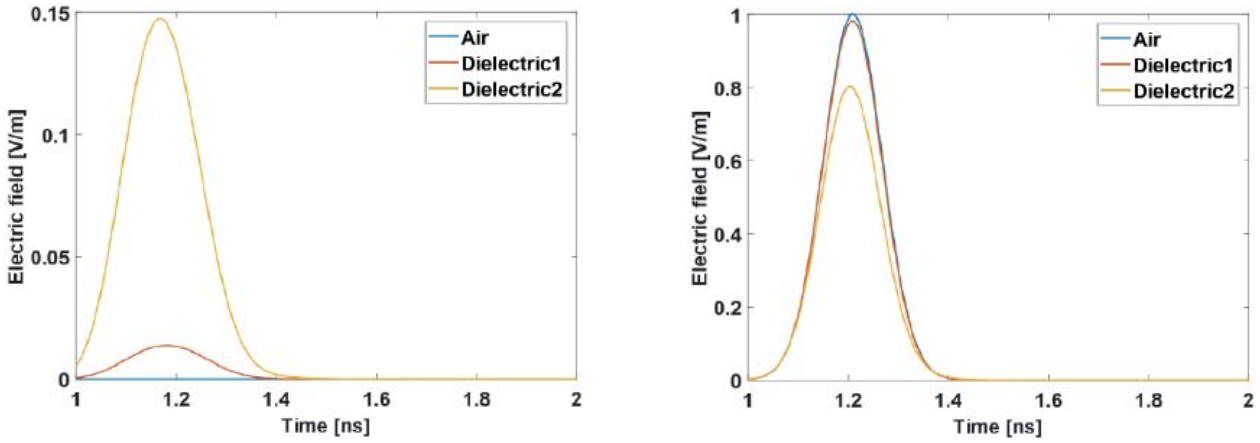

Figure 5. The electric fields in the FDTD simulation: (a) the reflected electric fields below the dielectric slab, and (b) the electric fields measured above the dielectric slab.

this value was smaller. Lastly, and as expected, there was no signal reflected by the slab in the case in which air was considered, since there was no impedance mismatch of the media.

In terms of the results present in Figure 5b, it could be seen that the curves corresponding to the air and *dielectric1* were very similar in terms of amplitude, since the ε_r were similar and the conductivities were close to zero. However, in the simulation with *dielectric2*, differences in amplitude were verified due to the higher conductivity of this material.

The results of the frequency analysis are presented in Figure 6. As could be seen, when air was used for the substrate the transmission coefficient was 0 dB as expected, since there was no impedance mismatch. When

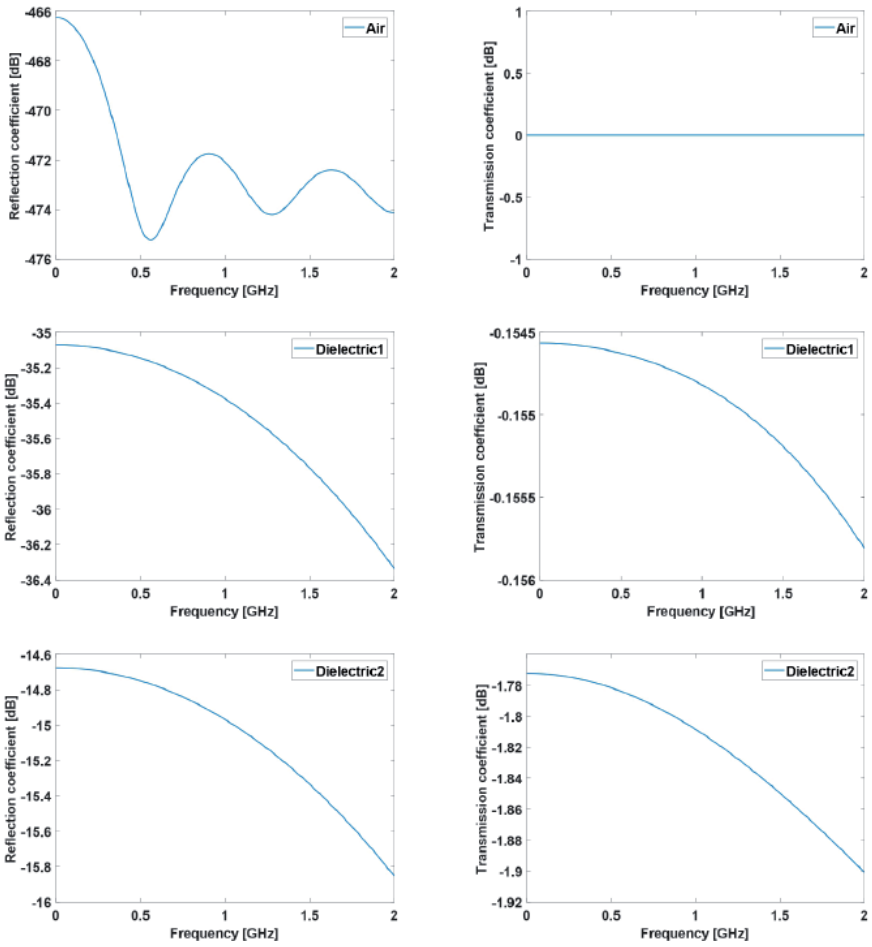

Figure 6. The reflection and transmission coefficients: (a - b) air dielectric, (c - d) *dielectric1*, and (e - f) *dielectric2*.

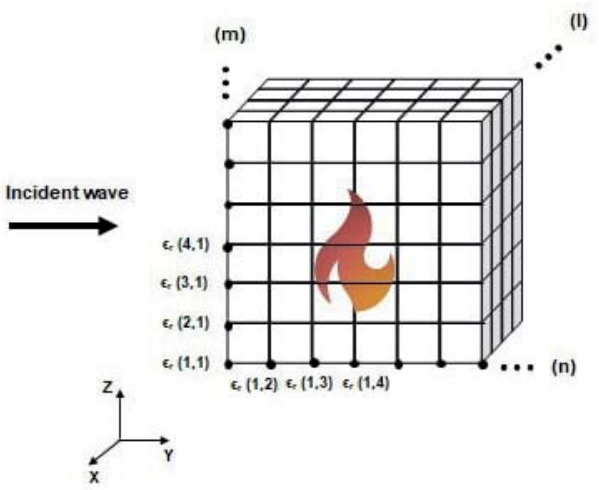

Figure 7. An illustration of the per-tube analysis.

the permittivity and the conductivity of the material started to increase, as in *dielectric1*, the transmission coefficient started to decrease, reaching 0.15 dB at 700 MHz. This value was even higher when *dielectric2* was considered, achieving an attenuation of 1.8 dB at 700 MHz. Inversely, the higher the conductivity of the medium, the higher the reflection coefficient, leading to maximum values of −14.8 dB at 700 MHz for the simulation where *dielectric2* was considered.

4.2 Transmission-Line Method and Full-Stack Technique

In order to evaluate the overall attenuation introduced by fire for the time step considered in the previous section, the Transmission-Line Method (TLM) was applied. By implementing this method, it was possible to study the transmission and reflection coefficients in the propagation path on a per-tube basis. This method was chosen due to its low computational cost and time consumption.

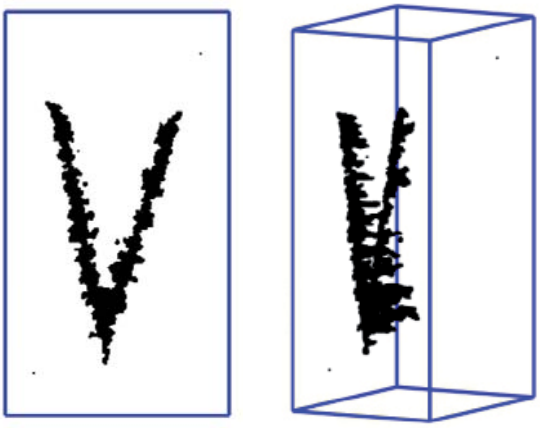

Figure 8. Permittivity cells from the simulated environment: (a) top view and (b) side view.

For this analysis, consider Figure 7, which represents the simulated geometry divided into cubic unit cells. The volume designed was split into $m \times n$ longitudinal dielectric tubes in the *y*-axis direction, assuming wave propagation also along the *y* axis. Each voxel considered is illustrated as a black dot in the corner of each cell and presented uniform electrical properties in electrical permittivity and conductivity that varied according to fire and fuel conditions.

Figure 8 illustrates the voxels with permittivities that contributed most to the excess-loss estimation. These points were mainly located in the fire and burning gas regions. Top and side views are presented.

In this work, the TLM was applied to recursively calculate the S_{21} parameter of a transmission-line cascade. By ensuring impedance matching at the multiple dielectric slabs, propagation and marching matrices were calculated. Here, the ABCD matrix method for a lossy medium was considered, which is given for each slab [15] by

$$\begin{bmatrix} A_{m,n} & B_{m,n} \\ C_{m,n} & D_{m,n} \end{bmatrix}$$

$$= \begin{bmatrix} \cosh\left(\gamma_{m,n} l_{m,n}\right) & jZ_{m,n} \sinh\left(\gamma_{m,n} l_{m,n}\right) \\ jY_{m,n} \sinh\left(\gamma_{m,n} l_{m,n}\right) & \cosh\left(\gamma_{m,n} l_{m,n}\right) \end{bmatrix}, \quad (8)$$

where Y and Z are the admittance and impedance of the voxel, l is the length of the slab, and γ is the propagation constant, given by

$$\gamma_{m,n} = j\omega\sqrt{\mu_0 \varepsilon_0 \varepsilon_{r_{m,n}}}, \quad (9)$$

where ω is the angular frequency, $\varepsilon_{r_{m,n}}$ is the relative permittivity of each voxel, and μ_0 and ε_0 are the vacuum permeability and permittivity, respectively.

When multiplying the matrices of each voxel, a final ABCD matrix is obtained for the entire tube:

$$\begin{bmatrix} A & B \\ C & D \end{bmatrix}_m = \prod_{i=1}^{n} \begin{bmatrix} A & B \\ C & D \end{bmatrix}_{m,n}, \quad (10)$$

and the transmission coefficient, S_{21}, is finally obtained [15] as

$$S_{21} = \frac{2}{A + B/Z_0 + CZ_0 + D}, \quad (11)$$

where Z_0 is the free-space impedance.

For this scenario, each tube was made up of 320 voxels and the time instant of $t = 49.68$ s was once more considered. The projection plane, which is the plane view at the end of the simulated volume, was used as the reference in order to compute the excess loss introduced by fire. The estimated result is illustrated in Figure 9. Results are shown for heights up to 1 m in order to highlight attenuation values. From the results, it was observed that even though this was a small-scale scenario where the total fuel mass available was approximately 5.72 kg, attenuation values around 6 dB were quantized. The highest values could be seen at approximately 0.3 m above the fuel bed.

The assessed results were also compared with an empirical homemade model based on the superposition theorem, called the Full-Stack (FS) technique [6]. In this procedure, no coupling effects between adjacent voxels were considered and the cumulative attenuation was obtained by summing the attenuation of each voxel that comprised the tube, the final result being denormalized by its physical dimension along the y axis. In this case, the attenuation constant was given in dB/m, as

$$\alpha_{\mathrm{dB}} = 20\log_{10}(e)\,\Re\left\{\gamma_{m,n}\right\}. \qquad (12)$$

Figure 10 presents the Full Stack results and showed that both methods were in good agreement, indicating that wildfires may significantly impact radiowave communications.

5. Conclusions

In this work the junction of two distinct fire fonts and its impact on radiowave propagation were studied. The fire environment was modeled using the Fire Dynamics Simulator and a range of complex permittivities of the medium were estimated considering the Cold Plasma Model for a 700 MHz signal. The influence of maximum

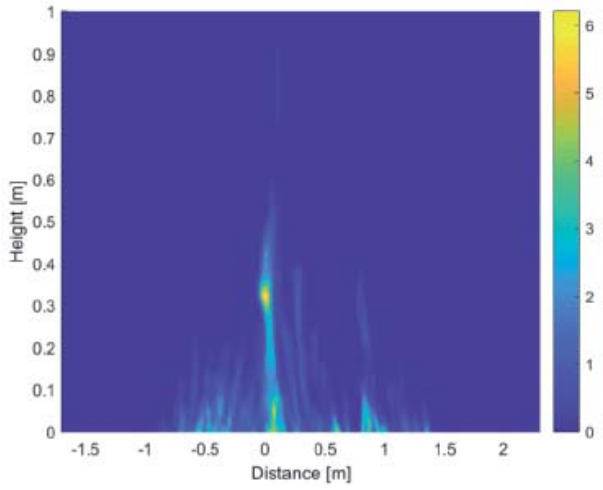

Figure 10. The total attenuation from a per-tube analysis using the Full-Stack technique at $t = 49.68$ s.

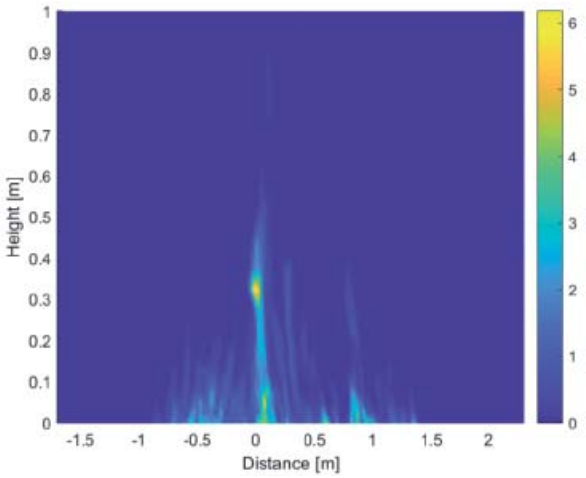

Figure 9. The total attenuation from a per-tube analysis using the Transmission-Line Method at $t = 49.68$ s.

and minimum values of complex permittivities was assessed using the FDTD method, with an aim to understand the impact of a weakly ionized plasma's electric characteristics on a propagating electromagnetic wave.

A set of simulations using an FDTD simulation tool was performed in which the effects of different permittivities found in a fire environment were assessed, both in the time and frequency domains. The time-domain analysis showed an attenuation of the electric fields that was higher for higher values of conductivity. These results were better analyzed in the frequency analysis, where a maximum of 1.8 dB of attenuation was found.

Besides the FDTD study, an overall excess attenuation in the projection plane was estimated using two different methods: the Transmission-Line Method and the Full-Stack technique. From both methods, an attenuation of up to 1 dB/m was quantified.

These results showed that the permittivities found in fire environments lead to the attenuation of the propagating radiowave. If there is a big cluster of such materials concentrated around a certain area, it can even affect the communications between the professionals present in the terrain.

Future work will address the simulation and the assessment of complex permittivity values for a number of different scenarios and configurations, such as small-scale, bent terrain, etc. Measurements of attenuation in a controlled fire environment, using different vegetation as fuel, are also planned to experimentally verify the results presented herein.

6. Acknowledgements

This work was part of the projects RESCuE-TOOL (PCIF/SSI/0194/2017) and UID/EEA/50008/2021, both funded by the Portuguese Government, Portuguese Foun-

dation for Science and Technology (FCT). We gratefully thank Prof. Xavier Viegas and the Forest Fire Research Laboratory team for all support in the forest fire area of expertise.

7. References

1. M. D. Chinthaka, N. H. Malka, K. Ramamohanarao, B. Moran, and P. Farrell, "The Signal Propagation Effects on IEEE 802.15.4 Radio Link in Fire Environment," 2010 Fifth International Conference on Information and Automation for Sustainability, 2010, pp. 411-414.

2. A. Aguiar, A. Navarro, A. Rodrigues, C. Fernandes, C. Salema, J. Sanguino, N. B. d. Carvalho, and R. Caldeirinha, "Estudo do funcionamento do SIRESP - Parte I," Instituto de Telecomunicações de Portugal, Tech. Rep., 2017.

3. K. M. Mphale, "Radiowave Propagation Measurements and Prediction in Bushfires," PhD dissertation, School of Mathematical and Physical Sciences - James Cook University, 2008.

4. K. Mphale and M. Heron, "Microwave Measurement of Electron Density and Collision Frequency of a Pine Fire," *J. Phys. D: Appl. Phys*, **40**, May 2007, pp. 2818-2825.

5. K. Mphale, M. Jacob, and M. Heron, "Prediction and Measurement of Electron Density and Collision Frequency in a Weakly Ionised Pine Fire," *International Journal of Infrared and Millimeter Waves*, **28**, 3, 2007, pp. 251-262.

6. Y. Wu Li, H. Yong Yuan, Y. Lu, R. Feng Xu, M. Fu, M. Yuan, and L. Han, "Experimental Studies of Electromagnetic Wave Attenuation by Flame and Smoke in Structure Fire," *Fire Technology*, **53**, 1, July 2016, pp. 5-27.

7. S. Faria, M. Vala, P. Coimbra, N. Leonor, J. Felício, C. A. Fernandes, C. Salema, and R. F. S. Caldeirinha, "Radiowave Propagation Modelling of Dual Wildfire Front Spreading Over Hilly Terrain at 700 MHz," *2021 Telecoms Conference (ConfTELE)*, 2021, pp. 1-6.

8. J. Boan, "Radio Propagation in Fire Environments," PhD dissertation, University of Adelaide, School of Electrical and Electronic Engineering, 2009.

9. S. Faria, M. Vala, P. Coimbra, J. Felício, N. Leonor, C. Fernandes, C. Salema, and R. Caldeirinha, "Comparative Study of Computational Electromagnetics Applied to Radiowave Propagation in Wildfires," *2020 XXXIIIrd General Assembly and Scientific Symposium of the International Union of Radio Science*, 2020, pp. 1-4.

10. L. S. Frost, "Conductivity of Seeded Atmospheric Pressure Plasmas," *Journal of Applied Physics*, **32**, 10, 1961, pp. 2029-2036. Available: https://doi.org/10.1063/1.1728283

11. K. G. Budden, *The Propagation of Radio Waves: The Theory of Radio Waves of Low Power in the Ionosphere and Magnetosphere*, Cambridge, Cambridge University Press, 1985.

12. K. Mphale and M. Heron, "Plant Alkali Content and Radio Wave Communication Efficiency in High Intensity Savanna Wildfires," *Journal of Atmospheric and Solar-Terrestrial Physics*, **69**, 04, 2007, p. 471-484.

13. K. McGrattan, R. McDermott, S. Hostikka, J. Floyd, and M. Vanella, *Fire Dynamics Simulator, Sixth Edition*, 2018.

14. A. Z. Elsherbeni and V. Demir, *The Finite-Difference Time-Domain in Electromagnetics*, London, Institution of Engineering and Technology, 2015.

15. D. Pozar, *Microwave Engineering, Fourth Edition*, New York, Wiley, 2011.

An IoT Radio Coverage Survey in Subway Tunnels

Catarina Sousa[1], Cláudia Alves[1], João Casaleiro[1,2], António Serrador[1]

[1]Departamento de Engenharia Eletrónica Telecomunicações e Computadores
Instituto Superior de Eng. de Lisboa (ISEL), *Portugal*

[2] Centre of Technology and Systems (CTS-UNINOVA), Portugal

Abstract

It is becoming increasingly relevant to use wireless communications in subway tunnels to gather sensors data for advanced maintenance and security purposes. In this work, we present a propagation survey over IoT radio bands using LoRa modulation in Lisbon's Subway. Several scenarios such as straight and curved tunnels, bifurcations, and partial tunnel obstructions were considered. Measurements were taken with LoRa modulation with a transmitter and receiver set to 868 MHz with spreading factors from 7 to 12. The transmit power was 14 dBm, and half-wave whip antennas with vertical polarization were used. Based on the measurement results and the COST-231 two-slope propagation model, a loss factor of 58.5 dB/km and 80.5 dB/km, were obtained respectively, for unobstructed curved and bifurcation tunnels. An extra attenuation of 10 dB was observed for partial tunnel obstruction by one loaded convoy. The results of this study indicate that using a legal transmission power and for straight and curved tunnels, communication can be maintained for distances exceeding one kilometre. *Keywords—Subway tunnels, propagation model, LoRa, IoT.*

1. Introduction

Subway operators are switching from traditional maintenance methods, such as preventative, run-to-failure, or a combination of the two, to predictive maintenance techniques. Predictive maintenance is an invaluable subject for subway operators because it allows for the early detection of faulty components, minimizes failures and unplanned downtime. An infrastructure and train network of low-power wireless sensors is usually installed to collect the relevant data. A wireless network is required to forward data to a central point where it can be processed. The Internet of Things (IoT) technologies are well suited to transmitting data in this manner.

In the literature several propagation models for tunnels are available. There are studies focusing on a specific technology, or service, and others on propagation models. Several works focus on the propagation in tunnels for mobile communications [1-5]. Other studies are focussed on the propagation and deployment of wireless networks to provide internet access to passengers [9-11, 14-17]. Recently, train-to-train communications have been reported with interesting results [18].

There are already mobile communication systems installed in subways worldwide, and Wi-Fi networks are also available, but the access points are typically located in the stations or on board the trains to enable passengers to access the internet. The main disadvantage of using these networks to gather sensory data is that radio transceivers consume a lot of power, in comparison with the LoRa transceivers.

The aim of this work is to determine the coverage range of LoRa gateways considering the tunnel's propagation characteristics and the antennas installed in the tunnel's walls. From the available propagation models for tunnels [12] we selected the two-slope model which fitted well with the measurements.

The paper is organized as follows: in Section II, a brief review of the two-slope empirical model and the required parameters are presented. The measurement setup, the developed firmware and measured scenarios are presented in Section III. Finally, concluding remarks are given in Section IV.

2. Two-slope Model

The two-slope empirical model was proposed for radio propagation in tunnels in [1], a detailed description is available in [1, 12, 19, 20]. The model determines the path loss based on the Received Signal Strength Indicator (RSSI), Pr, and the reference power level, P0, obtained near the transmitter. The path loss is divided in the near- and far-regions. A linear regression is applied to the measurements of the received power in the far region to obtain the model parameters from which one can estimate the path loss by

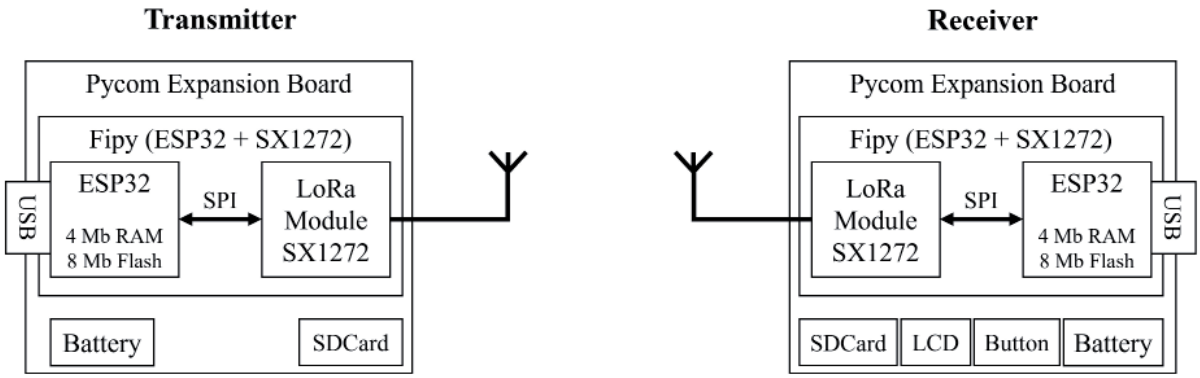

Figure 1 . Block diagram of the transmitter (left), and receiver (right).

$$P_r(d) = P_0(d_0) - d \times \alpha \quad (1)$$

where P_r and P_0 are the received power level at a distance d and d_0, respectively, away from de transmitter antenna, and α is the loss factor per unit length, i.e. dB/km. The loss factor is higher for the near-region due to the several propagation modes and is lower in the far-region due to the less propagation modes [12]. Loss factor is a parameter that is dependent on several factors, such as signal frequency, tunnel cross section dimensions, forms, and obstruction percentage.

The transition from near to far region is not smooth and is referred to has the break point, or critical distance, and is obtained by

$$d_{critic} = D^2/\lambda \quad (2)$$

where D is the tunnel cross section largest dimension and λ is the wavelength of the transmitted RF signal [2].

The two-slope model is suitable for line of sight and when the transmitter and receiver antennas are installed several wavelengths away from the tunnel floor and walls [12]. However, for practical reasons the transmitter and receiver antennas must be mounted near the walls. Sensors will be installed along the tunnel walls and floor, and near the tracks, which makes the use of directive antennas unfeasible.

3. Measurements

Measurements are performed using two low-cost devices, having each a LoRa transceiver (based on the Semtech SX1272), a whip antenna for the 868 MHz band, a microcontroller (Espressif ESP32) with 4 MB of RAM and 8 MB of Flash and an memory card (SDCard) to store the measurements, as shown in Figure 1.

3.1 Measurement setup

The transmitter is fixed and installed at approximately 1.8 m height from the tunnel floor and at 30 cm from the tunnel's wall, as shown in Figure 2(a) and Figure 3. The receiver is portable, and for each measurement the receiver was positioned approximately 1 m and 1.5 m respectively

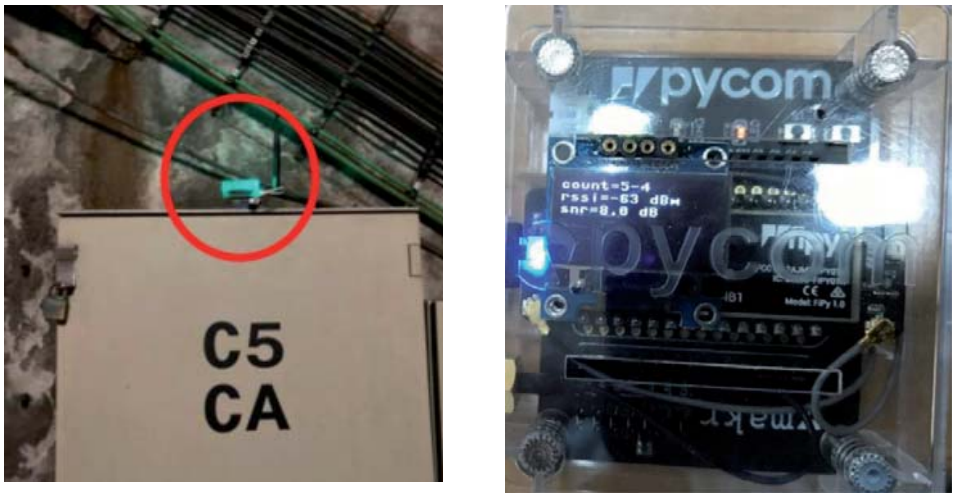

Figure 2. Transmitter (a), highlighted by red circle, installed, and transmitting and a photo of the receiver (b).

Figure 3. Photo of the transmitter.

from the tunnel floor and walls. A photo of the receiver is shown in Figure 2(b). Both devices were powered by a commercial power bank through the USB connection.

The transmitter firmware configures the LoRa transceiver for a transmitter power of 14 dBm, bandwidth of 125 kHz and to broadcast indefinitely a cycle of 10 LoRa packets with a spreading factor (SF) of 12 followed by 10 packets with a spreading factor of 7. To receive packets in the correct order and correct spreading factor, the receiver must synchronize itself with the transmitter. This synchronization is done automatically by the developed firmware and in accordance with the state machine shown in Figure 4.

The receiver starts in the IDLE state where all the peripherals are asleep to save energy. After pressing the onboard button, S1, the device wakes up and switches to RX_SF12 state. This is where it configures the LoRa radio to accept packets with a SF of 12 and wait to receive 10 packets in sequence. After receiving 10 LoRa packets the device switches to RX_SF7 state where it stays until it collects the last 10 packets.

Finally, after receiving a total of 20 packets, the data is stored on the memory card and the device returns to the IDLE state. To consider the scenario where it is not possible to receive packets, in either of the two states, a timeout timer of 20 seconds is triggered. This timer is implemented to abort the cycle, dump the data, and return to the IDLE state. Furthermore, an RGB LED set to Red, Blue, and Green respectively for the IDLE, RX_SF12, and RX_SF7 states is used. This is used to allow the person carrying the receiver to evaluate whether the measurement is complete.

The transmitter broadcasts LoRa packets with a relative counter between 1 and 10 and a general counter which is always increasing. After reaching the value 10, the relative counter is reset, and the spread factor is changed. Therefore, 10 packets are sent cyclically in each spreading factor until the module is shut down or restarted. The receiver stores the counters, RSSI and SNR values of each packet received and the timeout events on the memory card.

3.2 Measured Scenarios

Measurements were taken in the following scenarios:

- Tunnel with bifurcation empty;
- Curved tunnel empty;
- Straight tunnel empty and partial obstructed.

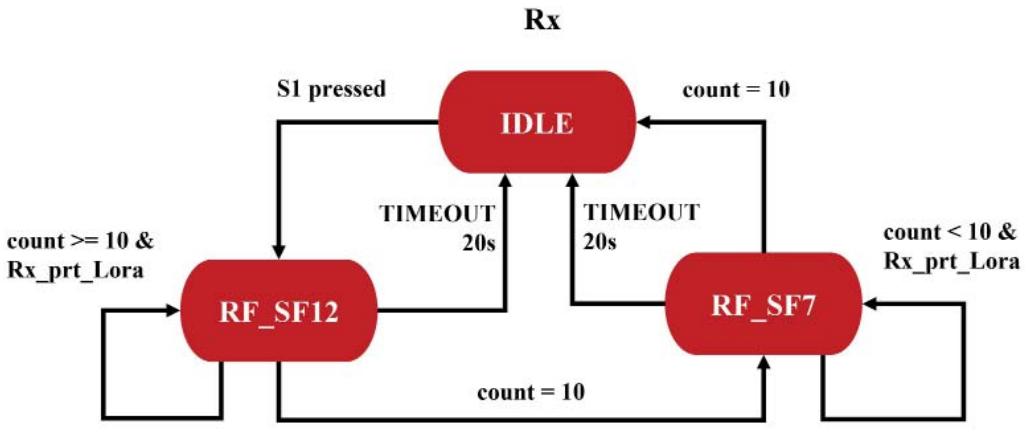

Figure 4. Diagram of the receiver state machine.

Figure 5. Photo of the bifurcation at "Carnide" station (a), and oval tunnel (b).

Table 1 presents the receiver and transmitter configuration for all previous scenarios.

3.2.1 Empty tunnel with a bifurcation

Measurements was done between Lisbon Metro stations: "Carnide" and "Colégio Militar". The transmitter was installed near the "Carnide" station. The tunnel from "Carnide" has a rectangular geometry of 13.5 x 6.0 m (width x height). Approximately 80 meters into the tunnel, two oval tunnels with a smooth curve and a 4.5 x 6 m geometry appear, as shown in Figure 5. We measured along a distance of 650 meters into the left tunnel, with 50 meter intervals between measurements. The measurement results are shown in Figure 6. A total of 600 measurements were taken, 10 measurements at each distance and for each spreading factor. To determine the exact breakpoint, measurements were taken 10 m apart near the transmitter. According to the data, the break point is about 20 meters from the transmitter. The parameters of the model are derived from the linear regression of the data and displayed graphically, as shown in Figure 6. The loss factor is α = 55,8 dB/km and the P_0 (d_0 = 20 m) = -55.1 dBm.

3.2.2 Empty curved tunnel

Measurement was done between "Carnide" and "Pontinha" stations. The transmitter was installed near the "Carnide" station. The tunnel leading from "Carnide" to "Pontinha" is 800 m long and with a curvature radius of 87.5 m. Along the length of the tunnel, the geometry changes from oval to rectangular to oval again, at 300 and 600 m respectively. In the oval sections the dimensions are 8.3 x 8.3 m and in the rectangular sections, 7.9 x 4.0 m.

The measurement results are shown in Figure 7. A total of 340 measurements were taken, 10 measurements at each distance and for each spreading factor. The model's parameters are derived from the linear regression of the data. The loss factor is α = 80.5 dB/km and the P_0 (d_0 = 100 m) = -48.2 dBm. As expected, the results for both spreading factors are identical.

3.2.3 Straight tunnel empty and partial obstructed

The measurement was made between the stations "Anjos" and "Intendente". The tunnel is 250 m long, straight, and both transmitter and receiver were stationary on the nearest stations' ledges.

A total of 50 measurements were taken on two scenarios: an empty tunnel and in an obstructed tunnel by one loaded convoy. Based on the measurements, the RSSI median are presented in Table 2, from which one can conclude that a single loaded convoy increases attenuation approximately by 10 dB.

Table 1. Receiver and Transmitter Equipment and Configuration

	TX	***RX***
Frequency	868 MHz	
Modulation	LoRa (SF=7, SF=12)	
Bandwidth	125 kHz	
Transmit Power	14 dBm	-
Receiver Sensitivy	-	-120 dBm (SF=7) -132 dBm (SF=12)
Antenna		
Type	λ/2 Whip Antenna	
Polarization	Linear Vertical	
Frequency band	868 MHz	

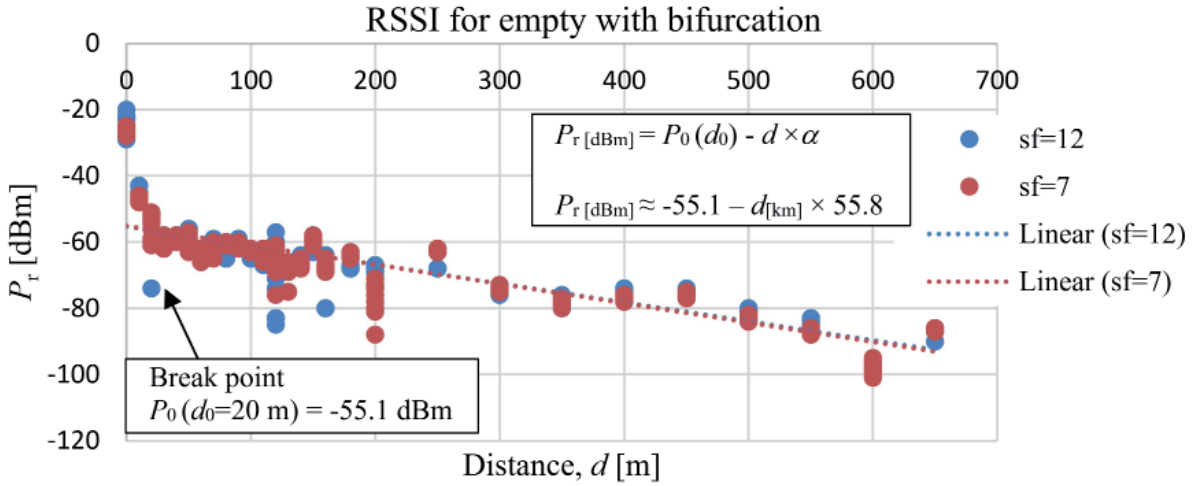

Figure 6. Measured RSSI values along the tunnel for SF=7 (red) and SF=12 (blue).

4. Conclusions

This work confirms the feasibility of using low-cost devices to obtain and measure the path loss, in locations and environments with difficult access and complexity for installing conventional RF measurement equipment. The two-slope model is also validated for measurements near the tunnel walls and floor.

Table 2 Median RSSI values between "Anjos" and "Intendente"

Tunnel	RSSI [dBm] SF=12	RSSI [dBm] SF=7
Empty	-85	-87
Partially Obstructed	-96	-95

For straight or slightly curved tunnels, the loss factor is -55.8 dB/km, which allows communication ranges over 1.2 km assuming a SF of 12 and a receiver sensitivity of -132 dBm.

Since the loss factor for curved tunnels is 80.5 dB/km, a maximum range of 1 km is expected, assuming the most optimistic case of an empty tunnel, a SF = 12 and the receiver sensitivity of -132 dBm.

A loaded convoy obstructing the tunnel has an impact on the overall attenuation of approximately 10 dB. In addition to continuing the investigation, it will be interesting to measure the impact of obstructing the tunnel completely with two convoys.

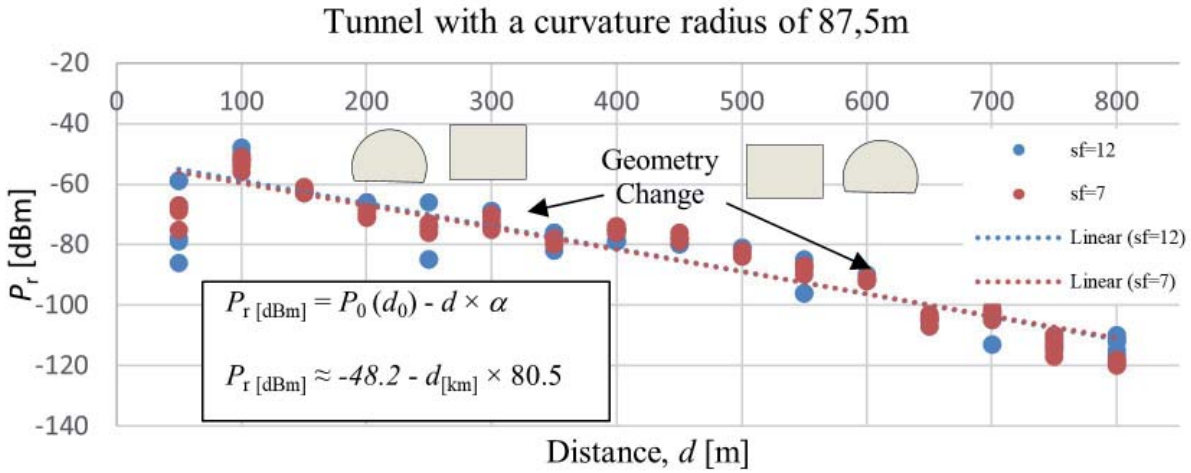

Figure 7. RSSI values along the curved tunnel for SF=7 and SF=12.

6. Acknowledgements

The authors acknowledge the *Metropolitano de Lisboa* for providing both technical and human resources for the development of this work. Special thanks to Tomé Canas and Rui Rodrigues, for their technical discussions, availability, sympathy, and patience while in the tunnels.

7. References

1. H. Xia, H. L. Bertoni, L. R. Maciel, A. Lindsay-Stewart and R. Rowe, "Radio propagation characteristics for line-of-sight microcellular and personal communications," in IEEE Transactions on Antennas and Propagation, vol. 41, no. 10, pp. 1439-1447, Oct. 1993, doi: 10.1109/8.247785.

2. T. Klemenschits and E. Bonek, "Radio coverage of road tunnels at 900 and 1800 MHz by discrete antennas," 5th IEEE International Symposium on Personal, Indoor and Mobile Radio Communications, Wireless Networks - Catching the Mobile Future., 1994, pp. 411-415 vol.2, doi: 10.1109/WNCMF.1994.529121.

3. S. Betrencourt, M. Lienard, P. Degauque and D. Degardin, "Mobile communication in road tunnels: influence of the traffic conditions on the channel characteristics," 2000 10th Mediterranean Electrotechnical Conf. Information Tech. and Electrotechnology for the Mediterranean Countries. Proceedings. MeleCon 2000, pp. 432-435 vol.1, doi: 10.1109/MELCON.2000.880458.

4. Y. P. Zhang, "Novel model for propagation loss prediction in tunnels," in IEEE Transactions on Vehicular Technology, vol. 52, no. 5, pp. 1308-1314, Sept. 2003, doi: 10.1109/TVT.2003.816647.

5. Z. changsen and M. Yan, "Effects of cross section of mine tunnel on the propagation characteristics of UHF radio wave," 2006 7th International Symposium on Antennas, Propagation & EM Theory, 2006, pp. 1-5, doi: 10.1109/ISAPE.2006.353521.

6. K. Guan, Z. Zhong, B. Ai and C. Briso-Rodríguez, "Statistic modeling for propagation in tunnels based on distributed antenna systems," 2013 IEEE Antennas and Propagation Society International Symposium (APSURSI), 2013, pp. 1920-1921, doi: 10.1109/APS.2013.6711618.

7. Hrovat, Andrej & Kandus, Gorazd & Javornik, Tomaz. (2010). Four-slope channel model for path loss prediction in tunnels at 400 MHz. Microwaves, Antennas & Propagation, IET. 4. 571 - 582. doi: 10.1049/iet-map.2009.0159.

8. Z. Chang-sen and G. Li-fang, "Research on propagation characteristics of electromagnetic wave in tunnels with arbitrary cross sections," 2010 2nd International Conf. on Future Computer and Communication, 2010, pp. V1-22-V1-25, doi: 10.1109/ICFCC.2010.5497844.

9. R. He, Z. Zhong and C. Briso, "Broadband Channel Long Delay Cluster Measurements and Analysis at 2.4GHz in Subway Tunnels," 2011 IEEE 73rd Vehicular Technology Conference (VTC Spring), 2011, pp. 1-5, doi: 10.1109/VETECS.2011.5956539.

10. J. Ferrer-Coll, P. Ängskog, H. Shabai, J. Chilo and P. Stenumgaard, "Analysis of wireless communications in underground tunnels for industrial use," IECON 2012 - 38th Annual Conference on IEEE Industrial Electronics Society, 2012, pp. 3216-3220, doi: 10.1109/IECON.2012.6389383.

11. K. Guan, Z. Zhong, J. I. Alonso and C. Briso-Rodriguez, "Measurement of Distributed Antenna Systems at 2.4 GHz in a Realistic Subway Tunnel Environment," in IEEE Transactions on Vehicular Technology, vol. 61, no. 2, pp. 834-837, Feb. 2012, doi: 10.1109/TVT.2011.2178623.

12. A. Hrovat, G. Kandus and T. Javornik, "A Survey of Radio Propagation Modeling for Tunnels," in IEEE Communications Surveys & Tutorials, vol. 16, no. 2, pp. 658-669, Second Quarter 2014, doi: 10.1109/SURV.2013.091213.00175.

13. J. Moreno, J. M. Riera, L. d. Haro and C. Rodriguez, "A survey on future railway radio communications services: challenges and opportunities," in IEEE Communications Magazine, vol. 53, no. 10, pp. 62-68, October 2015, doi: 10.1109/MCOM.2015.7295465.

14. K. Guan et al., "Measurements and Analysis of Large-Scale Fading Characteristics in Curved Subway Tunnels at 920 MHz, 2400 MHz, and 5705 MHz," in IEEE Transactions on Intelligent Transportation Systems, vol. 16, no. 5, pp. 2393-2405, Oct. 2015, doi: 10.1109/TITS.2015.2404851.

15. J. Li, Y. Zhao, J. Zhang, R. Jiang, C. Tao and Z. Tan, "Radio channel measurements and analysis at 2.4/5GHz in subway tunnels," in China Communications, vol. 12, no. 1, pp. 36-45, Jan. 2015, doi: 10.1109/CC.2015.7084382.

16. G. S. Ching, S. Nishida, A. Okuno and Y. Kishiki, "Radio propagation simulation and measurement inside a curved and sloped subway tunnel," 2016 International Symposium on Antennas and Propagation (ISAP), 2016, pp. 210-211.

17.X. Zhang, N. Sood and C. D. Sarris, "Fast Radio-Wave Propagation Modeling in Tunnels With a Hybrid Vector Parabolic Equation/Waveguide Mode Theory Method," in IEEE Transactions on Antennas and Propagation, vol. 66, no. 12, pp. 6540-6551, Dec. 2018, doi: 10.1109/TAP.2018.2864344.

18.C. Briso-Rodríguez, P. Fratilescu and Y. Xu, "Path Loss Modeling for Train-to-Train Communications in Subway Tunnels at 900/2400 MHz," in IEEE Antennas and Wireless Propagation Letters, vol. 18, no. 6, pp. 1164-1168, June 2019, doi: 10.1109/LAWP.2019.2911406.

19. Hrovat, Andrej & Kandus, Gorazd & Javornik, Tomaz. (2012). Path loss analyses in tunnels and underground corridors. International journal of communications. 6. 136-144.

20. E. Bonek: "Tunnels, Corridors, and Other Special Environments"; in: "COST Action 231: Digital mobile radio towards future generation systems", E. Damosso, L. Correira (eds.); European Union Publications, Brüssel, 1999, 190 – 207. ISBN: 9282854167.

Antenna Element Operating at 100 GHz

J.M. Neves[1], L.M. Pessoa[1], H.M. Salgado[1]

[1]INESC TEC and Faculty of Engineering, University of Porto, Porto, Portugal
henrique.salgado@inesctec.pt

Abstract

In this work, a novel patch antenna fed by a CPW square loop feed, was design in HFSS to work at a centre frequency of 100 GHz, having a minimum requirement of at least 5 percent of fractional bandwidth. An end launch connector, up to 110 GHz, was used for measurement purposes, imposing the design of a GCPW-to-CPW transition, as well as a TRL calibration kit. The antenna and calibration kit were fabricated in RT/duroid 5880 substrate with 0.127 mm of thickness. The experimentally obtained -10 dB impedance bandwidth was 6.7 GHz (versus 7.66 GHz simulated) and the measured peak gain at 100 GHz was 6.3 dBi (versus 6.1 dBi simulated).
Keywords—*Patch antenna, 100 GHz, square loop feed, GCPW (Grounded Coplanar Waveguide), CPW (Coplanar Waveguide), TRL, calibration, RT/duroid 5880.*

1. Introduction

In recent years, due to an exponential growth in wireless traffic data yet again, the need for higher bit rates has resurfaced. In the 4G to 5G transition, there was a move towards millimetre wave spectrum motivated by the need for higher bandwidth. Now the trend towards 6G is to move to even higher zones of the frequency spectrum, into the sub- terahertz (sub-THz) region, in order to mitigate the spectrum scarcity and capacity limitations of current wireless communication systems [1].

While rigorous scientific research and development in sub-THz devices and systems is still in progress, it is expected that it will have a significant societal impact, with applications ranging from wireless communications to sensing domains, including biomedical, radar and security systems.

In [2], a silicon-based micro-machined Benzocyclobutene-cavity patch antenna and two arrays were developed at 100 GHz, where the antenna element presented a 2.8 GHz -10 dB bandwidth and a 6.7 dBi peak gain. Furthermore in [3], a 94 GHz double-folded slot antenna was manufactured on a high-resistivity silicon substrate, fed by a CPW transmission line and backed by a dielectric lens, measured from 90 to 100 GHz, providing a radiation pattern with side lobes below -15dB. An on-chip Quasi-Yagi multi-layered antenna in [4] was integrated on a low resistivity silicon substrate and manufactured by a post-back-end-of-line process, having obtained a 5.7 dBi gain at 100 GHz and a -6 dB impedance bandwidth within 89-104 GHz frequency range. As such, antenna designs targeting the sub-THz region generally involve complex manufacturing processes with multi-layer configurations, in this paper we propose to achieve a more cost effective and less complex manufacture process. This led us to solutions that avoided the use of a multi-layered substrate configuration.

In this work, given the advantages that coplanar waveguide (CPW) have over microstrip configurations at high frequencies, an antenna element fed by a CPW structure is proposed in order to evaluate its performance at an operation frequency of 100 GHz, which was selected since this frequency is located within a limited band that exhibits a low atmospheric attenuation of EM waves [5] and has been considered as part of the research in 6G systems. This approach was considered, given that, at higher frequencies, where radiation loss dominates, justifies the need for more expensive alternatives such as multi-layered substrate structures, other more complex feeding methods such as stripline or SIW, or even the use of non-commercially available substrate materials. This antenna element aims to avoid such expensive alternatives and it explores the use of a single substrate layer through the application of uniplanar transmission lines such as CPW, to evaluate its performance, efficiency and viability in the sub-Terahertz domain.

This paper is structured in the following way: After the introduction, in Section II, the design of the components that form the antenna element are shown and explained, followed by the design process behind the TRL calibration kit. Lastly, in Section III, a direct comparison between simulated and measured S11 and radiation pattern of the antenna element is performed.

2. Design of the Antenna Element

2.1 Patch Antenna Fed By a Square Loop Feed

Using the theoretical values obtained from formulas for the patch antenna and the quarter-wavelength

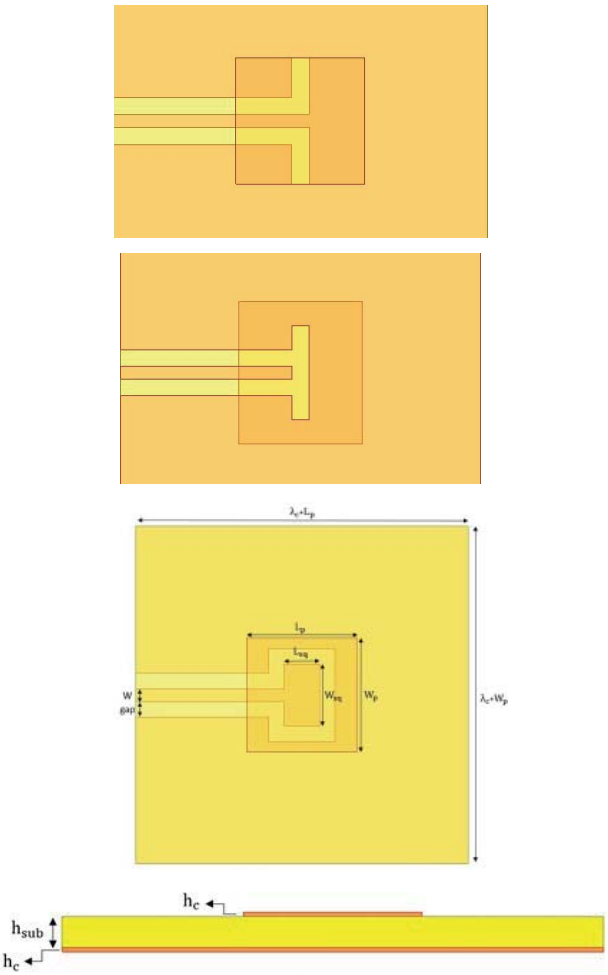

Figure 1. Schematic of the patch antenna (top view) fed by: a) inductive CPW feed, b) capacitive CPW feed, c) square loop CPW feed and d) side view of all feed types.

transformer in [6] [7], and for both the CPW and GCPW transmission lines in [8], a starting point for the dimensions of all the components was achieved, followed by a process of optimization through simulations, consisting of parametric sweeps of each variable. Given the implementation of a single substrate layer, and in order to obtain a high radiation efficiency and wide bandwidth [9], a thin Rogers RT/duroid 5880 substrate was selected, with a thickness of 0.127 mm and dielectric constant of 2.2.

For this design, three forms of antenna feeding were considered, taking advantage of the CPW feed line type, those being: inductive feed (CPW short-end structure – Figure1 (a)), capacitive feed (CPW open-end structure - Figure 1 (b)) [10] and square loop feed (Figure 1 (c)) [11]. All three of these feeding types were modeled and simulated using a commercial finite element method solver for electromagnetic structures named HFSS, from ANSYS. As seen in Figure 2 (a), only the square loop feed (blue solid line) presents a desirable minimum bandwidth of at least 5% fractional bandwidth (97.5 – 102.5 GHz). When comparing all three mentioned feed structures, the square loop feed structure showed a more symmetrical radiation

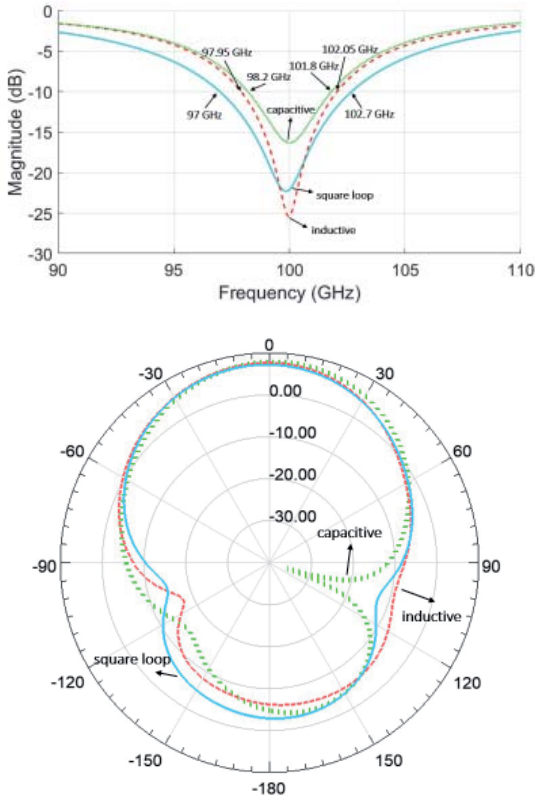

Figure 2. Simulated reflection coefficient (in dB) (a) and simulated radiation pattern (in dBi) (b) of the patch antenna types from Fig. 1 (inductive feed – red long dashed line, capacitive feed – green dotted line and square loop feed – blue solid line).

pattern, the trade-off being a lower front-to-back ratio and a slightly lower gain value, as seen in Figure2 (b) (inductive feed: 7.2 dBi, capacitive feed: 7.83 dBi and square loop feed: 7.6 dBi – simulated gain values at ($\theta = 0^0$). The simulation results of the full antenna element (seen in Figure 5) provide a S11 with a -10 dB impedance bandwidth of 7.66 GHz, and with a resonant dip of -34.97 dB at 100 GHz (see Figure 11.).

It is worth mentioning that it is important that the CPW feed is completely covered by the patch antenna, to maximize the electromagnetic coupling efficiency [12]. A substrate height of 0.127 mm was chosen as a starting value, to minimize the radiation losses from the feed line [13]. However, if the chosen value of the substrate height was not enough to provide the minimum required bandwidth, then the following available value of height of the Rogers RT/duroid 5880 series would need to be used (h=0.254 mm). The dimensions of the final design are given in Table 1.

2.2 GCPW-CPW Feed Line

In this sub-section, a description of the feed line, from the GCPW line where the connector is attached, to the CPW line that connects to the square loop feed (from Figure 1

Table 1. Variable Values For The Patch Antenna And The Square Loop Feed

Variable	Values (mm)
W	0.08138
gap	0.105
W_p	0.76
L_p	0.742
W_{sq}	0.411
L_{sq}	0.235
λ_c	1.5
h_{sub}	0.127
h_c	0.018

(c)) is given. A schematic of the line, top and bottom views is shown in Figure 3, along with the reference number of the different line sections.

The connector to be used for the measurement of the full antenna element is a 1.0 mm jack (female) end launch connector (DC up to 110 GHz), model 2492-04A-6, from Southwest Microwave, to be connected to a 50 Ω GCPW line (section 1 in Figure 3). The lines represented in section 3 (GCPW) and 4 (CPW) are chosen to have an impedance of 90 Ω, due to their similarity in line width and gap values, in order to avoid abrupt value variations when the changeover between the GCPW and CPW transmission lines occur. In section 2, a quarter-wavelength transformer was used to adapt de 50 Ω GCPW line to the 90 Ω GCPW line. The GCPW-CPW transition (section 3 to section 4) was implemented by a gradual tampering of the bottom ground plane of the GCPW side until it reached a width limit value, considering the manufacturing design constraints/limits. In section 5 of the feed line, another quarter-wavelength transformer, in the CPW side, was used to adapt the 90 Ω CPW line to the CPW line leading into the square loop feed (112.6 Ω CPW line). The values of the impedance as well as, line width and gap values of each section are presented in Table II. The impedance values were initially obtained using the PathWave Design Software LineCalc tool, from Keysight Technologies, which afterwards were optimized using HFSS software.

Table 2. Variable Values For The Various Line Sections Of The GCPW-CPW Feed Line Structure

Line Section	Impedance Value (Ω)	Line Width (mm)	Line Gap (mm)
1 (GCPW)	50	0.325	0.1
2 (GCPW)	67.08	0.185	0.1
3 (GCPW)	90	0.091	0.1
4 (CPW)	90	0.135	0.08
5 (CPW)	100.66	0.084	0.08
6 (CPW)	112.6	0.081	0.105

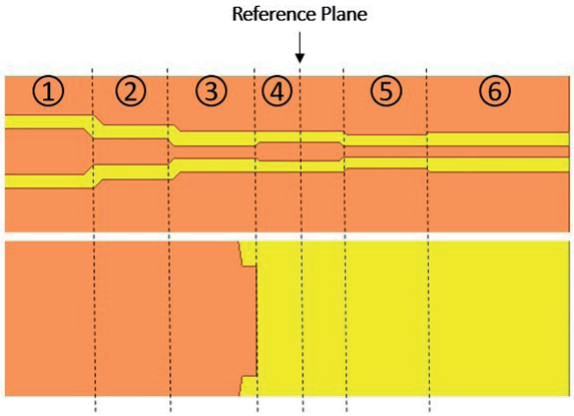

Figure 3. Zoomed-in schematic of GCPW-CPW feed line leading into the antenna feed structure (view of the line above and view of the ground plane below).

The simulated S-parameters of the entire GCPW-CPW feed structure, described previously, are shown in Figure 4, for the frequency band of interest (from 90 GHz to 110 GHz).

2.3 Overall Antenna Element Analysis

Figure 5 shows a schematic of the full antenna designed in HFSS, which includes an approximate model for the 1 mm end launch connector. Upon simulation it was observed, as seen in Figure 6 (radiation pattern in dashed red), that initially, without any line length extension, the radiation pattern showed considerable side lobes at the right side of the polar plot. In order to reduce said side lobes, the distance between the connector structure and the patch antenna was increased, by extending the 90 Ω CPW line length, by a length of 15 mm, obtaining the radiation pattern in blue. Not only the radiation pattern becomes more distorted, but also the antenna radiation efficiency decreases slightly (it decreased from 91% to 80%), as a result from increasing the line length, leading to a decision of not increasing above 15 mm, considered as a trade-off point.

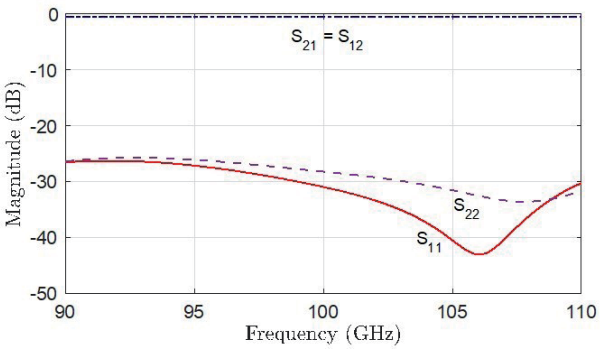

Figure 4. S-parameters of GCPW-CPW feed line leading into the antenna feed structure.

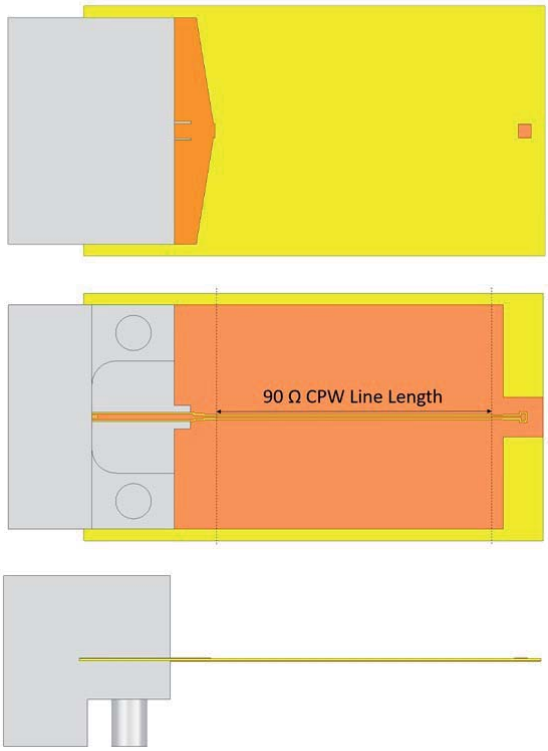

Figure 5. Top (a), bottom (b) and side (c) view of the connector with the full antenna element HFSS model.

2.4 TRL Calibration Kit Design

In order to allow for the conduction of calibrated measurements, a calibration kit suitable for the antenna element was designed. Measurement errors in network analysis can be divided into systematic and random errors. Systematic errors are calibrated out of the measurement process with the use of a calibration kit to allow for an accurate comparison between simulated and experimental results, regarding the reference plane. As opposed to the SOLT calibration, which is not viable at high frequencies, due to parasitic capacitances on load standard [14], a TRL (Through(Thru)-Reflect-Line) kit was designed, where for this type of calibration, only the line standard needs to be precisely known. The thru standard is a zero-length distance between the desired reference planes of each port. For the reflect standard, the use of a short standard was preferred, due to the fact that open standards are prone to radiate. The line standard is essentially the thru standard, but with an extra line length between both reference planes. In comparison with the thru standard, the transmission coefficient phase of the line standard should only vary between 20º and 160 º, hence as a rule of thumb, 90º is usually preferred, which also results in a bandwidth limitation [15]. From the simulations results, the S_{21} phase difference between the through and line standard: $\Delta\varphi \approx 90.53^0$, as well as, the offset delay of the 90º electrical length line portion: $\Delta t \approx 6.82\,ps$, were obtained, the latter needed for the VNA configuration of the TRL kit. In Figure 7, the HFSS model of the TRL kit is shown, and

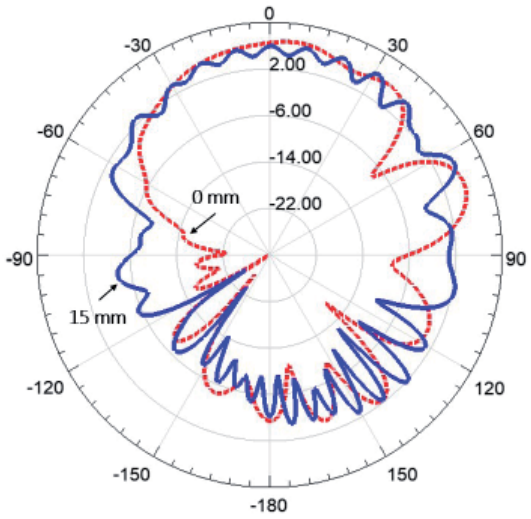

Fig. 6. Antenna radiation pattern for the θ plane at ϕ=90º for the variation of the CPW 90 Ω line length – 0 mm (red dashed line) and 15 mm (blue solid line), at 100 GHz.

in Figure 8, the simulated results of the S-parameters for the three standards of the TRL kit are displayed.

3. Simulation And Experimental Results Comparison

In this section, a comparative analysis of S11 (reflection coefficient) and radiation pattern (θ plane, ϕ=0º) between simulated and measured results is presented. The measurement setup used to obtain the experimental results is displayed as a schematic in Figure 9. In this experiment, the distance between the reference horn antenna and the AUT (antenna under test) is 0.9 m, placing the measurement within the far-field condition.

A picture of the fabricated antenna element and TRL calibration kit is displayed in Figure 10. In terms of the S_{11} results, observed in Figure 11, simulation and experiment are in close agreement, both regarding the reflection coefficient magnitude at the reference plane, shown previously in Figure 3. The observed discrepancies between both results are due to manufacturing tolerance and misalignment, as well as the PCB board flexibility throughout the measurement

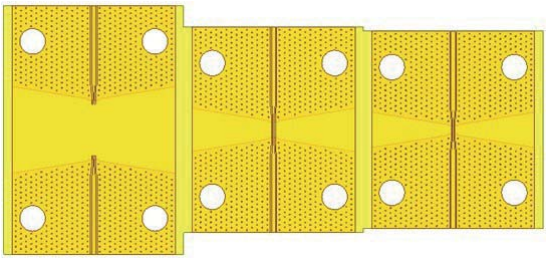

Figure 7. HFSS model of the TRL calibration kit.

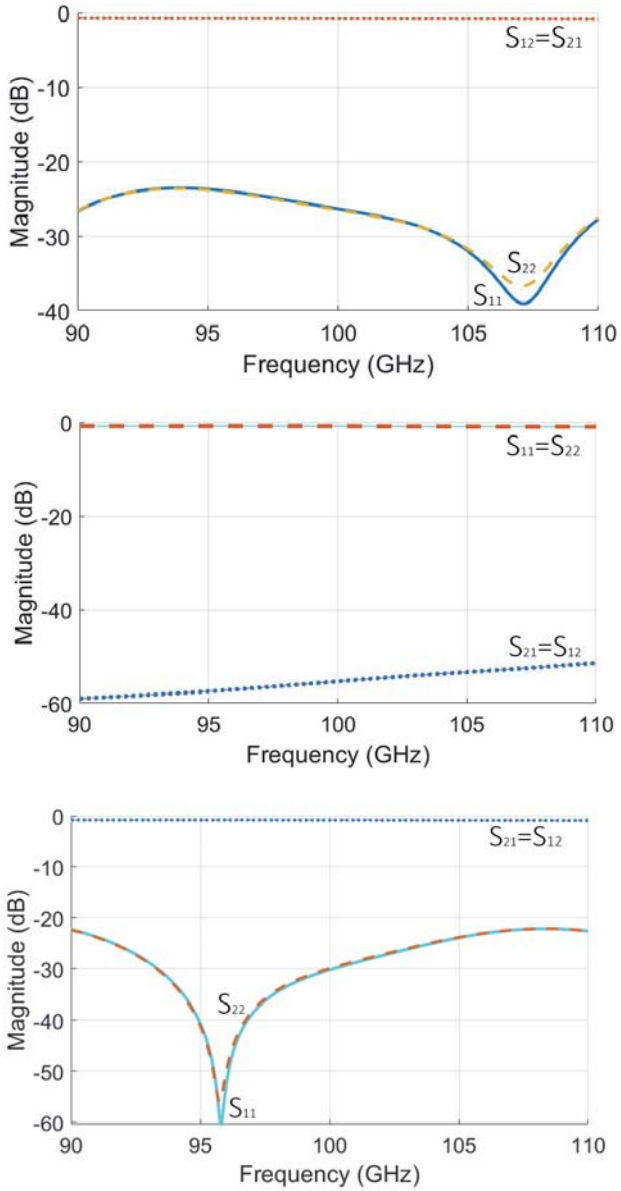

Figure 8. Simulated S-parameters of the Through (a), Reflect (Short – (b)) and Line (c) standards.

process, given the small substrate height used. As such, the resonant dip in the measured S11 is shifted slightly below the intended resonant frequency of 100 GHz, and

Figure 10. Fabricated antenna element (a) and TRL calibration kit (b).

a bandwidth of approximately 6.7 GHz was measured, in comparison to the 7.66 GHz obtained for the simulation. Regarding the measured radiation pattern (see Figure 12), the measurement in the anechoic chamber was performed in steps of 5º and it was only possible to measure from -90º to 90º due to mechanical restrictions, while for the simulated results, it is shown in steps of 1º for all angles. Comparing both radiation patterns, although the measured pattern presents a lower gain for most of the angles, it shows a reasonable agreement regarding the peak gain at $\phi = 0º$ (simulated peak gain value: 6.09 dBi and measured peak gain value: 6.33 dBi).

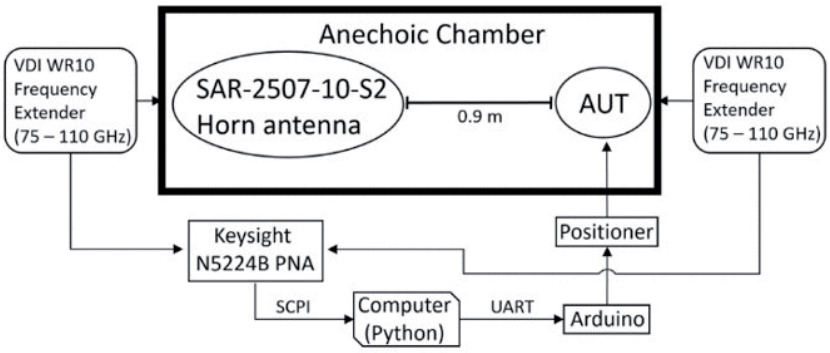

Figure 9. Measurement setup schematic.

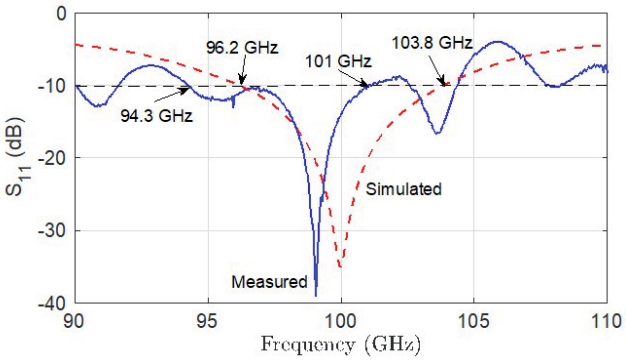

Figure 11. Simulated and Measured Reflection Coefficient (S11).

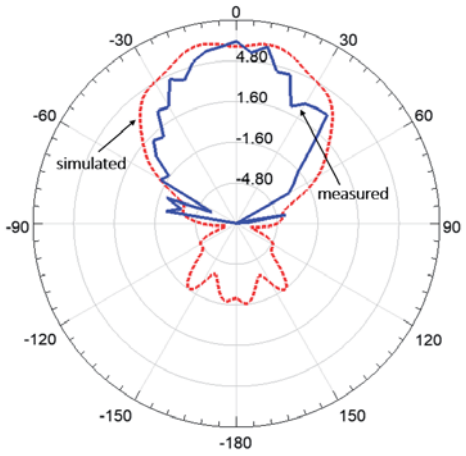

Fig. 12. Simulated (red dashed line) and Measured (blue solid line) Radiation Patterns for the ϕ plane, at θ = 0º (magnitude values in dBi).

5. Conclusions

In this work, an antenna element fed by a GCPW-CPW square loop feed on a substrate with 0.127 mm thickness and $\varepsilon_r = 2.2$, including a TRL calibration kit, was designed, fabricated and characterized experimentally, having obtained at least 5 percent of fractional bandwidth and a peak gain of 6.33 dBi, fulfilling the minimum requirements. Future work includes further optimization and the application of this type of feeding method to an antenna array that also operates at a frequency of 100 GHz.

References

1. Zhang, Zhengquan et al. "6G Wireless Networks: Vision, Requirements, Architecture, and Key Technologies." *IEEE Vehicular Technology Magazine* 14 (2019): 28-41.

2. J. Liu, S. Chen, K. Xiao, and X. Chen, "100 GHz Silicon-based micro-machined patch antenna and arrays," *J. Eng. (Stevenage)*, **vol. 2019**, no. 19, pp. 5622–5625, 2019.

3. G. P. Gauthier, S. Raman and G. M. Rebeiz, "A 90-100 GHz double-folded slot antenna," in *IEEE Transactions on Antennas and Propagation*, **vol.47**, no. 6, pp. 1120-1122, June 1999, doi: 10.1109/8.777141.

4. M. Sun and Y. P. Zhang, "100-GHz Quasi-Yagi Antenna in Silicon Technology," in *IEEE Electron Device Letters*, **vol. 28**, no. 5, pp. 455-457, May 2007, doi: 10.1109/LED.2007.895447.

5. T. S. Rappaport, Y. Xing, G. R. MacCartney, A. F. Molisch, E. Mellios and J. Zhang, "Overview of Millimeter Wave Communications for Fifth-Generation (5G) Wireless Networks—With a Focus on Propagation Models," in *IEEE Transactions on Antennas and Propagation*, **vol. 65**, no. 12, pp. 6213-6230, Dec. 2017, doi: 10.1109/TAP.2017.2734243.

6. C. Balanis, *Antenna Theory: Analysis and Design.* Wiley, 2016.

7. Pozar, D., *Microwave engineering.* Hoboken: John Wiley & Sons, 2012.

8. R. Simons, *Coplanar Waveguide Circuits, Components, and Systems.* Wiley Series in Microwave and Optical Engineering, Wiley, 2004.

9. W. Menzel and W. Grabherr, "A microstrip patch antenna with coplanar feed line", in *IEEE Microwave and Guided Wave Letters*, **vol. 1**, no. 11, pp. 340-342, Nov. 1991, doi: 10.1109/75.93905.

10. K. Elissa, "Title of W. Chai, X. Zhang, and J. Liu, "Characteristics Study of Four Coplanar Waveguide Feeding Devices", *PIERS Online*, **vol. 3**, no. 1, pp. 48–51, 2007.

11. B. Ghosh, Y. M. M. Antar, A. Petosa and A. Ittipiboon, "Feed configurations of CPW fed DRA," *IEEE Antennas and Propagation Society Symposium*, 2004., Monterey, CA, USA, 2004, pp. 1347-1350 **Vol.2**, doi: 10.1109/APS.2004.1330435.

12. Hettak, K., Delisle, G. Y., & Talbi, L., "Design of 60-GHz CPW fed patch antenna for Switched-beam antenna array", *2013 IEEE Antennas and Propagation Society International Symposium (APSURSI)*, 2013.

13. M. Milijić, A. Nešić and B. Milovanović, "Study of dielectric substrate effect on modelling CPW-fed slot antenna arrays," *2017 13th International Conference*

on Advanced Technologies, Systems and Services in Telecommunications (TELSIKS), Nis, 2017, pp. 105-108, doi: 10.1109/TELSKS.2017.8246239.

14. V. H. B. Preuss and F. R. de Sousa, "A Study on Low-Cost Calibration Kits for U.FL Connector Systems," *2019 4th International Symposium on Instrumentation Systems, Circuits and Transducers (INSCIT)*, Sao Paulo, Brazil, 2019, pp. 1-6, doi: 10.1109/INSCIT.2019.88.
15. Keysight Technologies, "Specifying Calibration Standards and Kits for Keysight Vector Network Analyzers.", Available: https://www.keysight.com/zz/en/assets/7018-01375/application-notes/5989-4840.pdf.

A Preventive Maintenance Approach to Optimize Fault Management using Machine Learning

M. Pereira[1], D. Duarte[2], and P. Vieira[1,3]

[1]Instituto Superior de Engenharia de Lisboa (ISEL), Lisboa, Portugal

[2]CELFINET, Consultoria em Telecomunicações, Lda., Lisboa, Portugal

[3]Instituto de Telecomunicações (IT), Lisboa, Portugal

Abstract

Mobile networks' fault management can take advantage of Machine Learning (ML) algorithms making its maintenance more proactive and preventive. Currently, Network Operations Centers (NOCs) still operate in reactive mode, where the troubleshoot is only done after the problem identification. The network evolution to a preventive maintenance enables the problem prevention or quick resolution, leading to a greater network and services availability, to a better operational efficiency and, above all, ensures customer satisfaction.

In this paper, different algorithms for Sequential Pattern Mining (SPM) and Association Rule Learning (ARL) are explored, using real Fault Management (FM) data from a live Long Term Evolution (LTE) network. A comparative analysis of the performance and efficiency between all the algorithms was carried out, having observed a decrease of 3.31% in the total number of alarms and 70.45% in the number of alarms corresponding to the same type. There were also considerable reductions in the number of alarms per network node or zone, identifying 39 nodes that no longer had any unresolved alarm.

These results demonstrate that the recognition of sequential alarm patterns allows the preventive maintenance of a mobile communications network.

Keywords – fault management, machine learning, preventive maintenance, sequential pattern mining.

1. Introduction

Fault Management (FM) optimization in a mobile network involves taking advantage of Machine Learning (ML) techniques to make the mobile network's maintenance proactive and preventive.

Mobile network operations still work in reactive mode, *i.e.*, the diagnosis and problem solving starts only after a network malfunction occurs, a service is impacted, or a customer complains. The engineers have access to a lot of information such as alarms, performance measures and more, but they lack an effective way to resolve issues quickly. Thus, Mean Time To Repair (MTTR) is affected, impacting network and service availability, operational efficiency, and customer satisfaction.

With a solution for preventive maintenance, operators can leverage machine learning to reduce operational costs, improve network and service availability, improve customer satisfaction, and reduce missed Service Level Agreements (SLAs).

In this context, the main goal of this paper is to create a solution for preventive maintenance of mobile networks' alarms, using real data, that:

1) Mines alarms clusters and relationships between them, forming association rules;
2) Continuously learns from new data, gets better over time, and builds expertise in the maintenance domain;
3) Defines antecedent and consequent alarms in a sequential pattern, where they are sorted chronologically;
4) Recognizes the most frequent patterns in order to tell what the most concerning faults are and what advantages come from their prevention.

Some of the works related to preventive fault management are: [1], [2], [3]. In [1], the alarms' proactive management is addressed as a way to take advantage of ML algorithms to follow the evolution of mobile networks and services operations. In [2] and [3], research is carried out on the application of ML techniques and data mining in the fault management of telecommunications networks, from an operational point of view.

This paper is organized as follows: Chapter 2 presents, briefly, the study carried out on Association Rule Learning

(ARL) and Sequential Pattern Mining (SPM) algorithms and their respective evaluation metrics. Chapter 3 presents the experimental results of all the discussed algorithms' implementation, with a comparison of their efficiencies. Chapter 4 concludes the article with a summary of the most important points to take.

2. Methodology

2.1 Fault Management data

The dataset used in this work has several alarm logs from a live LTE network. These logs contain the timestamp, severity, name, type, technology, detailed information and network node associated with each alarm.

As described in [4], the alarms can be classified, as to their severity, as follows:

1) **Critical**: A critical alarm affects system services. As soon as it is triggered, immediate actions must be taken, even when the fault occurs outside working hours;
2) **Major**: A major alarm affects the quality of service and requires immediate action, only if occurs during working hours;
3) **Minor**: A minor alarm usually does not affect the quality of service. It should be treated as soon as possible or monitored to avoid potential severe failures;
4) **Warning**: A warning alarm indicates a possible error that could affect the quality of service. Requires different actions depending on specific errors.

These alarms can also be categorized by their type, depending on their operational area: Power; Environment; Signaling; Trunk; Hardware; Software; System; Communication; Service quality; Unexpected operation; Operations and Maintenance Center (OMC); Integrity; Operation; Physical resource; Security; Time domain; Running; Processing.

2.2 Association Rule Learning

Association Rule Learning (ARL) allows extracting correlations or strong associations, hidden between sets of items present in transactions that are found in a dataset. The association rules problem defines a transaction as a set of items where each item can have different attributes. The dataset in question contains several transactions. An association rule is an implication, written as $A \rightarrow C$ where A and C are sets of items called antecedent and consequent, respectively.

Generally, there are two metrics for evaluating an association rule: support and confidence, presented in equations (1) and (2), respectively. As datasets usually store large amounts of information but only the most frequent transactions are interesting, minimum values are defined for these evaluation metrics, which help to filter out less frequent rules.

Support: Relative frequency or occurrence probability of a transaction. It can take values between 0 and 1.

$$Support(A \rightarrow C) = \frac{Occurrences\ of\ A \cup C}{Total\ number\ of\ transactions} \quad (1)$$

Confidence: Probability of a transaction containing the consequent, knowing that it also contains the antecedent. Confidence is maximum if the consequent and the antecedent always occur together. It is not symmetric, that is, the confidence of $A \rightarrow C$ is different from the confidence of $C \rightarrow A$.

$$Confidence(A \rightarrow C) = \frac{Support(A \rightarrow C)}{Support(A)} \quad (2)$$

In addition to these two measures, others can be used to better classify the association rules, considering other properties that both support and confidence cannot quantify. In the scope of this work, three more evaluation metrics were used: lift, leverage, and conviction [5], presented in equations (3), (4) and (5), respectively.

Lift: Quantifies how frequent the simultaneous occurrence of A and C is compared to what would be expected if they were statistically independent. If A and C are independent, the lift will be equal to 1.

$$Lift(A \rightarrow C) = \frac{Confidence(A \rightarrow C)}{Support(C)} \quad (3)$$

Leverage: Difference between the frequency of A and C occurring together and the frequency that would be expected if A and C were independent. A value of 0 indicates independence between the two itemsets.

$$Leverage(A \rightarrow C) = Support(A \rightarrow C) - Support(A) \times Support(C) \quad (4)$$

Conviction: A high value means that C is strongly dependent on A. For example, if the confidence is equal to 1, the denominator will be 0, so the conviction will be ∞∞. Like lift, if items are independent, the conviction is equal to 1

$$Conviction(A \rightarrow C) = \frac{1 - Support(C)}{1 - Confidence(A \rightarrow C)} \quad (5)$$

In the development of the work, three ARL algorithms were implemented: Apriori [6], Eclat [7] and FPGrowth [8].

2.2.1 Apriori

This algorithm has to access the dataset multiple times to read all the frequent itemsets. In its first access, the support is counted for each individual item (level 1 itemsets). Then, with a minimum support value, S, rare items are excluded, that is, those whose support is lower than S.

In later accesses, higher-level itemsets containing rare items are removed, because if an item's support, S_i, is lower than S, then all itemsets that contain it will have a support equal or lower than S_i and, thus, lower than S (Apriori property).

This process is done iteratively for every frequent itemset in the dataset. The final list of frequent items is the junction of each level's list, including the support values calculated for each frequent itemset.

2.2.2 Eclat

Eclat is an improved version of Apriori that uses a vertical dataset representation, where it lists the transactions in which item occurs, instead of indicating the itemsets that belong to each transaction (horizontal representation).

Transaction lists for higher-level itemsets are created recursively, calculating the intersection of the previous level transactions lists. If this intersection is null, the itemset is removed. This process runs until all intersections become null.

If the minimum support is set to the same value, the final list of frequent itemsets will be identical to that of the Apriori algorithm. However, Eclat takes up less memory throughout the process, manages to be faster by using a vertical approach (in which calculations are done in parallel) and accesses the dataset less often, because it is possible to calculate the support values for any level.

2.2.3 FPGrowth

The FPGrowth algorithm uses the concept of a Frequent Pattern (FP)-tree, a tree that contains the prefixes of the transactions. Each tree branch represents a set of transactions that share the same prefix, where each node corresponds to a single item. All nodes referring to the same item are linked together, so that all transactions that contain an item can be easily found when traversing the tree.

The main process that this algorithm performs is to build the FP-tree of a projected dataset, that is, a dataset with the transactions that contain a certain item, with that item removed. The projected dataset is processed recursively, not forgetting that every frequent itemset share the same prefix – the item that was removed.

After building the FP-trees for all the dataset projections, some of the nodes associated with rare items are pruned, in order to simplify the tree and speed up the process.

Thanks to an efficient implementation of FP-trees, the FPGrowth algorithm largely outperforms both Apriori and Eclat algorithms in terms of execution time and memory usage, since the storage of the dataset using a tree representation is more compact than the complete list of transactions.

2.3 Sequential Pattern Mining

Sequential Pattern Mining (SPM), unlike ARL, takes the items' order in each sequence into consideration, allowing to discover frequent patterns in a dataset, which may prove useful or simply interesting to be explored.

The objective of SPM algorithms is to find all patterns (sub-sequences) that have a support greater than or equal to the minimum support value defined by the user. Therefore, there is one and only one answer to a problem of this type. What differentiates the various algorithms is just their efficiency in finding that answer.

In the development of the work, three SPM algorithms were implemented: PrefixSpan [9], SPADE [10] and SPAM [11].

2.3.1 PrefixSpan

Based on FPGrowth, PrefixSpan is a pattern-growth algorithm and the only one of the three studied SPM algorithms that does not consider all possible combinations for the patterns that can be found. It recursively accesses the dataset to concatenate new items until the full pattern is formed, therefore, it only considers the patterns that really exist in the dataset.

These successive accesses can, however, take a very long time, so the "projected dataset" concept is also applied here to reduce its size, optimizing the accesses that need to be made. In terms of memory usage, creating multiple projections can take up a lot of data storage space.

2.3.2 SPADE

Inspired by Eclat, SPADE uses a vertical dataset representation, created during the first access, that indicates in which itemsets and in which sequence each item occurs.

The vertical representation has two interesting properties for recognizing sequential patterns. The first, is that the list created for any sequence allows directly calculating its support. The second property is that the

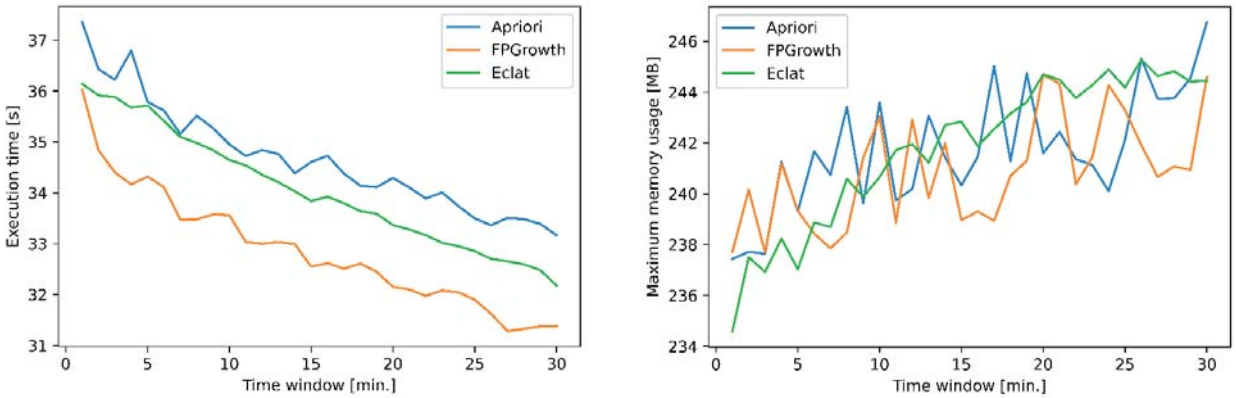

Figure 1. **Execution times (a) and memory usages (b) of each algorithm, for various time windows.**

list of any sequence can be obtained, without the need to access the original dataset, by joining the lists of every sub-sequence that is part of it.

By taking advantage of these properties, SPADE performs its discovery for sequential patterns without repeatedly accessing the dataset and, therefore, without keeping many patterns in memory.

2.3.3 SPAM

Similar to SPADE, the SPAM algorithm manages to be even more efficient by optimizing the structure of the pattern list. It encodes these lists as binary vectors, which cuts the memory needed to store the same information. Using compression techniques, that reduce the number of used bits, SPAM improves even further in the speed of mathematical operations that need to be performed.

This algorithm has been shown to be faster than both SPADE and PrefixSpan, especially for relatively large datasets. In terms of memory, SPADE still manages to be the more efficient of the two.

3. Experimental Results

In order to discover the association rules and sequential patterns that arise in the network, and to obtain some practical conclusions that verify the expected results in theory, real Fault Management (FM) data were used to test, analyze, and compare the studied algorithms.

To evaluate any and all association rules, the minimum support value was set at "2 occurrences / Total number of transactions", that is, it is enough to have a repetition of a certain set of items for it to be considered frequent. A minimum confidence of 50% was also imposed, which

Table 1. The 6 association rules, and respective evaluation metrics calculated by the three algorithms, with greater Lift.

Minute(s)	Network node	Antecedent(s)	Consequent(s)	Support	Lift	Leverage
15 - 21	BX94BL	RF Unit ALD Current Out of Range	ALD Maintenance Link Failure	0.00134 - 0.00157	741.5 - 634.0	0.00134 - 0.00157
15 - 21	BX94BL	ALD Maintenance Link Failure	RF Unit ALD Current Out of Range	0.00134 - 0.00157	741.5 - 634.0	0.00134 - 0.00157
1 - 2	VA08OL	X2 Interface Fault	Inter-System Cabinet Configuration Conflict	0.00151 - 0.00158	662.0 - 632.0	0.00150 - 0.00157
1 - 2	VA08OL	Inter-System Cabinet Configuration Conflict	X2 Interface Fault	0.00151 - 0.00158	662.0 - 632.0	0.00150 - 0.00157
2	BX16QL	Certificate Invalid	External Clock Reference Problem	0.00202	494.0	0.00202
2	BX16QL	External Clock Reference Problem	Certificate Invalid	0.00202	494.0	0.00202

Table 2. Execution times and memory usages of each algorithm, for the dynamic time window.

Algorithm	Execution time	Maximum memory usage
PrefixSpan	14 minutes 43 seconds	179.07 MB
SPADE	15 minutes 9 seconds	178.06 MB
SPAM	13 minutes 50 seconds	180.18 MB

indicates that, at least, for a given rule, half of the transactions that contain the antecedent also contain the consequent.

Before analyzing the results and to assess the efficiency of each algorithm, the execution times and memory used were measured. These results were obtained from tests performed on a machine with the following specifications: Intel® Core™ i5-7300HQ CPU @ 2.50GHz (4 CPUs), 8GB RAM, Windows 10 Education 64bits.

3.1 Association Rule Learning

In the implementation of the algorithms Apriori and FPGrowth, the MLxtend library [12] was used. For Eclat, PyFIM [13] was used. The tests were carried out for temporal windows from 1 to 30 minutes, every minute. Comparative graphs for the different time windows are shown in Figure 1.

As can be seen in Figure 1a), the execution times of all algorithms decrease as the time window increases. Although, with this increase, there are transactions with more sets of items, the number of transactions is decreasing and, ultimately, there are fewer evaluation metrics to calculate, which justifies the time reduction. Comparing the executions times of each algorithm, it is possible to verify that the fastest is FPGrowth, followed by Eclat and, finally, the slowest is Apriori. As for Figure 1b), despite constant fluctuations, it is possible to verify that memory usage increases as the time window increases, which is justified by the increase in the number of items in each transaction. In general, it is possible to conclude that the most efficient in terms of memory occupation is also FPGrowth. Eclat manages to be very optimized for small transactions, but after a certain point it uses even more memory than Apriori.

The list of rules, identical to all algorithms, was sorted by the Lift metric in descending order, since those with this higher value are those with a greater dependence between the rule's antecedent and consequent. The first 6 rules are shown in Table 1. The confidence and conviction metrics were omitted as they were the same for all evaluated rules

Table 3. The 5 sequential patterns, and respective evaluation metrics calculated by the three algorithms, with greater Lift.

Network node	Pattern	Support	Confidence	Lift	Leverage	Conviction
VA08OL	{Inter-System Cabinet Configuration Conflict, X2 Interface Fault}	0.00259	1.0	386.5	0.00258	∞
VA83WL	{RF Unit ALD Current Out of Range, ALD Maintenance Link Failure}	0.00274	1.0	364.33	0.00274	∞
BX16QL	{Certificate Invalid, External Clock Reference Problem}	0.00197	0.66	226.0	0.00196	2.9912
AB42AL	{Inter-System Cabinet Configuration Conflict, X2 Interface Fault}	0.00476	1.0	210.0	0.00474	∞
TX49BL	{ALD Maintenance Link Failure, External Clock Reference Problem}	0.00477	1.0	209.66	0.00475	∞

and time windows, having the values 1 and ∞, respectively.

In the first column of this table there are the different lengths of time windows that got the best results. Some of the associations, namely the first 4, were aggregated because they were present for consecutive time windows, hence, the range of values, both in this column and in the corresponding evaluation metrics.

In spite of the support values being low, the algorithms demonstrate conviction that these associations are quite strong, that is, when a certain antecedent alarm occurs, the consequent alarm will occur afterwards.

It is possible to verify that, for a given time window and network node, there is always a pair of symmetric rules, *i.e.*, there is always a second rule where the antecedent is the consequent, and the consequent is the antecedent of the first rule. Therefore, it is not possible to be sure of the order of occurrence of the alarms, and it is necessary to resort to sequential pattern mining.

3.2 Sequential Pattern Mining

In the implementation of the algorithms, the extensive framework for data mining SPMF [14] was used.

In the development of the work reported in the previous section, it was noticed that there was no need to test several time windows (1 to 30 minutes, every minute) in the definition of transactions, as the results are similar for all of them. Therefore, for these algorithms, transactions were defined based on a single dynamic window. There is a timeout interval in which if no alarm happens during that interval, the next alarm that occurs will belong to the next transaction.

The timeout value was defined considering the predominant association rules in the previous section, namely those that contained alarms associated with the Antenna Line Device (ALD). As the objective is that this pair of alarms is always in the same transaction, the timeout was fixed at 11 minutes, as this is the maximum time interval registered between the two alarms.

The execution times and memory usage of each algorithm were measured, for the dynamic window, and are presented in Table 2.

Observing the average value of three tests executed in a row, it appears that the fastest algorithm is SPAM, followed by PrefixSpan, and finally SPADE. In terms of occupied memory, the order is reversed, with SPADE being the most efficient, followed by PrefixSpan and, finally, SPAM.

The list of patterns, identical to all algorithms, was sorted by the Lift metric in descending order, as those with this highest value are those with a greater dependency among all the alarms that make up the pattern. The first 5 patterns are shown in Table 3.

As can be seen, the same alarms that had already appeared in the association rules of the previous section continue to appear here. However, this time there are no longer symmetrical rules, only the patterns themselves, which, by themselves, already indicate the order in which the alarms occur.

All patterns listed have been validated using each alarm's documentation. Furthermore, assuming that when the antecedent is resolved, the consequent no longer happens and that the time interval between them is sufficient to report the failure, trigger a fictious work order and solve the problem, the consequent will be removed from the original dataset, and the maximum reduction in the number of alarms will be calculated.

The next sections will present some use cases considering the patterns found in Table 3.

3.2.1 RF Unit ALD Current Out of Range → ALD Maintenance Link Failure

In the context of preventive maintenance, it is necessary to understand what is gained by being able to recognize the patterns that happened in the past, in order to try to predict and prevent what will happen in the future. In this case, by preventing the antecedent alarm, 715 "ALD Maintenance Link Failure" alarms are removed. This mainly translates into the reduction of:

- "Communication"-type alarms: 1860 → 1145 (-38.44%);
- "VX73KL" node alarms: 40 → 22 (-45%);
- "CS12KL" node alarms: 87 → 51 (-41.38%);
- "VX37KL" node alarms: 179 → 107 (-40.22%);
- "CR29VL" node alarms: 64 → 44 (-31.25%).

3.2.2 Inter-System Cabinet Configuration Conflict → X2 Interface Fault

By solving the errors and configuration conflicts in the cabinet, 6327 "X2 Interface Fault" alarms can be prevented from happening. This mainly translates into the reduction of:

- Total number of alarms: 191053 → 184726 (-3.31%);
- "Signaling"-type alarms: 8981 → 2654 (-70.45%);
- "LO01AL" node alarms: 37 → 18 (-51.35%);
- "VX83EL" node alarms: 74 → 37 (-50%);
- "VX49KL" node alarms: 53 → 27 (-49.06%).

3.2.3 Certificate Invalid → External Clock Reference Problem

By properly validating the certificate, it can prevent a lot of "External Clock Reference Problem" alarms from happening. As this pattern shares the same consequent as the next, the calculation and analysis of this impact is made for the next pattern.

These two patterns are between "Major" alarms, while the first two were between a "Minor" antecedent and a "Major" consequent. This allows us to deduce, after analyzing the 4 cases, that the sequence of alarms always follows an increasing order in terms of severity. Of course, there may be alarms caused by alarms with the same severity (as in this case), but a less severe alarm than the previous one is unlikely to occur (for example, Major → Minor).

3.2.4 ALD Maintenance Link Failure → External Clock Reference Problem

This pattern is the second (of those described) in which the "External Clock Reference Problem" alarm is found as a consequence. This suggests that the problems in the external clock reference can be indirectly caused by various sources on the network, which lead to a bad configuration of the clock or the malfunction of some hardware element essential for proper clock synchronization.

Resuming the correct synchronization of the external reference clock, it prevents the occurrence of 1414 "External Clock Reference Problem" alarms. This mainly translates into the reduction of:

- "Hardware"-type alarms: 7969 → 6555 (-17.74%);
- There are 39 nodes that no longer have any unresolved alarm (-100%);
- "VX30EG" node alarms: 18 → 1 (-94.44%);
- "CR06VU" node alarms: 22 → 4 (-81.82%);
- "VX88EU" node alarms: 50 → 12 (-76%).

It is concluded that, with sequential pattern mining, it is possible to predict which will be the most likely alarm to be the consequence of a given antecedent alarm. Within the scope of preventive maintenance, if the problem resolution is quick and effective, it is possible to completely prevent the consequent alarm from occurring, resulting in a decrease in the number of triggered alarms and failures caused by them.

4. Conclusions

This work aimed to develop a solution for preventive and proactive maintenance in the fault management of LTE mobile networks, using two types of machine learning techniques for handling FM data: ARL and SPM.

For ARL algorithms, FPGrowth presented the best performance in terms of execution time and resources used. Eclat was the most efficient for short transactions, being surpassed by Apriori for larger transactions. In all of them there was a symmetry in the association rules, having therefore evolved to the SPM algorithms, where the order of alarms' occurrence is important.

In this case, SPAM turned out to be the most efficient in terms of execution time but the worst in terms of resource utilization. SPADE was the most efficient in terms of resource utilization but the slowest of all. On the other hand, PrefixSpan offered a good compromise among the three. In all the performed tests, it was possible to conclude that the prevention of consequent alarms results in a decrease in their absolute number in the network's nodes where they occurred.

In the best case, there was a decrease of 3.31% in all analyzed nodes, and 70.45% in terms of alarms of the same type. It was also found that 39 network nodes no longer had any unresolved alarm. These results demonstrate that sequential pattern mining drives the preventive maintenance of alarms in a LTE mobile network, reinforcing the preventive maintenance' importance for telecommunications operators.

5. Acknowledgements

This work was carried out in the scope of the international project Artificial Intelligence for Green Networks (AI4GREEN) C2018/1-5, under the CELTIC-NEXT Core Group and the EUREKA Clusters program. The authors would like to thank the COMPETE/FEDER program for funding the national component of the project (16/SI/2019), as well as the Instituto de Telecomunicações (IT) and CELFINET for its support.

6. References

1. C. G. Araújo, G. Cardoso, J. Sousa, M. Coutinho, P. Neves, "Predictive fault management," in *InnovAction #4*, Altice Labs, 2019.

2. D. Mulvey, C. H. Foh, M. A. Imran and R. Tafazolli, "Cell Fault Management Using Machine Learning Techniques," *IEEE Access*, **7**, pp. 124514-124539, 2019.

3. M. Nouioua, P. Fournier-Viger, G. He, F. Nouioua, and M. Zhou, "A survey of machine learning for network fault management," in *Machine Learning and Data Mining for Emerging Trend in Cyber Dynamics*, 2021.

4. Huawei, *3900 Series Base Station Product Documentation, V100R010C10*, Huawei Technologies Co., 2015.

5. "MLxtend evaluation metrics." http://rasbt.github.io/mlxtend/user_guide/frequent_patterns/association_rules/#metrics. Accessed: 2021-09-21.

6. R. Agrawal and R. Srikant, "Fast algorithms for mining association rules in large databases," in *Proceedings of the 20th International Conference on Very Large Data Bases*, VLDB '94, (San Francisco, CA, USA), p. 487–499, Morgan Kaufmann Publishers Inc., 1994.

7. M. Zaki, "Scalable algorithms for association mining," *IEEE Transactions on Knowledge and Data Engineering*, **12**, 3, pp. 372–390, 2000.

8. J. Han, J. Pei, Y. Yin, and R. Mao, "Mining frequent patterns without candidate generation: A frequent-pattern tree approach," *Data Mining and Knowledge Discovery*, **8**, pp. 53–87, 01 2004.

9. J. Pei, J. Han, B. Mortazavi-Asl, J. Wang, H. Pinto, Q. Chen, U. Dayal, and M. Hsu, "Mining sequential patterns by pattern-growth: The prefixspan approach," *IEEE Transactions on Knowledge and Data Engineering*, **16**, pp. 1424–1440, Nov. 2004.

10. M. Zaki, "SPADE: An efficient algorithm for mining frequent sequences," *Machine Learning*, **42**, pp. 31–60, 01 2001.

11. J. Ayres, J. Flannick, J. Gehrke, and T. Yiu, "Sequential pattern mining using a bitmap representation," in *Proceedings of the Eighth ACM SIGKDD International Conference on Knowledge Discovery and Data Mining,* KDD '02, (New York, NY, USA), p. 429–435, Association for Computing Machinery, 2002.

12. S. Raschka, "MLxtend: Providing machine learning and data science utilities and extensions to python's scientific computing stack," *The Journal of Open Source Software*, **3**, Apr. 2018.

13. C. Borgelt, "Frequent item set mining," *WIREs Data Mining and Knowledge Discovery*, **2**, 6, pp. 437–456, 2012.

14. P. Fournier-Viger et al., "The SPMF Open-Source Data Mining Library Version 2," in *Machine Learning and Knowledge Discovery in Databases* (B. Berendt, B. Bringmann, É. Fromont, G. Garriga, P. Miettinen, N. Tatti, and V. Tresp, eds.), (Cham), pp. 36–40, Springer International Publishing, 2016.

Quasi-Yagi Microstrip Dipole Antenna with Circular Arc Parasitic Elements for Wireless Sensing Networks

Tiago E.S. Oliveira[1], João R. Reis[2], and Rafael F.S. Caldeirinha[2]

[1]Polythecnic of Leiria, Leiria, Portugal

[2]Instituto de Telecomunicaçoes, Leiria, Portugal
Email: rafael.caldeirinha@ipleiria.pt

Abstract

In this paper, a Quasi-Yagi microstrip dipole antenna with circular arc parasitic elements for wireless sensing networks is presented. With the aim of being employed in a multi-sector base-station (BS) of a Wireless Sensing Network (WSN), the proposed antenna is designed and optimised to operate in the 2.4 GHz ISM band. Specific project requirements, such as: operating frequency, gain, half power beam-width (HPBW) and, consequently, Field of View (FOV) are taken into consideration when dimensioning the antenna. After proper design optimization, carried out with the aid of a full wave electromagnetic solver (CST Microwave Studio), an antenna prototype has been fabricated and experimentally characterized inside an anechoic chamber. From the measurement results obtained with the prototype, the antenna yields to a realised gain of 8.6 dBi, an HPBW of 64° and 42° in the azimuth and elevation planes, respectively, and a back-to-front ratio of 16.4 dB, at 2.44 GHz. The measurement results are proved to be in good agreement with the simulation ones.

Index Terms: Antenna, Quasi-Yagi, WSN, Base-Station, Director, Circular Arc.

1. Introduction

Wireless Sensor Networks (WSNs) are nowadays widely implemented [1], often being offered as a solution for monitoring networks, in particular for: environment monitoring [2], [3], security [4], [5], health monitoring [6], [7], agricultural [8], [9], hazard detection [10], among many others. A WSN is typically arranged in a point to multi-point configuration, composed of a collection of a large number of Sensor Nodes (SN) that are scattered in a certain monitoring area [11] and, a Base Station (BS) which collects the nearby environment data and forward it to higher layer network or upload to a Cloud service for further analysis.

In the majority of WSN applications, it is desirable to have a BS covering all its surroundings, typically requiring a Field of View (FOV) of 360 degrees. Antennas that exhibit an omnidirectional radiation pattern, e.g. dipole or monopole antennas, can fit the purpose, offering however, relatively low gains, which consequently impact the dynamic range of the system. To overcome this issue there are many techniques known in the literature, as e.g. beamforming, beamsteering and antenna sectorisation.

In particular, antenna sectorisation comprehends the division of the area (cell) covered by the antenna radiation pattern, in sub-sectors, so that higher directivity antennas with lower FOV can be employed [12]. Ultimately, the number of sectors depends on the half power beam-width (HPBW) of a single element antenna [13].

To this extend, it is proposed in this paper a novel microstrip quasi-Yagi antenna, based on the Yagi-Uda antenna principle. These antennas typically present relatively high gain, depending on the number of elements used, and moderate front-to-back ratio [14], ideal for the proposed application. In fact, Yagi-Uda antennas are very well known and their design procedure is well established from many years ago [15]. These end-fire antennas are typically composed of parallel metallic rods acting as reflector and directors of a driven element and, widely used for terrestrial television broadcasting services, in the HF, VHF and UHF bands [14]. Due to its popular design, they have rapidly been adapted to microstrip technology, by etching the directors and reflector directly in dielectric substrates [16], [17]. In recent years, several authors have been evolving this particular antenna design or constructed new antennas based on its physical principle. For example in [18], the authors have suggested a cloaked Yagi-Uda design, by introducing novel radiator designs, capable of being electromagnetically undetectable in another desired frequency range. In [19], the authors recurred to Square-Shaped Split Ring Resonators (SRRs) to reduce the width of planar Yagi-Uda antennas. In [20], the authors developed a wideband beam-switchable quasi-Yagi antenna array

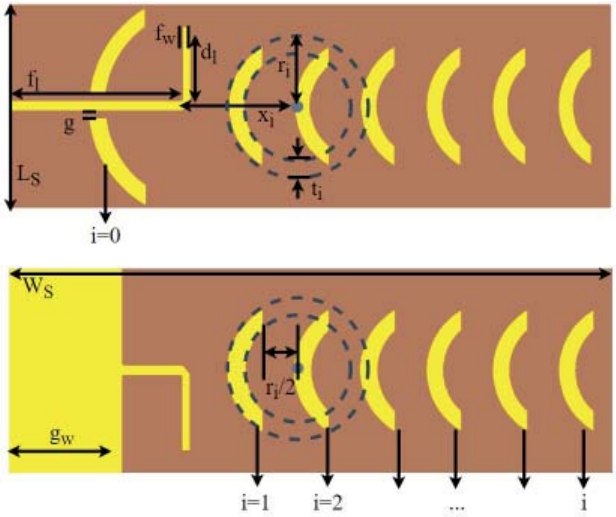

Figure 1. Proposed circular arc Quasi-Yagi antenna layout: (a) top view and (b) bottom view.

operating at 28 GHz, for mobile handsets. The proposed architecture consists of five quasi-Yagi antennas printed on Rogers substrate. More recently in [21], the authors have presented a three-port vertically polarized Quasi-Yagi Multiple-Input-Multiple-Output (MIMO) with pattern diversity for 5G N78 band applications. In this paper, it is proposed a novel quasi-Yagi antenna design based on circular arc shaped directors and reflector. Design guideline and simulation workout is presented for the antenna operating in the 2.4 GHz band, aiming at least 9 dBi of gain, a HPBW of 60 degrees, and a back-to-front ratio greater than 15 dB.

This paper is organised as follows: In Section II the antenna layout is thoroughly described. Section III presents in detail the parametric simulation and subsequent antenna optimisation, using a full wave electromagnetic solver (CST Microwave Studio). In section IV, the experimental setup considered for antenna characterisation is described, followed by subsequently analysis and discussion of the experimental results obtained from the prototype. Finally, in Section V the main conclusions are drawn.

2. Antenna Layout

The proposed antenna is depicted in Figure 1. It is based on a Yagi-Uda antenna design applied to microstrip technology, in which metallic parasitic elements are used as directors and reflector, in order to focus the radiated energy in one direction. The antenna is composed of a microstrip dipole, a circular arc shaped reflector over a ground plane (defined by gw) and, six circular arc shaped directors. The circular arc shaped reflector and directors should be seen as a quarter of a circle centred at x_i with radius r_i and thickness t_i, where i=0,1,2,... represents the number of the of the reflector/director, as depicted in Figure 1. The overall antenna dimensions are dictated by the parameters W_S x L_S. The feeding line width (f_w) and length (f_i) dictates the input impedance of the antenna, while the

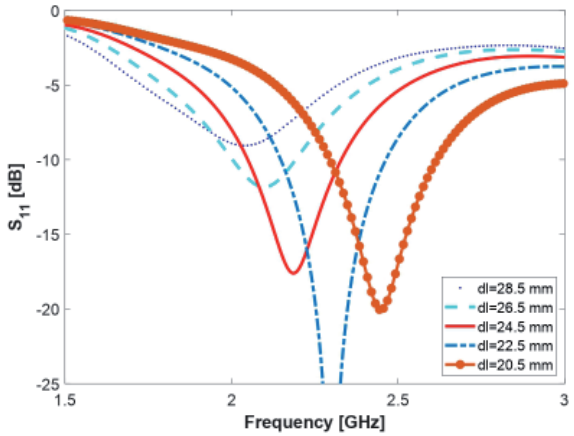

Figure 2. Simulated S11-parameter for several values of dl, within the selected parametric range.

frequency of operation is defined by the dimensions of the dipole arms (d_l). The dipole arms are perpendicular to the feeding line thus, creating a 90° bend which can cause an unnecessary signal reflection to the source. To overcome this issue the bend was mitred, to reduce the capacitance of the line, maintaining the desired impedance. The antenna was designed in a double-sided FR4 substrate with ε_r =4.4, a loss tangent of 0.014 and a thickness of h =1.6 mm. The optimisation of the antenna dimensions and the number of directors are further analysed and discussed next section.

3. Design and Optimisation

The proposed antenna design configuration was dimensioned with the assist of a full wave electromagnetic solver (CST MWS), in an iterative design approach. In a first iteration, the feeding element, *i.e.* the microstrip dipole was evaluated isolated (without directors and reflector), in order study the impact of the length of the dipole arm in S_{11} performance and, find the optimum value for antenna resonating at 2.44 GHz (target frequency). Therefore, a parametric study was carried out on d_l, with the initial value being set at λg/8 and by fixing gw at 32 mm, L_S = 61 mm and f_l = 52 mm. While L_S was defined to accommodate at least the arms length (i.e. 2× λg/8), f_l and gw were deliberately defined to further accommodate the reflector shape. f_w was set at 3.1 mm corresponding to a 50Ω impedance line for the proposed substrate. The simulation results of the parametric study are depicted in Figure 2. The parametric simulation run within the range of 20.5 to 28.5 mm, with 2 mm step. From the results, it is possible to observe that d_l = 20.5 mm is the optimised value for the desired resonance frequency (*i.e.* 2.44 GHz). With the dipole arms length already defined, the next step in the antenna design is to evaluate the impact of adding the directors in antenna performance. Therefore, a single director was added to the feeding antenna, at the position x_1 = 32 mm. At this point, no reflector has been considered. The initial values of t_1 =8 mm and r_1 = 22 mm were considered as starting point for the optimisation. The addition of the director provoked two effects in the antenna

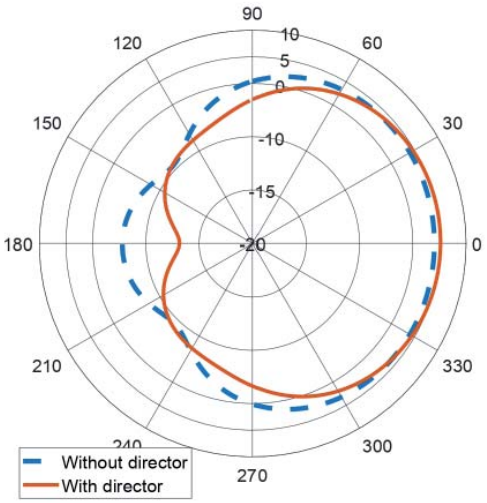

Figure 3. Impact of the addition of a single director in the antenna radiation pattern (in azimuth plane), at 2.44 GHz.

performance: an increase in the overall gain (Figure 3) and an undesirable deviation of the antenna's resonating frequency, as well as an increase of the S_{11} amplitude (Figure 4). While the first effect was expected (in line with the concept of Quasi-Yagi antenna), the latter is thought to be associated with mutual coupling between the driven element (dipole) and the added director. To correct this frequency shift, the length of the dipole arms d_l was optimised to 21.5 mm.

After ensuring the antenna was resonating at the desired frequency, a parametric study was carried out in all parameters of the circular arc director (r_1, x_1 and t_1). The study aims to optimise the circular arc director dimensions to achieve the greatest antenna gain possible,

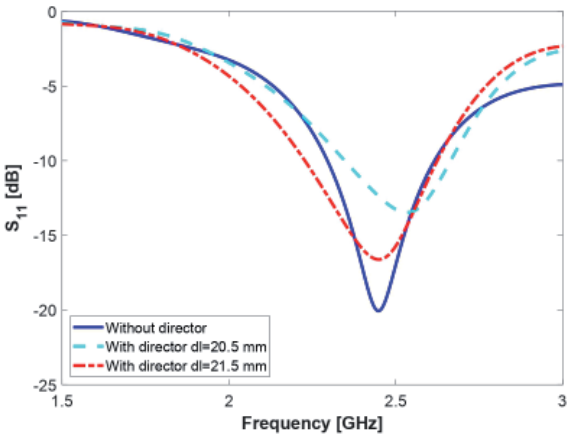

Figure 4. Impact of the addition of a single circular arc shaped director in S11-parameter.

while ensuring the antenna is still operating at the target frequency. From an extensive parametric study, it was found that the results which best favour the antenna performance in terms of gain are: $x_1 = 36$ mm, $t_1 = 5$ mm and $r_1 = 21$ mm. From Figure 5, it is possible to observe that such values yield a realised gain of 6.02 dBi, which mean an increase of 1.65 dB, when compared to the antenna layout without a director. Furthermore, different director shapes, such as the typical rectangular and, inverted circular arc shape, were also studied and optimised with the aid of several parametric simulations (not included in this paper due to space constraints). The simulated radiation patterns in the azimuth plane for the mentioned shapes (also optimized), are presented in Figure 6. When comparing the results, is clear that the circular arc shapes slightly improve the overall gain of the antenna, the addiction of a director with the rectangular shape generated a gain of 5.6 dBi, whereas for the inverted circular arc shape a gain of 5.86 dBi is presented and, as previously mentioned, the circular arc shape yields a realised gain of 6.02 dBi. The latter, not only

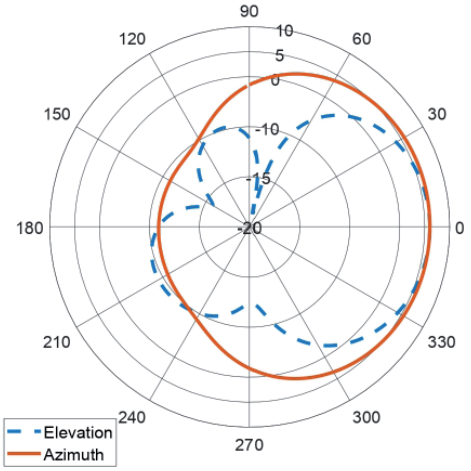

Figure 5. Radiation pattern in azimuth and elevation planes, at 2.44 GHz, for the optimised antenna with a single director.

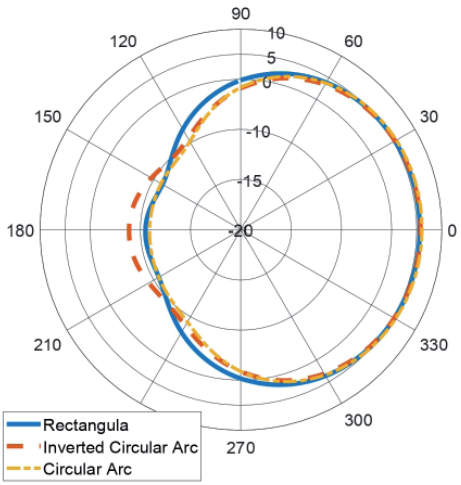

Figure 6. Radiation pattern in azimuth plane, at 2.44 GHz, for different optimised director shapes.

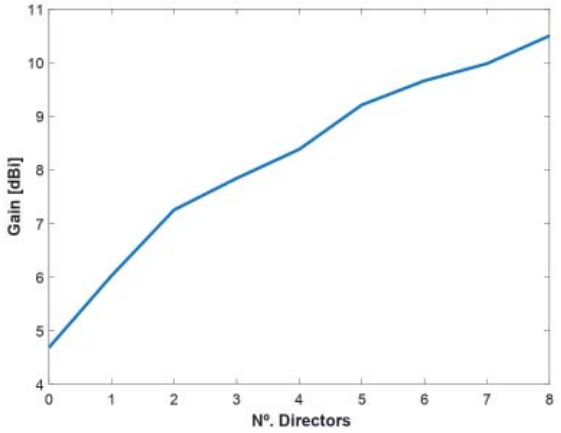

Figure 7. Variation of the realised gain against the number of directors.

presents the highest gain but also the best back-to-front ratio of 17 dB, therefore the circular arc shape was chosen.

Aiming to design an antenna with a higher gain, the process of adding directors has been studied. Thus, a parametric workout was carried out to access the gain improvement against the number of directors (with the same dimensions). The directors were added progressively to the layout, at the position $x_i = x_{i-1} + 18$ mm. The maximum gain at the antenna boresight has been obtained, and it is plotted against the number of directors (up to 8) in Figure 7. From the analysis of the results, it can be seen that after the addition of 6 directors, the ratio between gain and number of directors decreases. The difference from 6 to 8 directors is 0.81 dB, while the difference from 4 to 6 is 1.24 dB. Thus, for the best trade-off between antenna dimensions and gain, it was opted for 6 director design which achieves the target gain of 9.6 dBi. This represents an additional gain of 3.6 dB, when comparing with the configuration of a single director.

To further improve the front-to-back ratio of the antenna (already considering 6 directors), an additional circular arc shape was added to the design. The element was added prior to the feeding line (at the position $x0$ =8 mm), over the ground plane, acting as a reflector. The dimensions of the reflector were also optimised using CST MWS with the goal of improving the front-to-back ratio. From the parametric workout, it was found that the best front-to-back ratio is of 18.63 dB, achieved with r_0 = 34.5 mm, x_0 = 8 mm, t_0 = 5 mm and g = 2 mm, as depicted Figure 8, which improves 4.28 dB, from the case without reflector (Figure 8a). However, this change came at the expense of significantly increasing the side-lobe-levels, as it can be observed from the radiation patterns of Figure 8b. This indicates that most of the energy being reflected by the reflector is being re-radiated towards the side lobe direction, instead of the boresight direction, thus justifying the small increase of gain (only 0.1dB) of the main lobe. Please note that if the intention was exclusively increasing the gain of the main lobe, this could have been done by slightly shaping the reflector, e.g. making it more parabolic.

Finally, after all the design optimisation performed in this section, an antenna with an overall size of 175 × 61 mm^2, and dimensions (in mm): L_S = 61, W_S = 175, f_l = 52, x_0 = 8, g = 2, r_0 = 34.5, t_0 = 5, f_w = 3.1, t_i = 5, r_i = 21, x_1 = 36, x_2 = 54, x_3 = 72, x_4 = 90, x_5 = 108, x_6 = 126, gw = 32 and d_l = 21.5, presents a realised gain of 9.7 dBi,a total efficiency of -0.55 dB (89%), a front-to-back ratio of 18.63 dB and, a HPBW (FOV) of 60°. The polarization is vertical with the E-field parallel to the dipole arms

4. Experimental Characterisation

4.1. Setup

In order to experimentally characterise the proposed antenna, the prototype depicted in Figure 9 was fabricated. Firstly, antenna matching was evaluated by measuring the S_{11}-parameter, using a Vector Network Analyzer (VNA) (R&S ZVM). Subsquently, several antenna radiation

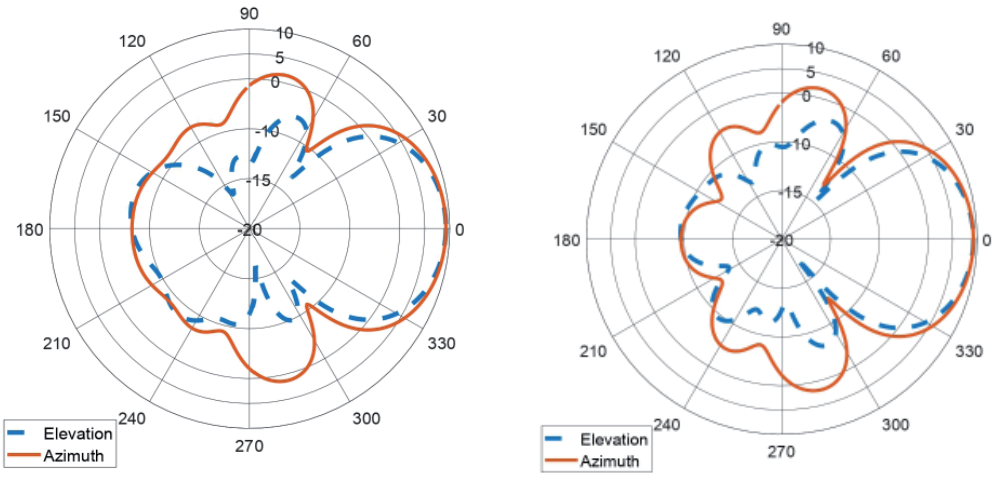

Figure 8. Radiation pattern in azimuth and elevation planes, at 2.44 GHz, (a) without and (b) with the reflector.

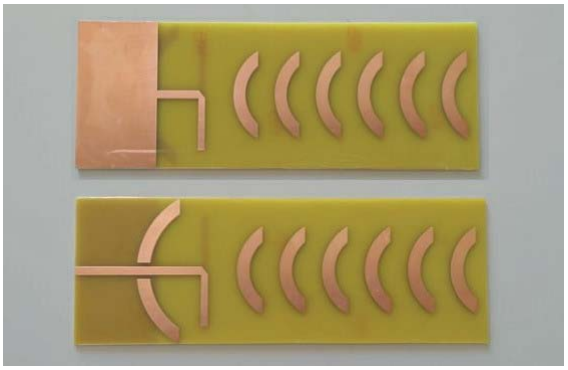

Figure 9. Photography of the Quasi-Yagi microstrip dipole antenna with circular arc parasitic elements prototype.

patterns, in the two main antenna planes, *i.e.* azimuth and elevation, have been obtained. To this end, the setup of Figure 10a was assembled inside an anechoic chamber enabling experiments to be performed in a controlled, electromagnetically quiet and reflection free radio environment.

In particular, a well characterised *Aaronia Hyperlog 30100* antenna was used as the Tx antenna (Figure 10b). It is connected to a Signal Generator (R&S SMR27) producing a continuous wave (CW)), with a transmission power of 0 dBm. At the receiver end, a well characterised *Aaronia Hyperlog 60100* antenna was connected to a spectrum analyser (Agilent E4407B) to be used as reference, later replaced by the antenna under test (AUT). The antennas were placed 3,5 meters apart, ensuring that the measurement took place in the far-field region of the antennas. The Tx antenna was kept fixed throughout the measurements, while the AUT was rotated around its axis with the assist of motorised pan/tilt head unit. The received power was acquired for each angular step with 1° of resolution, within the range defined between -180° and 180° (in the azimuth plane). Both Tx and Rx antennas were further rotated 90° to measure the radiation pattern in the elevation plane, using the same physical setup. The received power acquisition and movement control were executed in real-time and post processed in MATLAB, using a software developed for the effect.

4.2 Experimental Results

From the experimental S_{11}, depicted in Figure 11, it is possible to observe that the measured results are in good agreement with the simulated ones. Even though the S_{11} presents slightly difference around the resonance peak at 2.4 GHz, antenna matching is still below -10 dB, presenting a bandwidth of 390 MHz, defined between 2.12 to 2.51 GHz, in experiments, against a slightly larger bandwidth of 420 MHz in simulations. Such discrepancy can be associated to mismatched values of the permittivity of the substrate between the real data and the one provided by the manufacturer, accuracy issues associated with the

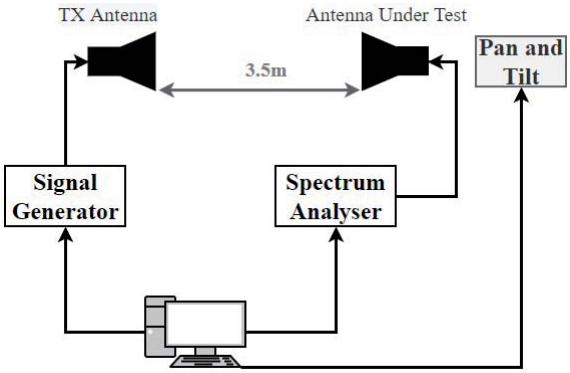

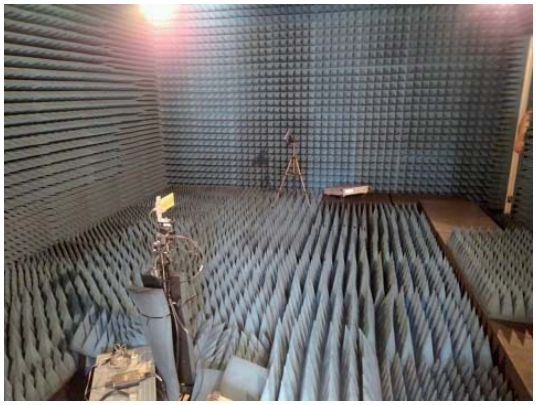

Figure 10. Radiation pattern experimental characterisation setup (a) diagram and (b) photography

PCB production technique (produced in-house), and the use of the SMA connector, not considered in simulations.

In terms of the radiation pattern obtained at 2.44 GHz, depicted in Figure 11b and Figure 11c for the azimuth and elevation planes, respectively, it can be observed a good agreement in the shape, between the simulation and measured results. According to experiments, the antenna presents a total gain of of 8.6 dBi, an HPBW of 64° in azimuth and 42° elevation planes, respectively, and a back-to-front ratio of 16.4 dB. This compares to simulations by having a decrease of 1.1 dB in total gain and 2.2 dB in back-to-front ratio. HPBW in simulations also decreases by 5° in both azimuth and elevation planes.

5. Conclusions

A novel Quasi-Yagi Microstrip Dipole antenna with circular arc parasitic elements is proposed in this paper. The antenna is comprised of a microstrip dipole used as the driven element, a circular arc shaped reflector and six equal circular arc shaped directors. A parametric study on several antenna parameters, including the shape and the number of directors, is performed in order to meet specific project requirements (operating frequency, gain, HPBW and back-to-front ratio). After proper antenna optimisation using CST MWS, an antenna prototype designed to operate at 2.44 GHz has been fabricated in FR4 substrate. The

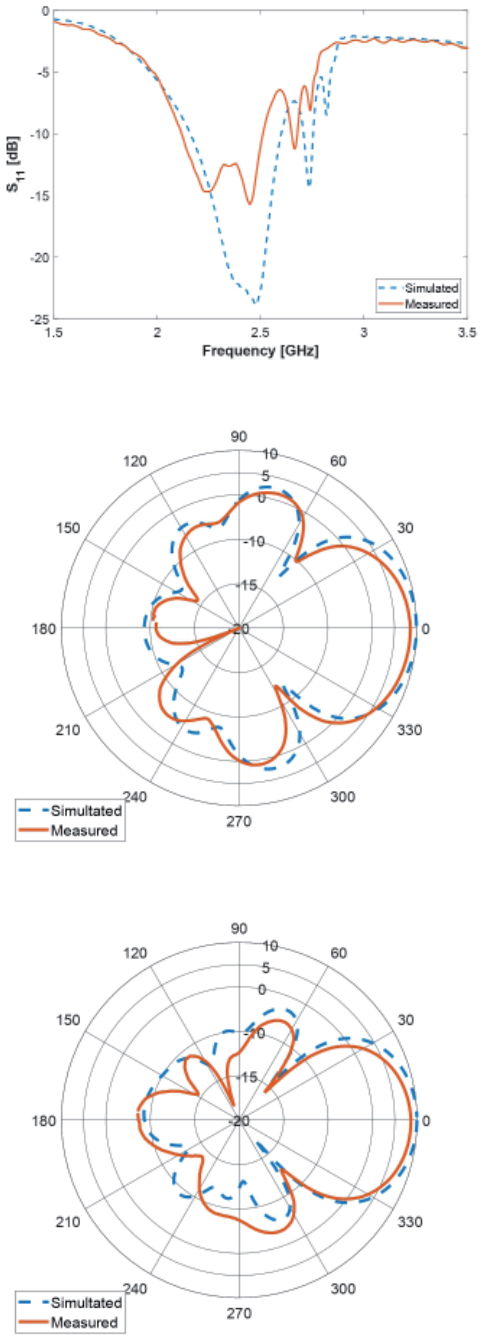

Figure 11. Simulated and measured results for the (a) S11-parameter and, radiation patterns at (b) azimuth and (c) elevation planes.

antenna presents overall dimensions of 175×61 mm^2. Further experimental characterisation carried out inside an anechoic chamber ensured a total gain of 8.6 dBi, a bandwidth of 390 MHz (from 2.12 to 2.51 GHz), HPBW of 64° in azimuth and 42° elevation planes, respectively, and a back-to-front ratio of 16.4 dB. Giving its technical characteristics and the end-fire radiation pattern, this antenna will enable the development of compact multi-sector base stations using circular array, as opposed to multiple flat panels, typically of large volumes, as the ones proposed in [22] and [23]. Further work will aim at antenna implementation in a multi-sector WSN base-station, composed of 6 Quasi-Yagi elements, which will be further tested in a real-world scenario, *i.e.* implemented in a wireless sensing network.

Acknowledgement

This research was partially under the project WSN-EM: PTDC/EEI-EEE/30539/2017 by FCT/MCTES through national funds, and when applicable, by EU funds under the project UID/EEA/50008/2021.

References

1. M. L. Laouira, A. Abdelli, J. B. Othman, and H. Kim, "An efficient WSN based solution for border surveillance," *IEEE Transactions on Sustainable Computing*, vol. 6, no. 1, pp. 54–65, jan 2021.

2. B. Montrucchio, E. Giusto, M. G. Vakili, S. Quer, R. Ferrero, and C. Fornaro, "A densely-deployed, high sampling rate, open-source air pollution monitoring WSN," *IEEE Transactions on Vehicular Technology*, vol. 69, no. 12, pp. 15 786–15 799, dec 2020.

3. O. B. Gonzalez and J. Chilo, "WSN IoT ambient environmental monitoring system," in *2020 IEEE 5th International Symposium on Smart and Wireless Systems within the Conferences on Intelligent Data Acquisition and Advanced Computing Systems (IDAACS-SWS)*. IEEE, sep 2020.

4. H. Luo, K. Wu, Z. Guo, L. Gu, and L. M. Ni, "Ship detection with wireless sensor networks," *IEEE Transactions on Parallel and Distributed Systems*, vol. 23, no. 7, pp. 1336–1343, jul 2012.

5. S. Astapov, A. Riid, and J.-S. Preden, "Military vehicle acoustic pattern identification by distributed ground sensors," in *2016 15th Biennial Baltic Electronics Conference (BEC)*. IEEE, oct 2016.

6. Y. Zhang, L. Sun, H. Song, and X. Cao, "Ubiquitous WSN for healthcare: Recent advances and future prospects," *IEEE Internet of Things Journal*, vol. 1, no. 4, pp. 311–318, aug 2014.

7. G. Hernandez-Penaloza, A. Belmonte-Hernandez, M. Quintana, and F. Alvarez, "A multi-sensor fusion scheme to increase life autonomy of elderly people with cognitive problems," *IEEE Access*, vol. 6, pp. 12 775–12 789, 2018.

8. D. D. K. Rathinam, D. Surendran, A. Shilpa, A. S. Grace, and J. Sherin, "Modern agriculture using wireless sensor

network (WSN)," in *2019 5th International Conference on Advanced Computing & Communication Systems (ICACCS)*. IEEE, mar 2019.

9. D. Qiong and P. Hao, "Design and implementation of irrigation water saving control system based on WSN," in *2021 International Conference on Intelligent Transportation, Big Data & Smart City (ICITBS)*. IEEE, mar 2021.

10. L. Shu, Y. Chen, Z. Sun, F. Tong, and M. Mukherjee, "Detecting the dangerous area of toxic gases with wireless sensor networks," *IEEE Transactions on Emerging Topics in Computing*, vol. 8, no. 1, pp. 137–147, jan 2020.

11. L. K. Ketshabetswe, A. M. Zungeru, M. Mangwala, J. M. Chuma, and B. Sigweni, "Communication protocols for Wireless Sensor Networks: a survey and comparison," *Heliyon*, vol. 5, no. 5, p. e01591, may 2019.

12. M. Appleby and F. Harrison, "47 -Cellular radio systems," in *Telecommunications Engineer's Reference Book*, F. Mazda, Ed. Butterworth-Heinemann, 1993, pp. 47–1–47–17.

13. T. E. S. Oliveira, J. R. Reis, M. Vala, and R. F. S. Caldeirinha, "High performance antennas for early fire detection wireless sensor networks at 2.4 GHz," in *2021 IEEE-APS Topical Conference on Antennas and Propagation in Wireless Communications (APWC)*. IEEE, aug 2021.

14. C. A. Balanis, *Antenna Theory: Analysis and Design, 3rd Edition*. John Wiley & Sons, 2005, vol. 72.

15. H. YAGI and S. UDA, "Projector of the sharpest beam of electric waves," *Proceedings of the Imperial Academy*, vol. 2, no. 2, pp. 49–52, 1926.

16. Y. Ding, Y. C. Jiao, P. Fei, B. Li, and Q. T. Zhang, "Design of a multiband quasi-Yagi-type antenna with CPW-to-CPS transition," *IEEE Antennas and Wireless Propagation Letters*, vol. 10, pp. 1120–1123, 2011.

17. K. D. Xu, D. Li, Y. Liu, and Q. H. Liu, "Printed quasi-Yagi antennas using double dipoles and stub-loaded technique for multi-band and broadband applications," *IEEE Access*, vol. 6, pp. 31 695–31 702, 2018.

18. A. Monti, J. Soric, A. Al`u, A. Toscano, and F. Bilotti, "Design of cloaked Yagi-Uda antennas," *EPJ Applied Metamaterials*, vol. 3, p. 10, 2016.

19. P. Aguila, G. Zamora, S. Zuffanelli, F. Paredes, F. Martin, and J. Bonache, "Reducing the width of planar Yagi-Uda antennas using square-shaped split ring resonators (SRRs)," in *2017 11th European Conference on Antennas and Propagation (EUCAP)*. IEEE, mar 2017.

20. C. Di Paola, S. Zhang, K. Zhao, Z. Ying, T. Bolin, and G. F. Pedersen, "Wideband beam-switchable 28 GHz quasi-Yagi array for mobile devices," *IEEE Transactions on Antennas and Propagation*, vol. 67, no. 11, pp. 6870–6882, 2019.

21. Y. Xu, Y. Dong, S. Wen, and H. Wang, "Vertically polarized quasi-Yagi MIMO antenna for 5G n78 band application," *IEEE Access*, vol. 9, pp. 7836–7844, 2021.

22. P. Liu, J. Zhang, S. Lu, and J. Lin, "Design and achievement of miniaturization in Wi-Fi base station antenna," in *Proceedings of 2014 3rd Asia-Pacific Conference on Antennas and Propagation*. IEEE, jul 2014.

23. J.-N. Lee, K.-C. Lee, and P.-J. Song, "The design of a dual-polarized small base station antenna with high isolation having a metallic cube," *IEEE Transactions on Antennas and Propagation*, vol. 63, no. 2, pp. 791–795, feb 2015.

A Simple Method for Calibrating GPS-Disciplined Clocks via Direct Comparison to a UTC(*k*) Time Scale

Michael A. Lombardi[1], Bijunath R. Patla[1], Andrew N. Novick[1], Demetrios Matsakis[2], and Stephen J. Mitchell[3]

[1]National Institute of Standards and Technology Boulder, CO, USA
E-mail: lombardi@nist.gov, bijunath.patla@nist.gov, novick@nist.gov

[2]Masterclock, Inc.
St. Charles, MO, USA
E-mail: dmatsakis@masterclock.com

[3]Applied Physics Laboratory (APL)
Johns Hopkins University
Laurel, MD, USA
E-mail: stephen.mitchell@jhuapl.edu

Abstract

Global-Positioning-System-(GPS) disciplined clocks are referenced to the Coordinated Universal Time (UTC) scale at the United States Naval Observatory (USNO), known as UTC(USNO). The UTC(USNO) time scale is a very close approximation of UTC, the official world time scale. GPS-disciplined clocks therefore provide a very close approximation of UTC when they are properly calibrated to compensate for equipment and cable delays. This paper provides a simple method for calibrating GPS-disciplined clocks with respect to UTC so they can replicate UTC with uncertainties of < 10 ns. The method involves directly comparing the device under test to any UTC(*k*) time scale listed on the weekly Rapid UTC (UTCr) reports published by the Bureau International des Poids et Mesures (BIPM).

1. Introduction

GPS-disciplined clocks (GPSDCs) produce a one-pulse-per-second (pps) output that is referenced to UTC(USNO), the Coordinated Universal Time (UTC) scale operated by the United States Naval Observatory (USNO). In nearly all cases – unless the antenna cable is unusually long or if the antenna coordinates have a very large error – an uncalibrated GPS-disciplined clock should agree with UTC(USNO) to within less than 1 µs, with ~100 ns accuracy being a typical specification. However, even when short antenna cables are used and even when the antenna coordinates have been determined to within less than 1 m, getting the best available accuracy from a GPS-disciplined clock still requires measuring and calibrating all hardware delays. The antenna cable typically introduces the largest delay, but the GPS receiver and its associated electronics and firmware, as well as the antenna itself, will also introduce delays. Once these delays are determined, a delay constant can be keyed into the GPS-disciplined clock to correct the 1 pps output. Within the semantic framework of the *International Vocabulary of Metrology* [1], the determination of the delays and their respective uncertainties is accomplished by calibration, and the correction of the delay in the GPS-disciplined clock is accomplished by adjustment. After a GPS-disciplined clock has been both calibrated and adjusted, it can be utilized as a true UTC synchronization source.

Several methods of GPS delay calibrations are routinely practiced. Some methods involve measuring the cable, receiver, and antenna delays separately, and then appropriately accounting for all delays, but some parts of this process can be difficult. For example, methods for measuring cable delays are well established [2, 3], but measuring receiver delays might require the use of a GPS simulator [4, 5]. Antenna-delay measurements might be even more involved, requiring the use of a network analyzer and an anechoic chamber. For these reasons, it is common and usually preferable to calibrate a GPS-disciplined clock as a system that includes the receiver, antenna, and antenna cable, and obtaining a single delay value that accounts for the entire system. This is usually done by simultaneously comparing both the GPS-disciplined clock under test and a previously calibrated reference GPS-disciplined-clock system, each connected to antennas separated by a short distance, to the same clock [6]. The comparisons usually last for about three to 10 days, with one week being typical. The reference GPS-disciplined-clock system is assumed to

be correct, and thus the average time difference between the two units is attributed to the GPS-disciplined clock under test.

This paper introduces a simple method that retains the advantage of calibrating GPS-disciplined clocks as a system, but that eliminates the need for a reference GPS-disciplined clock. This is advantageous because the reference GPS-disciplined clock contributes uncertainty to the measurement, and because in many cases the reference GPS-disciplined clock is a unit maintained elsewhere that must travel to the site of the calibration. The method described here consists of directly comparing the GPS-disciplined clock under test to any UTC(k) time scale listed on the Rapid UTC (UTCr) reports that are published weekly by the Bureau International des Poids et Mesures (BIPM), and then applying a UTCr correction to the measurement. The new method works because of the very close agreement between UTC, UTCr, UTC(USNO), and GPS time. It is viable to implement because the UTC(USNO) time scale provides the time reference for GPS, and because daily UTCr – UTC(USNO) results are freely available via the BIPM. For the purposes of this paper, the method is called the GUC method, an acronym for GPS/UTC calibration.

Section 2 provides a short discussion of the close relationship between UTC, UTCr, UTC(USNO), and the time broadcast by the GPS satellites. Section 3 explains the GUC method, including the application of UTCr data. Section 4 provides and discusses measurement results from several GPS-disciplined clocks calibrated with this method at the National Institute of Standards and Technology (NIST). Section 5 discusses the measurement uncertainty of the delay calibrations, and Section 6 provides a summary.

2. The Relationship Between UTC, UTCr, UTC(USNO), and the Time Broadcast by GPS

Time calibrations, as is the case with nearly all metrological calibrations, should be referenced and traceable to the International System of Units (SI). The base unit for time is the second (s), one of the seven base units of the SI. The ultimate reference for establishing traceability for time calibrations is Coordinated Universal Time (UTC), an atomic time scale that provides the world's best approximation of the SI second [7]. UTC is computed by the BIPM from a weighted average of data collected from local time scales, known as UTC(k), that are located at national metrology institutes or other facilities that have legal or technical timekeeping responsibilities.

The UTC(k) time scales produce signals that can serve as a reference for physical measurements, whereas UTC does not. Instead, UTC is defined by regularly publishing the time difference, UTC – UTC(k), for each institution that contributes to UTC. The official time differences are published monthly in the BIPM *Circular T*,

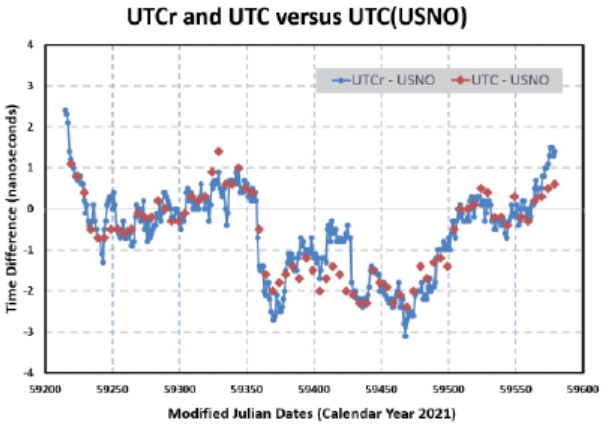

Figure 1. Time differences for UTC – UTC(USNO) and UTCr – UTC(USNO) for calendar year 2021.

which provides UTC – UTC(k) values at five-day intervals [8]. Since July 2013, the BIPM has also published weekly UTCr – UTC(k) time differences, with values provided at one-day intervals [9].

The UTC(USNO) time scale is the largest contributor to UTC, and as previously noted, provides a very close approximation of UTC. This is illustrated in Figure 1, which shows both the UTC – UTC(USNO) and UTCr – UTC(USNO) time differences for the calendar year 2021. The graph indicates UTC(USNO) did not depart from UTC by more than ±4 ns at any point during 2021, with the average UTC – UTC(USNO) and UTCr – UTC(USNO) time differences being –0.58 ns and –0.62 ns , respectively. The largest difference between the UTC and UTCr comparisons, for the days spaced at five-day intervals when both values were available, was 1.4 ns, with the average difference being –0.03 ns . This suggests that the results of UTCr, while non-official, agree closely with the results published later in the *Circular T* and are suitable for use for GPS-disciplined clock-delay calibrations, as described in Section 3.

The close approximation of UTC(USNO) to UTC is advantageous to GPS, because GPS broadcasts a prediction of UTC(USNO). Even though GPS has its own time scale, known as GPS time, the satellites broadcast UTC correction parameters in subframe 4, page 18, of the navigation message. Nearly all GPS-disciplined clocks apply these parameters and convert GPS time to a prediction of UTC(USNO). The UTC offset correction, Δt_{UTC} , is computed as [10]

$$\Delta t_{UTC} = \Delta t_{LS} + A_0 + A_1\left[t_E - t_{0t} + 604800\left(WN - WN_r\right)\right] \quad (1)$$

where

Δt_{LS} is the number of leap seconds introduced into UTC since the beginning of the GPS epoch (January 6, 1980),

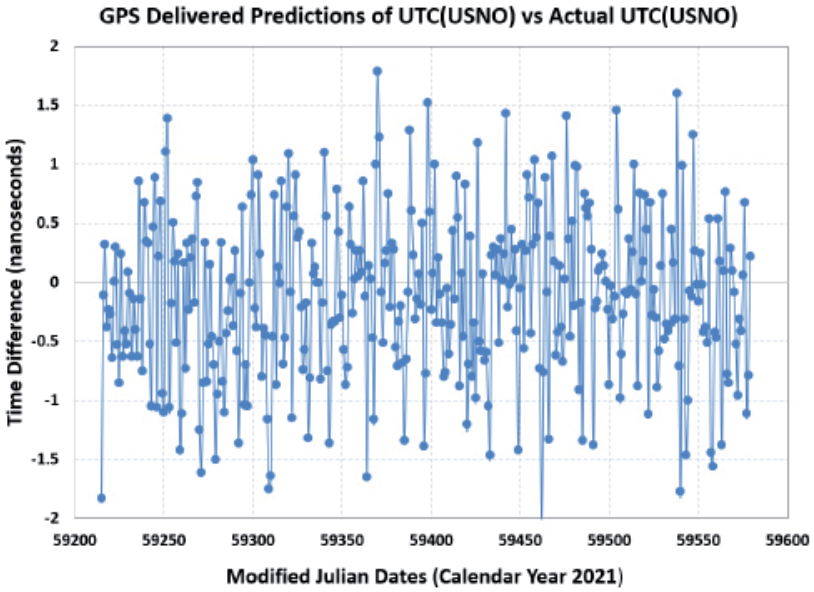

Figure 2. GPS delivered predictions of UTC(USNO) compared to actual UTC(USNO) for 2021.

A_0 is the constant UTC offset parameter expressed in seconds,

A_1 is a dimensionless frequency-offset value that allows the correction of the time error accumulated since the UTC reference time, t_{0t}, which is when A_0 was last determined,

t_E is GPS system time (the time to be converted to UTC(USNO)),

604800 is a constant that equals the number of seconds in one week,

t_{0t} is the reference time for UTC data,

WN is the GPS week number, and

WN_t is the UTC reference week number.

The Δt_{LS} term is the large, integer-second part of the correction, equal to the number of leap seconds that have occurred since the beginning of the GPS epoch (January 5, 1980). The A_0 term is the small, nanosecond part of the correction, equal to the difference between the GPS and UTC(USNO) second markers. It is broadcast in units of seconds, but is typically $<1\times10^{-8}$ s, or <10 ns in magnitude. The fine tuning of the UTC output of a GPS-disciplined clock is accomplished by applying a dimensionless frequency offset, provided by A_1, as a drift correction for the interval between the time specified by t_{0t} and WN_t and the current time. This is normally a sub-nanosecond correction, because A_0 is normally updated in the GPS broadcast more than once per day and the drift correction supplied by A_1 is typically near 1 ns per day.

The UTC(USNO) prediction broadcast by GPS is based upon an extrapolation of the observed difference

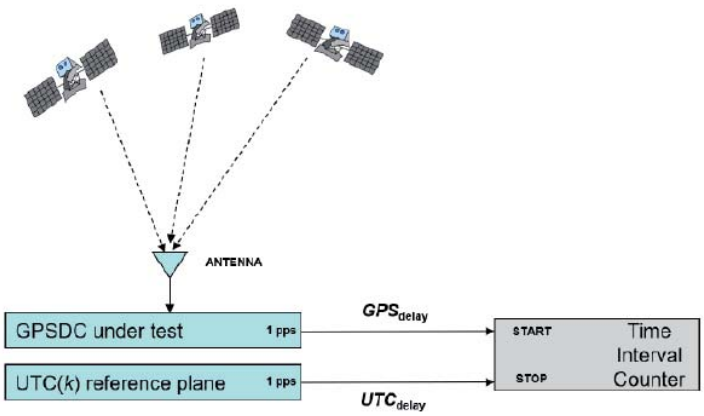

Figure 3. The GPSDC – UTC(*k*) time-difference measurement.

Table 1. The sample calibration of a GPS-disciplined clock at NIST using UTCr report 2152 (values are in nanoseconds).

MJD	UTCr – UTC(USNO)	UTCr – UTC(NIST)	GPSDC – UTC(*k*)	GPSDC delay bias, GPS_{db}
59575	1.3	1.3	85.5	85.5
59576	1.5	1.4	86.8	86.9
59577	1.5	1.4	87.1	87.2
59578	1.3	1.4	84.1	84.0
59579	1.4	1.6	84.5	84.3
59580	1.4	1.4	86.8	86.8
59581	1.5	1.6	85.3	85.2
Average delay (applied to GPSDC after calibration)				85.7

between GPS and UTC(USNO) from the start to the end of the previous day. Figure 2 shows the differences between the GPS-delivered predictions of UTC(USNO) and actual UTC(USNO) daily averages for calendar year 2021. The GPS – UTC(USNO) time differences fall within a ±2 ns range and have a mean value of -0.1 ns . The very close agreement between UTC(USNO) and the time broadcast by the GPS satellites provides the foundation for the simple GUC method described in Section 3.

3. The GUC Calibration Method

The GUC delay calibration method consists of comparing the 1 pps output of the GPS-disciplined clock under test to a 1 pps output of any UTC(*k*) time scale included on the weekly UTCr reports. Because the GPS-disciplined clock is being calibrated as a system (receiver, antenna, antenna cable), it should be measured with its delay compensation equal to 0, in other words, no previously measured or estimated delay values should be keyed into the unit. The comparisons are typically done with a time-interval counter (TIC), as shown in Figure 3.

If the two cables that connect the GPS-disciplined clock to the time-interval counter and the UTC(*k*) reference plane to the time-interval counter do not have equivalent delays, then the raw time-interval counter readings must be corrected. Assuming that the GPS-disciplined clock is connected to the start channel on the time-interval counter and UTC(*k*) is connected to the stop channel, as shown in Figure 3, each time-interval counter reading is corrected as

$$TIC_{corr} = TIC_{raw} - UTC_{delay} + GPS_{delay}, \qquad (2)$$

where TIC_{raw} is the uncorrected reading from the time-interval counter, UTC_{delay} is the cable delay between the UTC(*k*) reference plane and the time-interval counter, and GPS_{delay} is the cable delay between the 1 pps output of the GPS-disciplined clock and the time-interval counter. The corrected time-interval counter readings (TIC_{corr}) are a measurement of GPS-disciplined clock – UTC(*k*). These readings can be recorded every second, but the data points used for the calibration should be one-day averages. Daily averages are required because UTCr only provides one value per day, and also have the benefit of attenuating diurnal variations caused by ionospheric or environmental factors. The daily averages should ideally be recorded for a period of at least seven days that corresponds to the period of a UTCr report. The last day of a UTCr report is always a Sunday and the reports are published on Wednesdays. This means that the GPS-disciplined clock delay calibration cannot be completed until a few days after the most recent measurement when the UTCr report becomes available.

The equation to compute the delay bias in a GPS-disciplined clock, GPS_{db}, for a given day is

$$GPS_{db} = \left[\left(UTCr - UTC_{USNO}\right) - \left(UTCr - UTC_k\right)\right] + \left(GPSDC - UTC_k\right), \qquad (3)$$

where $\left(UTCr - UTC_{USNO}\right)$ and $\left(UTCr - UTC_k\right)$ are obtained from the UTCr report, and $\left(GPSDC - UTC_k\right)$ is obtained from the time-interval counter measurements.

Table 1 provides an example where a GPS-disciplined clock was measured at NIST in Boulder, Colorado. In this example, the UTC(NIST) time scale served as UTC(*k*), and correction data were obtained from UTCr report 2152 (published on January 5, 2022). A delay constant of 0 was used in the GPS-disciplined clock under test, meaning that all hardware delays, including antenna cable delays, were unaccounted for and ignored. The purpose of the calibration was to obtain a single delay value that could be keyed into the GPS-disciplined clock to compensate for its hardware delays, and therefore make the GPS-disciplined clock produce signals that agreed with UTC as closely as possible.

Note that in this example, the close agreement between the UTC(USNO) and UTC(NIST) time scales meant the corrections obtained from UTCr and applied to the

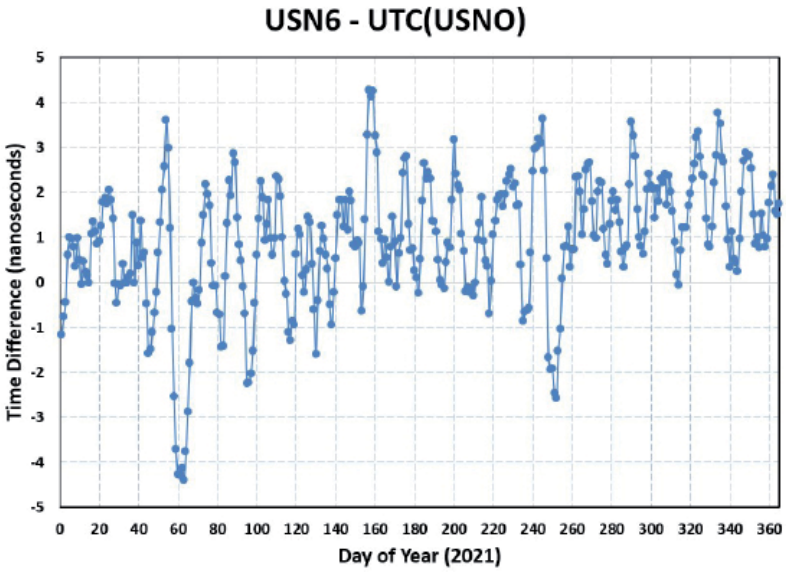

Figure 4. Time differences for the reference USN6 GPS receiver – UTC(USNO) for calendar year 2021.

calibration were sub-nanosecond. A direct comparison of the GPS-disciplined clock to UTC(NIST) would therefore have produced nearly the same results. For GUCs performed at other UTC(*k*) laboratories, the UTCr corrections would likely be larger. For example, if UTC(USNO) – UTC(*k*) as obtained from the UTCr report had an average time difference of 20 ns, then a GPS-disciplined clock compared to UTC(*k*) should also have an average time difference of 20 ns after it had been calibrated. The GUC method calibrates devices to agree with UTC and not with UTC(*k*), and the method is viable because the differences between UTC and UTC(*k*) are published.

4. Calibration Results

One way to test the validity of the GUC method is to use it to check for biases in reference GPS time-transfer receivers that have been previously calibrated with other more-established methods. The first, most-basic check, was done by comparing USN6, a reference GPS receiver at the USNO, to the UTC(USNO) time scale for the entire year of 2021 (Figure 4). The average time difference of this comparison should be near 0 (as previously indicated by the data shown in Figure 2) if the GPS device has been properly designed and calibrated. As expected, despite daily peak-to-peak variations that sometimes reached ±4 ns, the

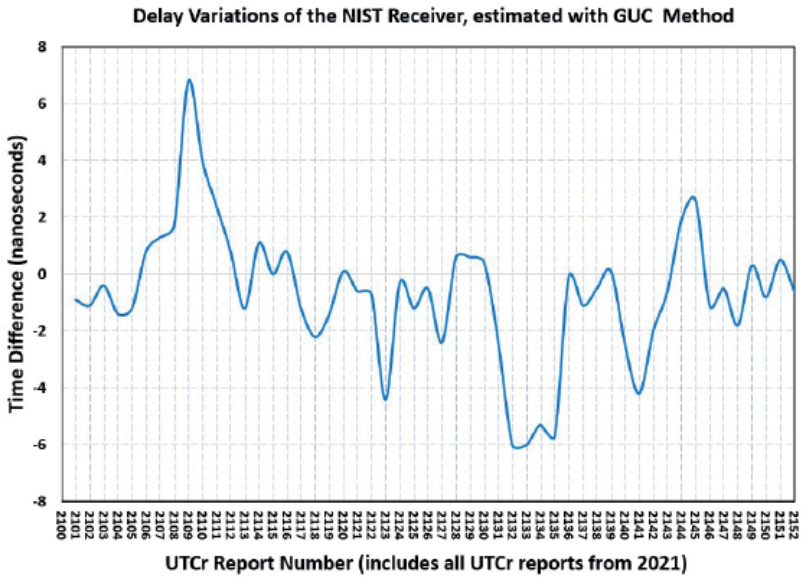

Figure 5. Post-calibration delay variations of the NIST receiver, estimated with the GUC method, for calendar year 2021.

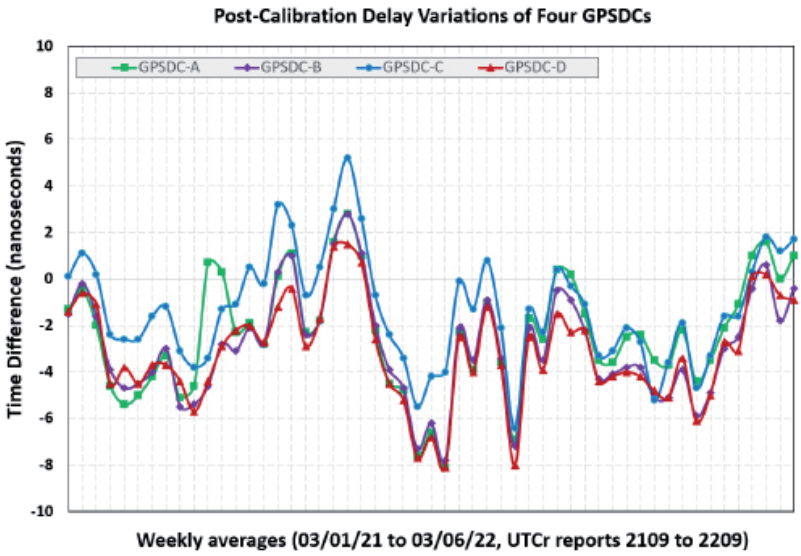

Figure 6. Post-calibration delay variations of four single-frequency (L1 band) GPS-disciplined clocks during a one-year interval.

average time difference for 2021 was just 1.0 ns, indicating only a small calibration bias.

A second test of the GUC method involved a comparison for the year 2021 involving a reference receiver at NIST, which was previously (and periodically) calibrated via the BIPM calibration program. Here, the GUC method was applied to estimate post-calibration delay biases as shown in Figure 5. Daily variations occasionally exceeded ±5 ns, but the average time difference for 2021 was 0.7 ns.

During the first two months of 2021, the GUC method was used to calibrate four low-cost single-frequency (L1 band) GPS-disciplined clocks at NIST. These calibrations were not all performed simultaneously – no more than two were in progress at one time – and each lasted for about two weeks (at least two full UTCr reports were used for each calibration). After these calibrations were completed, the four GPS-disciplined clocks were allowed to run undisturbed for an entire year, and the GUC method was then again applied to the collected data. Figure 6 shows the post-calibration delay variations of the four GPS-disciplined clocks for the approximate one-year period from March 1, 2021,through March 6, 2022 (via UTCr reports 2109 through 2209; 53 full one-week reports were used). Although the daily delay variations were different, the average delay bias for GPS-disciplined clock-C (which utilized different receiver hardware than the other three units), was −0.8 ns for the approximate one-year interval, differing by just 0.3 ns from the NIST reference receiver over the same interval. The other three units (A, B, and D) used identical hardware. As such, their daily values closely tracked each other, and their average values for the one-year interval were nearly the same: −3.1 ns, −3.3 ns, and −3.4 ns, respectively. Units A, B, and D each differed by nearly 3 ns from the NIST reference receiver.

Figure 6 indicates that after the original approximate two-week GUC calibration, all four of the GPS-disciplined clocks under test were still "biased low" with respect to UTC, with GPSDC-C having the smallest bias and the other three units grouped closely together. No calibration can eliminate the inevitable daily delay fluctuations, but long-term calibrations can do a better job of centering the fluctuations around zero by removing the bias of seasonal effects. The delay values of each of the four GPS-disciplined clocks in Figure 6 were thus subsequently adjusted to remove the revealed calibration biases, allowing the one-year observation period to serve as a lengthy recalibration with a smaller uncertainty. This is shown in Figure 7, which includes data for the next six UTCr reports (2210 to 2215) after the calibration biases were removed. The average values for this six-week period then all showed sub-nanosecond agreement with UTC, with values of 0.7 ns, −0.5 ns, 0.1 ns, and −0.5 ns for units A, B, C, and D, respectively.

5. Factors that Limit the Measurement Uncertainty of GUC Calibrations

The time differences of the GPS time signal with respect to UTC(USNO) are tightly controlled, as shown in Figure 2, but GPS-disciplined clocks will produce larger time deviations, as indicated by the data shown in Figures 4, 5, and 6. These deviations can be attributed either to factors that affect the GPS signal as it propagates from the satellite to the receiving system's antenna, or to delay changes within the receiving system itself. For the purposes of this brief discussion, uncertainties related to GPS signal propagation can be labeled as U_P. These include uncertainties in the broadcast ionospheric delay corrections

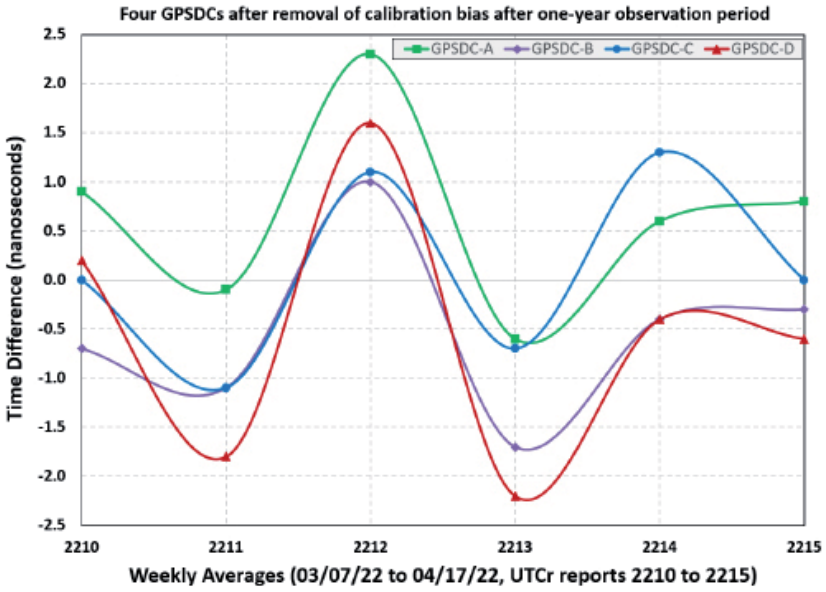

Figure 7. Delay variations of four single-frequency (L1 band) GPS-disciplined clocks during a six-week interval after calibration bias was removed following a one-year observation period.

that are applied by GPS-disciplined clocks, as well as multipath signal reflections, solar activity, tropospheric activity (weather), and other factors that can cause propagation delays to change. Environmental conditions, such as changes in both indoor and outdoor temperature that can cause hardware delay changes, are labeled as U_E . For example, outdoor temperature and conditions such as snow on the antenna can change the delay of receiving antennas or cables. Indoor temperature often has a larger effect, especially in the case of GPS-disciplined clocks with low-cost local oscillators, such as those graphed in Figure 6. In fact, both indoor and outdoor temperatures likely contributed to the approximate 3 ns bias in units A, B, and D, as they were calibrated during the months of January and February, winter months in Boulder, Colorado. Some amount of delay variation both during and after the calibration is inevitable in all GPS-disciplined clocks, regardless of whether the GUC method or another calibration method is utilized, and it seems reasonable and pragmatic to evaluate both U_P and U_E as Type B uncertainties, and to conservatively assign a value of 3 ns to each

The other factors that must be considered in the uncertainty analysis of the GUC method are the uncertainties of the links that UTC(USNO) and UTC(k) utilize to send their data to the BIPM, which can be labeled as U_{USN} and U_{UTK} , respectively. These uncertainties are provided by the BIPM in Section 1 of the *Circular T*. For purposes of example, we used the January 2022 *Circular T* where U_{USN} was reported as 1.6 ns. If we selected UTC(NIST) as UTC(k), then U_{UTK} was reported as 2.3 ns. We could also assign an uncertainty of 1 ns to U_{UG} , or the difference between UTC(USNO) and the prediction of UTC(USNO) broadcast by GPS (obtained by rounding up from the average time difference shown in Figure 2). Using standard methods for uncertainty analysis [11] and the aforementioned values, we estimated the combined uncertainty, U_c , of the calibration method via UTC(NIST) as

$$U_c = k\sqrt{U_P^2 + U_E^2 + U_{USN}^2 + U_{UTK}^2 + U_{UG}^2}$$

$$= 2\sqrt{3^2 + 3^2 + 1.6^2 + 2.3^2 + 1^2} = 10.4 \text{ ns.} \qquad (4)$$

The coverage factor of $k = 2$ indicates that the coverage probability was 95.45%. This represents the probability that a daily measurement value was within the coverage interval. All of the post-calibration delay variations shown in Figures 4, 5, and 6 were well within a ±10 ns interval, suggesting that an approximate 10 ns uncertainty for a one-day average value was probably overestimated. The statistical (Type A) measurement uncertainty from a GUC calibration averaged across multiple days should improve by a factor of $\sqrt{N}$, where N is the number of days of the calibration. However, the systematic (Type B) uncertainties, such as the uncertainties in the BIPM links or GPS-disciplined clock antenna coordinate errors, will not be reduced by a longer calibration. Even so, for a seven-day calibration based on a single UTCr report, U_c should be ~5 ns ($k = 2$) in this example, and if three UTCr reports are used for a 21-day calibration, U_c should be reduced to < 4 ns ($k = 2$).The combined uncertainty, U_c , is with respect to UTC. As previously noted, the actual number of days required to complete the calibration will be N plus the days elapsed before UTCr is published (the last value shown on a UTCr report is for Sunday and publication is on Wednesday).

6. Summary

This paper has presented a simple method for the delay calibration of GPS-disciplined clocks, introduced here as the GUC method (GPS/UTC calibration). The GUC method can be utilized by any laboratory with a UTC(*k*) time scale. It has the advantage of not involving a reference GPS-disciplined clock, which potentially reduces the uncertainty of the measurements. The foundation for the method is the very close agreement between UTC, UTCr, UTC(USNO), and the time broadcast by the GPS satellites. The GUC method allows UTC(*k*) providers to calibrate GPS-disciplined clocks with respect to UTC, and to establish calibration services for industrial partners. It may also be useful for periodic recalibration of any secondary time-transfer receivers located at UTC(*k*) laboratories that do not serve as their primary link to UTC, and for continuous post-calibration verification of primary links.

7. References

1. Joint Committee for Guides in Metrology (JCGM), *International Vocabulary of Metrology – Basic and General Concepts and Associated Terms, VIM, Third Edition*, JCGM 200, 2012.

2. G. de Jong, "Measuring the Propagation Time of Coaxial Cables Used with GPS Receivers," Proc. of the 17th Annual Precise Time and Time Interval (PTTI) Systems and Application Meeting, December 1985, pp. 223-232.

3. D. Rovera, M. Abgrall, P. Uhrich, and M. Siccardi, "Techniques of Antenna Cable Delay Measurement for GPS Time Transfer," Proc. of the 2015 Joint Conference of the IEEE International Frequency Control Symposium and the European Frequency and Time Forum, Denver, Colorado, April 2015, pp. 239-244.

4. G. Petit, Z. Jiang, J. White, R. Beard, and E. Powers, "Absolute Calibration of an Ashtech Z12-T GPS Receiver," *GPS Solutions*, **4**, 4, April 2001, pp. 41-46.

5. J. Plumb, K. Larson, J. White, and E. Powers, "Absolute Calibration of a Geodetic Time Transfer System," *IEEE T. Ultrason. Ferr.*, **52**, 11, November 2005, pp. 1904-1911.

6. W. Lewandowski, J. Azoubib, and W. Klepczynski, "GPS: Primary Tool for Time Transfer," *Proceedings of the IEEE*, **87**, 1, January 1999, pp. 163-172.

7. D. Matsakis, J. Levine, and M. Lombardi, "Metrological and Legal Traceability of Time Signals," Proc. of the 2018 Precise Time and Time Interval Meeting (ION PTTI 2018), January 2018, pp. 59-71.

8. BIPM Time Department, "Circular T, available monthly (from 1996 to present) at: https://www.bipm.org/en/time-ftp/circular-t .

9. BIPM Time Department, "UTCr," available weekly (from 2013 to present) at: https://www.bipm.org/en/time-ftp/utcr .

10. Global Positioning Systems Directorate, "Navstar GPS Space Segment/Navigation User Interfaces," Interface Specification IS-GPS-200H, 2013.

11. Joint Committee for Guides in Metrology (JCGM), "Evaluation of Measurement Data – Guide to the Expression of Uncertainty in Measurement," JCGM 100, 2008.

On the Radar Cross Section of Dragons

Stefano Selleri

Department of Information Engineering
University of Florence
Via di S. Marta, 3 – I50139 Florence, Italy
E-mail: stefano.selleri@unifi.it

Abstract

An assessment is given of the possibility of detecting and recognizing dragons based on their radar cross section.

It is somewhat assessed that no dragon has been reported in nature since a few centuries. However, scientific papers on dragons with careful investigations are not limited to the Middle Ages [1, 2] or the Renaissance [3, 4]. Recent accurate papers on the ecology of dragons have appeared in the XX and XXI centuries in international referred journals [5-7].

While [5] and [6] do treat the general ecology and evolution of dragons, dividing them into two broad families, those with four limbs (either four legs or two wings and two legs) which should, evolutionarily speaking, belong to our own Tetrapoda superclass; and those with six limbs (two wings and four legs), which albeit being of course to Chordata must have separated from our clade much earlier. Of course, this is not to speak of multi-headed or multi-tailed dragons.

The reason why there are no dragons recorded in the wild might be attributed to their extinction somewhere around A.D. 1300, and this could be due to several factors [7]:

1. A general cooling of the world's climate, which was in a transition from the Medieval Warm Period to the Little Ice Age (Figure 1).

2. The shortage of food. The end of Chivalry and the advent of gunpowder lead to a scarcity of armored knights [9], which, together with princesses, were a dragon's preferred meal (Figure 2)[1].

To these reasons we might add a third:

3. The passage from an economy based solely on gold and silver, hoarded by dragons, to more evolved financial instruments, like the promissory note, introduced early in the XIV century, which diminished the possibility for dragons to haul treasures.

However, as stated in [6], a dragon's life span is in the range of 10^3 to 10^4 years and in the r- or K- strategy, they surely belong to the extreme K-selection strategy, with

[1] Indeed, sheep-eating and peasant-eating dragons have also been reported [5].

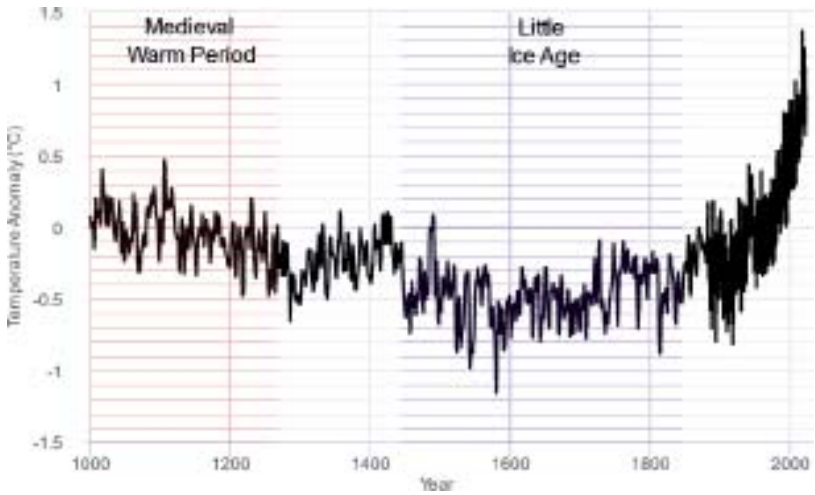

Figure 1. Global temperature variations with respect to the average value according to 2° institute [8]. What is conventionally called the "Medieval Warm period" [950-1250] and the "Little Ice Age" [1430-1850] are highlighted.

Figure 2. "Saint George Slays a Dragon" (Paolo Uccello, ca. 1460, oil on canvas, National Gallery, London, public domain). This is a tetrapod dragon not having a meal, but being captured by the princess, who binds the dragon with her belt after Saint George has wounded him.

very little offspring and long parental care. Furthermore, dragons are closer to reptiles, and supposedly ectothermic beasts [7], which means that, in very cold climates they can enter a period of *brumation* (which is the equivalent of the *hibernation* of dormice, bears, and other endothermic beasts).

Existing reptiles may eat more than usual before the brumation time, but eat less or refuse food as the temperature drops, and they can go for months without food. The brumation period is anywhere from one to eight months, depending on the air temperature and the reptile species [10].

If reptiles with lifespan less than 10^2 can remain dormant for two-thirds of a year, then it can be inferred that dragons can withstand centuries of brumation, occasionally emerging to life [7] but, due to the ongoing Little Ice Age, staying mostly dormant.

Now, global warming has indeed already raised temperatures well above the maximum of the Medieval Warm Period, so we might expect dragons to return active, searching for food and treasures. We therefore should be ready to spot them on our early surveillance radars, and we should focus on the radar signature of a dragon, to distinguish it from man-made flying objects.

We shall suppose that the dragon has slept for centuries over his treasure, mostly gold and silver. It is well known [11, 12] that dragons prefer to cover their body with these metals, especially their soft belly, to enhance their resistance to spears, arrows, and swords. We can hence safely assume that dragons are good conductors and compute their radar cross section (RCS) as if they were perfect electric conductors, with a minimum approximation.

Figure 3. A three-dimensional dragon model (available from *cgtrader*, authored by Dommk and released under royalty-free license [18]).

Furthermore, dragons are big, and like most big flying animals, should rely on gliding rather than on flapping-wing flight. This is true for the albatross, which, being the largest flying bird, has a maximum wingspan of 12 ft [13]. The same was most probably true for Pteranodons, whose wingspan exceeded 18 ft[14].

Dragons, which are reported to have been larger than any of the above-mentioned flying beings[2], must glide most of the time and also exploit ascensional currents. We hence can also neglect wing movements and focus on the radar cross section of a non-flapping gliding dragon.

Figure 3 represents a three-dimensional model of a six-limbed dragon among those various freely available. It is a good example and full of details, horns, spikes, claws, torn leathery wings. The dragon wingspan was about 35 ft, comparable to that of a Piper PA-18. We checked the RCS of the beast against that of the plane.

Figure 4 finally presents results, computed via physical optics [19], of the RCS of the two targets. It is apparent how the large flat surfaces characterizing the plane's fuselage and wings caused high RCS values (up to $30\ \mathrm{dBm}^2$) in very specific directions, whereas the curved, organic shape of the dragon led to a lower peak and less direction-dependent RCS.

Distinguishing a gliding dragon from an airplane on the basis of its RCS hence seems possible, as well as their disposal via AAM or SAM, even with infrared homing, since fire breathing dragons are expected to internally match the temperature of a jet engine, with the notable difference that the mouth is in the front of the creature while the engines are on the back of a plane.

[2] In [1] it was described how dragons wrestle elephants, while in [2] the fine art of saddling and bridling wild dragons was elucidated. In [15, 16] dragon-riding was uncommon but not unheard of, while in [12, 17] dragons were never ridden and Fell Beasts were the steeds of Nazgûls.

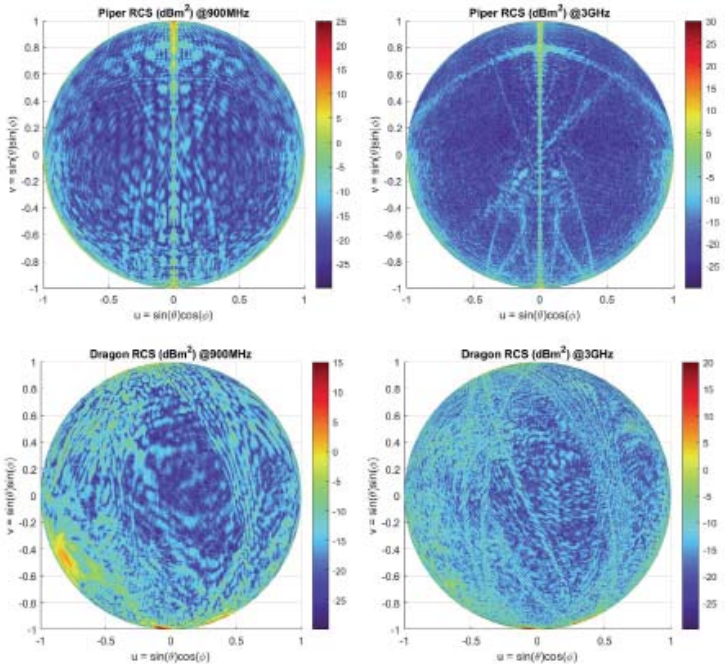

Figure 4. The RCS for the Piper (top row) and dragon (bottom row) at 900 MHz (first column) and 3 GHz (second column). The *z* axis corresponds to the axis of the plane and of the dragon.

We can hence sleep easy: our current defense systems should also be adequate against dragons.

References

1. Bartholomaeus Anglicus, *De proprietatibus rerum*, manuscript, c. 1240.

2. R. Bacon, *Opus Majus*, manuscript, c. 1267.

3. G. K. Kirchmaier, *Disputationum zoologicarum: publice ante hac habitarum, de basilisco, unicornu, phoenice, behemoth & leviathan, dracone, ac araneâ, hexas*, Wittebergae: Sumptibus haered. Johannisbergeri, typis haered Melchioris Oelschlegelii, 1661.

4. U. Aldovrandi, *Serpentum, et draconum historiae libri duo*, Bologna, Clementem Ferronium, 1640.

5. P.J. Hogarth, "Ecological Aspects of Dragons," *Bulletin British Ecological Society*, **7**, 2, 1976, pp. 2-5.

6. R. M. May, "The Ecology of Dragons," *Nature*, **264**, November 4, 1976, pp. 16-17.

7. A. J. Hamilton, R. M. May, E. K. Waters, "Here be Dragons," *Nature*, **520**, April 2, 2015, pp. 42-43.

8. https://www.2degreesinstitute.org/ - https://www.temperaturerecord.org/

9. S. Selleri, "On the Electromagnetic Shielding Effectiveness of Chain-Mail Armor," *URSI Radio Science Bulletin*, No. 367, 2018, pp. 9-11.

10. https://www.britannica.com/science/dormancy/Dormancy-in-cold-blooded-vertebrates

11. J. R. R. Tolkien, *The Hobbit*, London, George Allen & Unwin., 1937.

12. J. R. R. Tolkien, *The Silmarillion*, [C. Tolkien ed.] Boston, Houghton Mifflin, 1977.

13. D. Stone, "Albatross's Effortless Flight Decoded –May Influence Future Planes," National Geographic, September 9, 2012.

14. K. Padian, "A Functional Analysis of Flying and Walking in Pterosaurs," Paleobiology, **9***, 3, 1983, pp. 218-239.*

15. *G. R. R. Martin, A Song of Ice and Fire*, New York, Bantam, 5 volumes, 1996, 1999, 2000, 2005, 2011.

16. C. Paolini, *The Inheritance Cycle*, New York, Alfred A. Knopf, 4 volumes, 2003, 2005, 2008, 2011.

17. J. R. R. Tolkien, *The Lord of the Rings* (originally published in three volumes), London, George Allen & Unwin., 1954-1955.

18. https://www.cgtrader.com/free-3d-models/animals/other/dragon-3d-model

19. G. T. Ruck, D. E. Barrick, W. D. Stuart, C. K. Krichbaum, *Radar Cross-Section Handbook, Volumes 1 and 2*, New York, Plenum Press, 1970.

SCOSTEP's New Research Program: "Predictability of Variable Solar-Terrestrial Coupling (PRESTO)"

J. L. Chau[1] and C. J. Rodger[2]

[1]Leibniz Institute of Atmospheric Physics at the University of Rostock
Kühlungsborn, Germany
E-mail: chau@iap-kborn.de

[2]Department of Physics, University of Otago
Dunedin, New Zealand
E-mail: craig.rodger@otago.ac.nz

Abstract

The Scientific Committee on Solar Terrestrial Physics (SCOSTEP) has recently launched its latest five-year scientific program, " Predictability of Variable Solar-Terrestrial Coupling (PRESTO)." This program is intended to last from 2020 through 2024. URSI is one of SCOSTEP's formal participating bodies, and provides a representative to the Bureau that governs SCOSTEP. Through this route, URSI was involved in the selection of the projects that formed the PRESTO program. The scientific goals of PRESTO are relevant to a wide range of URSI members, and in particular to those from Commissions E, F, G, H, and J. In this brief article, we wish to alert the URSI community to PRESTO and its pillars.

1. Background Information

The Scientific Committee on Solar-Terrestrial Physics (SCOSTEP) is a thematic body of the International Science Council (ISC [1]). SCOSTEP promotes ISC's mission to strengthen international science for the benefit of society. SCOSTEP runs international interdisciplinary scientific programs and promotes solar-terrestrial physics research by providing the necessary scientific framework for international collaboration and dissemination of the derived scientific knowledge in collaboration with other ISC bodies.

SCOSTEP is a permanent observer at the United Nations Committee on the Peaceful Uses of Outer Space (COPUOS [2]). SCOSTEP was originally established as an Inter-Union Commission, following a resolution adopted at the 11th General Assembly of ICSU (International Council for Science) in Bombay in January 1966. It was modified by the 14th General Assembly of ICSU in Helsinki in 1972 to become a Special Committee, and by the 17th General Assembly in 1978 to become a Scientific Committee.

The governing body of SCOSTEP is the SCOSTEP Bureau. The Bureau is comprised of SCOSTEP's President, Vice President, and Past President; the representatives of the ISC Participating Bodies; and the Scientific Secretary (ex-officio). The Bureau directs scientific, administrative, and financial activities. URSI [3] is one of the participating bodies inside SCOSTEP, and thus contributes a representative to the Bureau. The current URSI representative to SCOSTEP is Jorge L. Chau (Germany), who took up the role before the URSI General Assembly in Montreal (2018). Previous to this, the SCOSTEP URSI representative was C. J. Rodger (New Zealand). The other Participating Bodies are COSPAR [4], IAGA [5], IAMAS [6], IAU [7], IUPAP [8], SCAR [9], and ISC-WDS [10].

SCOSTEP organizes and conducts international solar-terrestrial physics (STP) programs of finite duration in cooperation with other ICS bodies. They share the results of these programs by joining in conducting meetings, conferences, and workshops, and by publishing newsletters, handbooks, and special journal issues about these solar-terrestrial physics programs. SCOSTEP is an outgrowth of earlier bodies in ICS involved in planning and implementing the International Geophysical Year (lGY: 1957-58) and the International Quiet Sun Year (lQSY: 1964-65). SCOSTEP programs completed to date include:

1976-1979 IMS: International Magnetospheric Study
1979-1981 SMY: Solar Maximum Year
1982-1985 MAP: Middle Atmosphere Program
1990-1997 STEP: Solar-Terrestrial Energy Program
1998-2002 SRAMP: STEP-Results, Applications, and Modeling Phase
1998-2002 PSMOS: Planetary Scale Mesopause Observing System
1998-2002 EPIC: Equatorial Processes Including Coupling
1998-2002 ISCS: International Solar Cycle Study
2004-2008 CAWSES: Climate and Weather of the Sun-Earth System

Figure 1. The PRESTO logo (source: https://scostep.org/presto/).

2009-2013 CAWSES-II: Climate and Weather of the Sun-Earth System-II
2014-2018 VarSITI: Variability of the Sun and its Terrestrial Impact (e.g., [11, 12]).

2. Introducing the PRESTO Program

In 2017, a committee was established by SCOSTEP's Bureau to define the next SCOSTEP program. Since their early deliberations, the committee members and scientists participating in the planning stages identified that predictability of the sun-Earth system from a few hours to centuries was a timely scientific topic. After many in-person exchanges (meetings in Beijing and Bern at the International Space Science Institute) and teleconferences, PRESTO (PREdictability of the variable Solar-Terrestrial cOupling) was conceived. PRESTO is the latest SCOSTEP program, and is expected to cover the 2020-2024 period.

The sun is a variable star and its variability influences the Earth's space environment. Furthermore, changing solar magnetic fields, and radiative and energetic particle fluxes, together force the Earth's atmosphere and climate. Transient energetic events such as flares, coronal-mass ejections (CMEs), interplanetary shocks, stream-interaction regions (SIRs), co-rotating interaction regions (CIRs), and energetic particles adversely impact critical technologies based in space and on Earth upon which our society is increasingly dependent.

At the same time, the middle and upper atmosphere/ionosphere are impacted by processes originating at lower altitudes, e.g., by atmospheric gravity waves, tides and planetary waves, and changes in radiatively active gases. The importance of solar influences on climate is gaining increasing attention, since variations in solar activity not only impact middle-atmosphere chemistry and physics, but have been shown to impact decadal variability at the Earth's surface. This is particularly interesting and important for decadal climate predictions.

With the enhanced understanding of causal connections in the sun-Earth system maturing over the last several decades, fuelled by both observations and theoretical modeling, we are in the position to transform this understanding to produce improved predictions of the sun-Earth coupled system: this is the focus of the current PRESTO program, due to the strong relevance to society.

PRESTO addresses the predictability of: (a) space weather on time scales from seconds to days and months, including processes at the sun, in the heliosphere, and in the Earth's magnetosphere, ionosphere, and atmosphere; (b) sub-seasonal to decadal and centennial variability of the sun-Earth system, with a special focus on climate impacts and a link to the World Climate Research Programme Grand Challenge on Near-Term Climate Predictions as well as the Intergovernmental Panel on Climate Change.

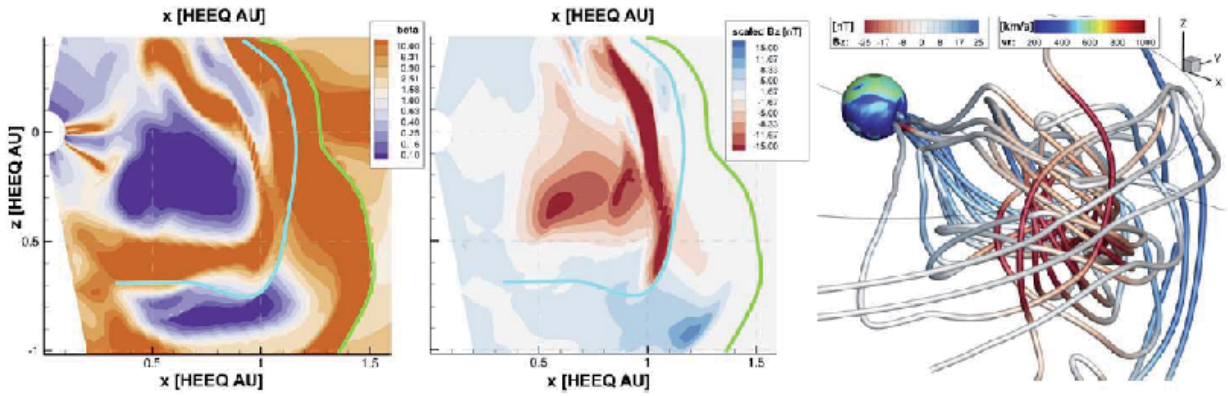

Figure 2. Numerical simulations of three interacting CMEs on 7 September 2017 at 18:00 UT. The lime contour outlines the two first CMEs that merged close to the sun, while the blue contour marks the third CME that reached the previous CMEs further out in interplanetary space (adapted from [13]).

To carry out its objectives, PRESTO activities are divided into three main pillars, i.e.,

Pillar I: Sun, interplanetary space, and geospace
Pillar II: Space weather and Earth's atmosphere
Pillar III: Solar activity and its influence on climate

The PRESTO program is currently led by Ramon E. Lopez (chair, USA); Jie Zhang (co-chair, USA); and Eugene Rozanow (co-chair, Switzerland). Figure 1 shows the PRESTO logo.

3. The PRESTO Pillars

The PRESTO pillars mentioned above span a wide range of fields that overlap with research efforts of many URSI scientists across multiple URSI Commissions. We briefly describe these pillars below and indicate their main science questions.

3.1 Pillar I: Sun, Interplanetary Space, and Geospace

Heliospheric transients originating from the sun, stream-interaction regions (SIRs), fast streams, coronal-mass ejections, as well as solar energetic particles (SEPs) are key agents driving disturbances in geospace. Their formation and evolution, solar wind-magnetospheric coupling, and ensuing magnetospheric dynamics form a complex chain. Accurately predicting and reliably various geospace disturbances, including changes in near-Earth plasma waves and radiation environment, requires understanding the key aspects of related phenomena, physical processes, and their interplay from sun to Earth operating over timescales ranging from milliseconds to days. Despite significant advancements in the field, long-lead-time predictions still require major improvements. For example, there are often significant uncertainties related to corona-mass ejection (CME) parameters and boundary conditions that are fed into the advanced numerical simulations, empirical and semi-empirical forecasting models (see, e.g., Figure 2). Improved physical understanding of their nature and geometry and of the complex interaction properties will also improve predictions.

The main scientific questions in Pillar 1 are: (1) Under what conditions are solar eruptions, CMEs, and SEPs produced, and which indicators of pre-CME and pre-flare activity are reliable? (2) What are the required/critical model input parameters for most successfully forecasting the arrival of SEPs and the geo-effectiveness of CMEs, SIRs, or co-rotating interaction regions (CIRs), and the consequences of the interactions between SIRs/CIRs and CMEs? (3) How are different magnetospheric disturbances and waves (that are critical for the ring current and radiation-belt dynamics) driven by variable solar-wind structures, and/or internal magnetospheric processes?

Pillar I is led by Allison Jaynes (USA), Emilia Kilpua (Finland), and Spiros Patsourakos (Greece).

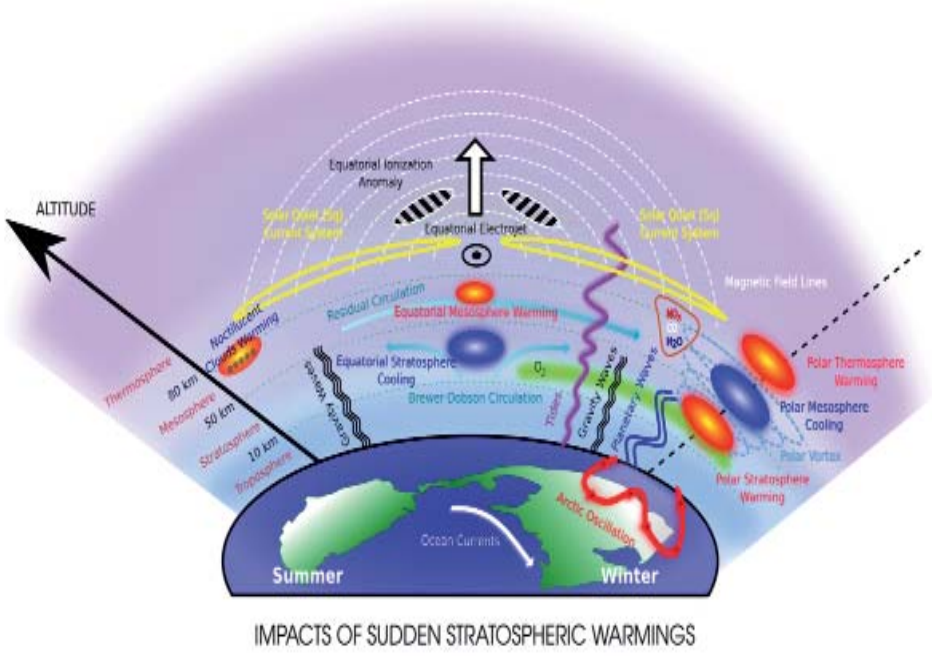

Figure 3. A schematic diagram of whole-atmosphere effects during sudden stratospheric warmings (from [14]).

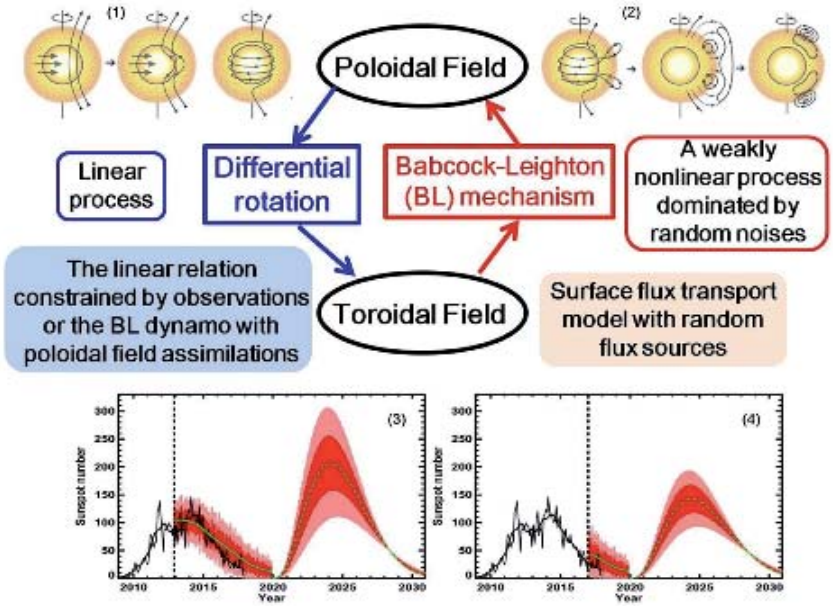

Figure 4. The scheme for the physics-based solar cycle prediction/predictability (adapted from [15]).

3.2 Pillar II: Space Weather and Earth's Atmosphere

The thermosphere and the ionosphere are conventionally known to be directly affected by the varying magnitudes of solar activity. When the incidence of solar flux or energetic charged particles suddenly increases due to the occurrence of solar flares or CMEs combined with magnetic reconnection in the Earth's magnetosphere, the adverse effects witnessed in the ionosphere-thermosphere (IT) system as a whole are referred to as space weather effects. Consequently, these space weather effects lead to adverse effects in several space and ground-based applications. These effects and consequences are to be understood at both fundamental and applications levels.

More recently, it has been recognized that waves originating in the lower atmosphere are an additional important source of ionosphere-thermosphere variability. These waves encompass a vast range of temporal (minutes to weeks) and spatial (few kilometers to global) scales, and introduce a similarly large range of spatial and temporal variability in the ionosphere-thermosphere. Changes in the ionosphere-thermosphere due to wave-driven processes can reach magnitudes similar to moderate geomagnetic storms, illustrating their importance in modifying the ionosphere-thermosphere system. Furthermore, wave-driven processes introduce variability in the entirety of the Earth's atmosphere, as shown in Figure 3, which illustrates the numerous aspects of atmospheric variability that occur in large-scale phenomenon such as in sudden stratospheric warming events.

In order to enhance the predictive capability of the ionosphere-thermosphere spatial and temporal variability, it is necessary to understand how the ionosphere-thermosphere system is affected by both coupling from above and below. Several features that are formed and/or affected due to these effects are plasma irregularities, plasma bubbles, ion-drifts, ionospheric currents, thermospheric densities and composition, neutral winds and waves, etc. These features adversely affect trans-ionospheric radio communication, high-frequency terrestrial radio propagation, and thermal and drag environments for spacecraft in the increasingly congested low-Earth-orbit (LEO, <2000 km) region.

The main scientific questions of Pillar II are: (1) How do the thermosphere and ionosphere respond to various forcing factors from above and from below?; (2) How do atmospheric waves and composition changes impact the middle and upper atmosphere?; (3) What are the magnitude and spectral characteristics of solar and magnetospheric forcing needed for accurate predictions of the atmospheric response? (4) What is the chemical and dynamical response of the middle atmosphere to solar and magnetospheric forcing?

Pillar II is led by Loren C. Chang (Taiwan), Duggirala Pallamraju (India), and Nicholas M. Pedatella (USA).

3.3 Pillar III: Solar Activity and its Influence on Climate

The next five years, spanning the start of Solar Cycle 25 through its (near) peak, provide an excellent opportunity for evaluating our understanding and ability to predict solar activity on decadal time scales. Predictability requires improved understanding of the physical pathways wherein solar variability impacts the atmosphere, from the magnetosphere through the troposphere. The nonlinear

and stochastic mechanisms that modulate the solar cycle and affect the scope of the prediction and predictability of the solar cycle are still open questions. In some areas, decadal-scale solar forcing remains to be quantified to climate-relevant accuracies, which challenge our ability to determine causal connections in the pathways explaining solar forcing impacts on climate (see, e.g., Figure 4). Furthermore, due to wave-driven coupling in the atmosphere, improving predictability of solar forcing also requires improved characterization of the atmosphere-ocean response to the forcing.

The main questions in Pillar III are: (1) How will future solar activity vary over different timescales and what are the physical reasons for the variations?; (2) How will the solar forcing on the Earth's system evolve in the future?; and (3) What is the role of the coupling between atmospheric regions in the realization of the long- and short-term solar influence on the Earth's system, and how are those responses affected by increasing green-house gases?

Pillar III is led by Odele Coddington (USA), Jie Jiang (China), and Stergios Misios (Germany).

4. Relevance to URSI

The breadth of the scientific questions posed in the PRESTO program are relevant to many URSI members. Traditionally, direct SCOSTEP activities have been mainly carried out within URSI Commissions G and H. However, SCOSTEP and PRESTO activities are also indirectly relevant to other Commissions, e.g., A (improvements in electromagnetic remote sensing), B (inverse scattering and imaging), C (radar and navigation systems), D (combined and hybrid photonic and electronic systems for improved solar-terrestrial observations), E (terrestrial and planetary noise of natural origin), F (wave propagation through planetary, neutral atmospheres), J (radio receivers for sun or ionospheric scintillation research) and K (assessment of human exposure to solar electromagnetic fields). As SCOSTEP's role is to provide the framework for international collaboration and dissemination, projects within PRESTO should stimulate more opportunities for URSI researchers to work together. Conferences, workshops, and sessions will be organized and supported around the PRESTO program and the four associated projects. In particular, it is worth noting that PRESTO has funding to provide support for organizing scientific meetings, for international and interdisciplinary campaign activities, and for database construction (see e.g., https://scostep.org/grant-proposals/). As URSI refocuses itself onto its three "core" meetings (URSI GASS, URSI AT-RASC, URSI AP-RASC), the PRESTO funding may assist research communities to support focused workshops during the PRESTO years.

SCOSTEP's role is to also support capacity building for international solar-terrestrial physics research. This has included funding to support training and capacity-building schools. In addition, there is the SCOSTEP Visiting Scholar (SVS) program. The objective of this program is to provide training to young scientists and graduate students from developing countries in well-established solar terrestrial physics laboratories for periods of between one and three months. The aim is to fund between three to six scholars each year. The training will help the young scientists to advance their careers in solar terrestrial physics, using the techniques and skills they learn during the training. We suggest that interested parties should examine the SCOSTEP and PRESTO Web sites for more information.

More detailed information about PRESTO can be found in [16].

5. PRESTO Implementation in a Time of COVID-19

While the VarSITI program was originally scheduled to run from 2014-2018, it effectively continued through to mid-late 2019, at which point closing activities took place, including the VarSITI Closing Symposium (10-14 June 2019, Sofia, Bulgaria). In late 2019, the Chair, co-Chair, and Pillar co-leaders of PRESTO were announced, shortly followed by the first PRESTO newsletter in January 2020. As will be clear to the readers, the PRESTO program started just as COVID-19 became a global pandemic. Much of the operation to date has therefore occurred under COVID restrictions, forcing the SCOSTEP community to adapt.

As readers will surely know, a very significant impact from the pandemic was the imposition of closed international borders and the removal of most work-related travel. This impacted scientific research, stopping field work, collaborative visits, networking, and of course scientific conferences. As one attempt to respond to those difficulties, SCOSTEP/PRESTO hosted a series of online seminars to deliver the latest scientific topics and review presentations on solar-terrestrial physics through the PRESTO Online Seminar Series. This series kicked off in May 2020, and is still continuing at the time of writing with the 11th seminar held in February 2022. The 15th SCOSTEP quadrennial meeting, which was to be hosted in Alibag, India, in late February 2022, was also shifted online. A few exceptions have been PRESTO hybrid sessions with a mix of in-person and online participation at the URSI General Assembly and Scientific Symposium in Rome and the AGU Fall meeting, both of which occurred in 2021.

Of course, not all activities can be run online. The SCOSTEP Visiting Scholar program was delayed. Even in mid-2021, most of the 2020 SVS awardees had not yet started their training programs, with an extension granted up to the end of 2021.

6. References

1. https://council.science

2. https://www.unoosa.org/oosa/en/ourwork/copuos

3. https://www.ursi.org

4. https://cosparhq.cnes.fr

5. http://www.iugg.org/associations/iaga.php

6. http://www.iamas.org

7. https://www.iau.org

8. https://iupap.org

9. http://www.scar.org

10. https://www.icsu-wds.org

11. C. J. Rodger, "SCOSTEP's New Research Program: 'Variability of the Sun and Its Terrestrial Impact (VarSITI),'" *Radio Science Bulletin*, 352, pp. 5-8, 2015.

12. K. Shiokawa, and K. Georgieva, "A Review of the SCOSTEP's 5-Year Scientific Program VarSITI –Variability of the Sun and its Terrestrial Impact, *Prog. Earth Planet. Sci.*, **8**, 21, https://doi.org/10.1186/s40645-021-00410-1, 2021.

13. C. Scolini, E. Chane, M. Temmer, E. K. J. Kilpua, K. Dissauer, A. M. Veronig, E. Palmerio, J. Pomoell, M. Dumbovic, J. Guo, L. Rodriguez, and S. Poedts, "CME-CME Interactions as Sources of CME Geoeffectiveness: The Formation of the Complex Ejecta and Intense Geomagnetic Storm in 2017 Early September," *Astrophys. J. Supp. Series*, **247**, 21, https://doi.org/10.3847/1538-4365/ab6216, 2020.

14. N. M. Pedatella, J. L. Chau, H. Schmidt, L. P. Goncharenko, C. Stolle, K. Hocke, V. L. Harvey, B. Funke, and T. A. Siddiqui, "How Sudden Stratospheric Warming Affects the Whole Atmosphere," *Eos*, **99**, https://doi.org/10.1029/2018EO092441, 2018.

15. O. J. Coddington, J. Jiang, and E. Rozanov, "Pillar 3: Solar Activity and its Influence on Climate," *SCOSTEP/PRESTO Newsletter*, **22**, 6-7, 2020.

16. I. A Daglis, L. C. Chang, S. Dasso, N. Gopalswamy, O. V. Khabarova, E. Kilpua, R. Lopez, D. Marsh, K. Matthes, D. Nandy, A. Seppälä, K. Shiokawa, R. Thiéblemont, and Q. Zong, "Predictability of Variable Solar – Terrestrial Coupling, *Ann. Geophys.*, **39**, pp. 1013-1035, 2021, https://doi.org/10.5194/angeo-39-1013-2021.

Special Issue of the URSI-JRSM 2022 Student Paper Competition

This special issue is a collection of papers by university students who successfully applied for the Student Paper Competition organized at the 2022 URSI-Japan Radio Science Meeting (URSI-JRSM 2022). The conference was held at Chuo University, Tokyo, Japan, on September 1-2, 2022 (http://www.ursi.jp/conference/jrsm2022/).

The URSI-Japan Radio Science Meeting (URSI-JRSM) is a regional URSI conference organized by the Japan National Committee of URSI (JNC-URSI). The URSI-JRSM provides a regional scientific forum for radio scientists and engineers in Japan and the Asian region. The objective of the Meeting is to review current research trends, present new discoveries, and make plans for future research and special projects in all areas of radio science, and a particular emphasis is placed on enhancing the visibility of URSI in the Asian countries and encouraging young scientists to contribute to various URSI activities.

The first URSI-JRSM 2014 was held in Tokyo, Japan on September 8, 2014. A one-day program was organized as plenary sessions with three Keynote Lectures and 10 Invited Talks from the URSI Commissions A-K by outstanding researchers from Japan and Asia. The second URSI-JRSM 2015 was also held in Tokyo, Japan on September 3-4, 2015, where scientific sessions were composed of plenary sessions with two Keynote Lectures, two Special Lectures and 10 Invited Talks from the URSI Commissions A-K, and a Poster Session by contributed papers. The third URSI-JRSM 2019 was again held in Tokyo, Japan on September 5-6, 2019. Scientific programs consisted of plenary sessions with one Keynote Lecture and 10 Invited Lectures from the URSI Commissions A-K, and oral and poster sessions were arranged by each Commission for invited and contributed papers. These conferences were held successfully, each attended with about 200 domestic and international scientists and engineers.

The "2022 URSI-Japan Radio Science Meeting" (URSI-JRSM 2022) was the fourth URSI-JRSM and had the plenary sessions consisting of two Keynote Lectures and 10 Invited Lectures by prominent researchers in the radio science community. Oral Sessions (68 papers) and a poster session (50 papers) were organized by the URSI Commissions A-K for invited and contributed papers. A total of 201 scientists and engineers attended from four countries. This conference was sponsored by The Institute of Electronics, Information and Communication Engineers (IEICE), and technically supported by URSI. It was held in cooperation with Science Council of Japan, Japan Geoscience Union, Society of Atmospheric Electricity of Japan, The Astronomical Society of Japan, The Institute of Electrical Engineers of Japan, The Laser Society of Japan, and The Remote Sensing Society of Japan.

As with the previous URSI-JRSM 2015 and URSI-JRSM 2019, the Student Paper Competition (SPC) was organized in URSI-JRSM 2022 for full-time university students in a degree program, which was financially supported by URSI. A total of nine students applied for the SPC program. On the first day of the conference, September 1, 2022, the URSI-JRSM 2022 SPC Committee selected three SPC finalists based on the applicants' full-length papers and poster presentations. All of the three SPC finalists subsequently presented their papers orally at the SPC Special Session held on the second day of the conference, September 2, 2022. After careful consideration, the URSI-JRSM 2022 SPC Committee decided on the following ranking:

- First Prize: Debrupa Mondal, The University of Electro-Communications, Japan
- Second Prize: Yuji Tanaka, Kanazawa University, Japan
- Third Prize: Yoshihiko Inoue, The University of Tokyo, Japan

The above three winners received prizes (certificates, prize money and supplementary prizes) at the SPC Award Ceremony held during the URSI-JRSM 2022 Closing Ceremony on the second day of the conference. All the three SPC finalists are shown in Figure 1.

Among the three SPC prize winners, we have the following two papers in this special issue of the Radio Science Bulletin:

1. "Thunderstorms and Total Lightning Characteristics Causing Heavy Precipitation in Japan: A Case Study"
   Debrupa Mondal[1], Yasuhide Hobara[1,2], Hiroshi Kikuchi[2], Jeff Lapierre[3]
   [1] Graduate School of Informatics and Engineering, University of Electro-Communications, Japan, [2] Center for Space Science and Radio Engineering, University of Electro-Communications, Japan, [3] Earth Networks, USA
2. "A Bayesian *k*-vector Estimation Method for Electromagnetic Waves in Magnetized Cold Plasma"
   Yuji Tanaka[1], Mamoru Ota[2], Shoya Matsuda[3], Yoshiya Kasahara[3]
   [1] Kyoto University, Japan,[2] National Institute of Technology, Toyama College, Japan,[3] Kanazawa University, Japan

We are pleased that the SPC program at URSI-JRSM 2022 was successful, mainly due to the efforts of the URSI-JRSM 2022 SPC Committee. We feel grateful to the members of the committee for their hard work during the selection process. The financial support from URSI for running the program is greatly acknowledged. Finally, we would like to express our appreciation to the SPC finalists who contributed to this special issue.

Guest Editors:
Satoshi Yagitani, URSI-JRSM 2022 General Chair
Yasuhide Hobara, URSI-JRSM 2022 Technical Program Committee Chair

Figure 1. The URSI-JRSM 2022 SPC finalists. (*from left to right*: Prof. Satoshi Yagitani, URSI-JRSM 2022 General Chair; Debrupa Mondal, SPC First Prize Winner; Yuji Tanaka, SPC Second Prize Winner; Yoshihiko Inoue, SPC Third Prize Winner; Prof. Kazuya Kobayashi, URSI-JRSM 2022 General Co-Chair; Prof. Yasuhide Hobara, URSI-JRSM 2022 Technical Program Committee Chair).

Thunderstorms and Total Lightning Characteristics Causing Heavy Precipitation in Japan : A Case Study

Debrupa Mondal[1], Yasuhide Hobara[1,2], Hiroshi Kikuchi[2], Jeff Lapierre[3]

[1]Graduate School of Informatics and Engineering, University of Electro-Communications, 1-5-1, Chofugaoka, Chofu-shi, Tokyo 182-8585, Japan
E-mail: debrupamondaljam@gmail.com

[2]Center for Space Science and Radio Engineering, University of Electro-Communications

[3]Earth Networks, Germantown, MD 20874, USA

Abstract

We have analyzed an isolated, multicellular thunderstorm event with heavy precipitation (~100 mm/h) that occurred in Saitama, Japan. The X-band multi-parameter radar-derived 3D volume scan and ground-based total lightning data provide detailed spatio-temporal dependences of precipitation cores in different altitudes and associated different types of lightning. We found the development of high altitude (~7-10 km) precipitation core shows a high correlation with the in-cloud lightning rate and the peak of IC lightning occurred 5-10 min prior to subsequent heavy precipitation on the ground. Again, ground precipitation shows a higher correlation with -CG than +CG without significant time lag. Therefore, monitoring total lightning activity during thunderstorms can be useful for nowcasting and short-time prediction of ground precipitation volume.

1. Introduction

The frequency of natural disasters from extreme weather events (heavy precipitation (50mm/h) causing flash floods, storm surges, hurricanes, etc.) is increasing worldwide, including in Japan, due to the faster surface temperature rise (~0.5°C) than the global average (~0.3°C), and scientists predict this long-term trend will continue steadily or may increase [1]. To mitigate the huge destruction associated with such kinds of events, it is important to predict them sufficiently before their occurrence. Many studies showed the Total Lightning (TL) behavior (both In-Cloud (IC) and Cloud-to-Ground (CG)) and its correlation with severe weather such as hail and wind gusts associated with ThunderStorms (TS), tornadoes etc [2,3]. Also, different research groups have investigated spatial distribution trends [4,5], and temporal dependencies [6,7] between lightning and heavy precipitation and found that lightning can act as a precursory parameter of heavy precipitation. Sun *et al* [4], Wang and Liao [5] showed that positive CG flashes occur at the center of the precipitation core and are more in phase with high-level radar reflectivity. Gungle and Kridar [7] showed a linear relationship between the ground Precipitation Volume (PV) and the number of CG flashes and a variable time lag of 5-20 minutes (CG increases before precipitation increases) observed for these warm season storms in Florida.

In the developing stage of a TS, as a result of the strong updraft, IC pulses are produced in the initial stage of cloud electrification and CG flashes are more common in the mature stage of the storm. So, compared to less CG (~30%), a very large number of IC (~70%) as well as TL improves the accuracy of forecasting and warning time [8, 9].

Few research works have been made for the TS events in Japan with heavy precipitation and TL. Ogawa *et al.* (2018) showed a strong positive correlation between the time series of lightning stroke rate from Japanese Total Lightning Network data and ground PV using XRAIN data along with other meteorological parameters but no major time lag between these two was observed [10].

In this paper we have analyzed the overall picture of the development of TS clouds and precipitation cores associated with TSs that produce heavy precipitation (max >100 mm/h) by using TL data and full-volume scan high-speed weather radar data. We have also examined a time lag between the occurrence of lightning activity and

Table 1. XRAIN data specifications

Collected data	Precipitation (mm/h)
Time resolution	1 min
Spatial resolution	250 m
Precipitation resolution	0.1 mm/h
Minimum value	0.1 mm/h
Maximum value	409.0 mm/h

maximum precipitation which could be used for forecast/nowcast purposes for short-duration extreme rainfall events.

2. Data Collection

2.1 eXtended RAdar Information Network (XRAIN)

In this study we have used precipitation data from the Ministry of Land, Infrastructure, Transport, and Tourism's eXtended RAdar Information Network. The network is composed of 26 C-band radars and 39 X-band multiparameter (X-MP) radars which cover most parts of Japan around 14 major cities [11]. The full volume scan data produced by these X-MP radar scanning, are collected to visualize the precipitation core development at a higher altitude in 5-min time resolution. Twelve elevation angles are scanned to produce the 3D data ranging from 0° to 20°. X-band and C-band radar-derived high-resolution (temporal resolution of 1 min, spatial resolution of 250 m) composite ground rainfall intensity data [mm/h] is also collected from XRAIN. The ground rainfall data specifications are summarized in Table 1.

2.2 Japanese Total Lightning Network (JTLN)

TL data associated with the event is collected from JTLN which consists of 11 Earth Networks Total Lightning Sensors (Figure 1) over Japan (data set in 2017, currently 16 stations nationwide) deployed by the University of Electro-Communications and jointly operated with Earth Networks. These sensors can detect lightning pulses in a wide frequency range, ranging from 1 Hz to 12 MHz i.e., extreme low frequency to high frequency range with a spatial resolution of 500 m. TL parameters such as types of lightning (IC and CG), time of occurrence (UT), location (latitude-longitude), and lightning polarity are collected for each lightning discharge.

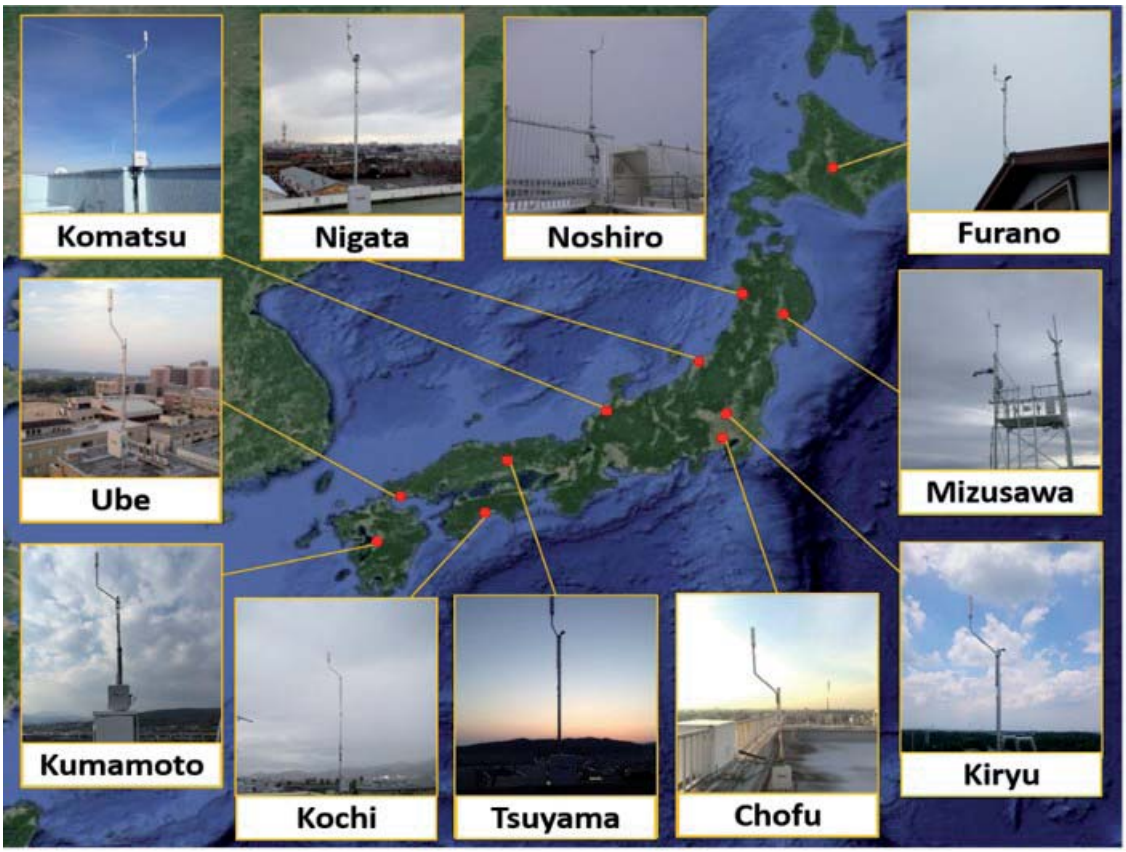

Figure 1. JTLN sensor distribution over Japan.

3. Results

In this paper, the preliminary results from the data analysis of high-resolution 3D volume scan precipitation data and TL activity have been presented. An isolated TS event with heavy precipitation, that occurred in Saitama prefecture and caused flooding of Yanase river on August 30, 2017, is analyzed in detail. During this TS event, the maximum precipitation rate of >100 mm/h (instantaneous value which represents 100 mm of rain would fall in 1 h if the rain rate remained constant) was observed by XRAIN. Depending on the different developmental stages at a particular time, different cells of a smaller spatial scale are considered (multicell TSs).

3.1 Spatio-temporal distribution

From every 5-min full volume scan data of Shinyoko radar (35.5125° E, 139.5994° N), Constant Altitude Plan Position Indicator (CAPPI) plots were produced and

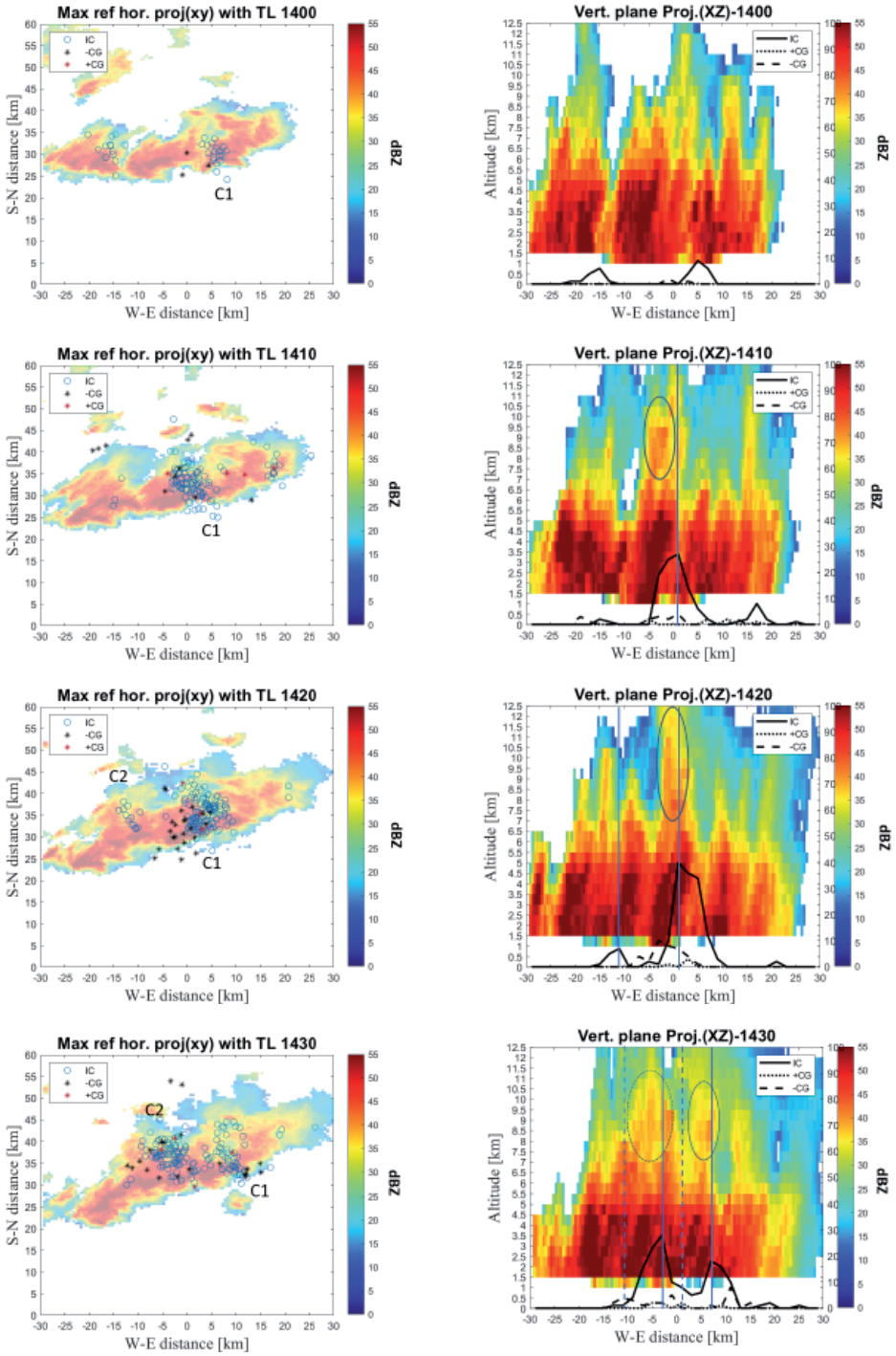

Figure 2. Maximum radar reflectivity projections on horizontal (left panels) and vertical planes (right panels) along with the lightning distributions for the first thirty minutes of the storm starting from 1400 JST.

a smaller area of analysis was selected depending on precipitation cell location. For a detailed analysis with TL distribution, we took maximum radar reflectivity projection both on horizontal (SN-WE) and vertical planes (WE-Altitude) for the selected range. The left panels of each time step in Figure 2 show the maximum radar reflectivity projection on the horizontal plane (for altitude range 0-12 km) with the spatial distribution of IC (blue circle), +CG (red asterisk), -CG (black asterisk) for the first thirty minutes of the TS. The horizontal axis represents the WE distance [km] from the radar location and the vertical axis represents the SN distance [km] from the radar (the radar is located at (0,0)). The right panels of each time step in Figure 2 show the maximum radar reflectivity projection on the vertical (WE-Altitude) plane (for SN range 0-60 km). The lightning data i.e. IC (black solid line), +CG (black dotted line), -CG (black dashed line) flash rate per 5 min for every 2 km of WE range and the SN range of 0-60 km. Observing the distribution of TL, we consider two precipitation cells formation and dissipation during the life cycle of the TS.

The first cell (C1 in Figure 2) started evolving around 14:00 JST (Japan Standard Time) within the 5 km east

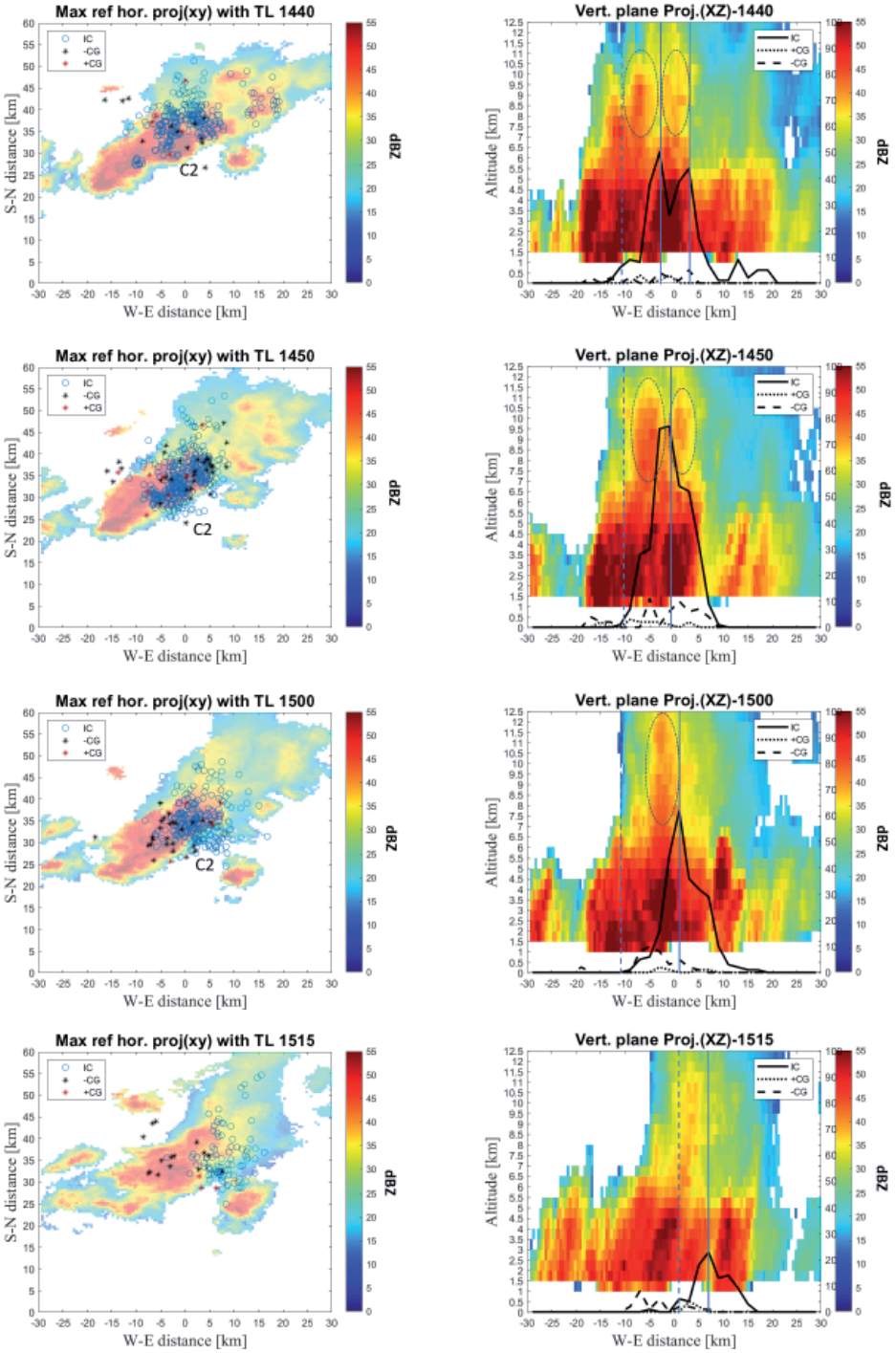

Figure 3. Maximum radar reflectivity projections on horizontal (left panels) and vertical planes (right panels) along with the lightning distribution for the remaining stages of the thunderstorm's life cycle.

of radar location. IC pulses gradually increased from 20 pulses per 5 min at 14:00 JST to 135 pulses per 5 min at 14:20 JST. TS cloud also started developing above 7 km altitude and with an IC lightning jump around 14:10 JST (a rapid increase from 19 pulses to 92 pulses/5 min), a strong core formation (blue circle in Figure 2) was observed at higher altitude (>7 km). This strong core evolved to max height (~12 km) around 14:20 JST when the IC count (135 pulses/5 min) was maximum. Around 14:20 JST few dispersed -CG strokes were observed a bit westward of IC concentration. IC pulses started decreasing gradually after this and started shifting eastward. The precipitation core at high altitudes also started diminishing. Around 14:20 JST, IC pulses also started increasing nearly 10 km west of the radar location and the peak gradually shifted eastward, which is considered as the second cell (C2 in Figure 2 and Figure 3). Simultaneously, TS cells also started evolving above 7 km altitude.

Figure 3 shows the maximum radar reflectivity projections on horizontal (left panels) and vertical planes (right panels) same as in Figure 2 but for the remaining stages of the TS's life cycle. Around 14:40 JST IC distribution is seen to be concentrated in two adjacent locations (2 peaks with consecutive 48 and 42 pulses/5 min in a 2 km range) and two relevant clear precipitation cores (blue dashed circle in Figure 2) were also identifiable in higher altitudes which belongs to second cell i.e. C2. Since C1 already started diminishing around 14:30, only C2 is shown in Figure 3.

After attaining the peak IC at 14:50, these two cores merged and sustained till 15:00 and then gradually started diminishing. IC flash rate also decreased and the peak of IC shifted eastward. The maximum CG (Positive CG + Negative CG) rate was observed around 14:55 (not shown in the figure).

For both the cells of this heavy precipitation event, precipitation cores at higher altitudes (above 7 km) started evolving around 2-4 km west from the peak IC lightning location and gradually migrated towards the peak location. In Figure 2 and Figure 3, the dashed vertical line shows the previous IC peak location and the solid vertical line shows the current IC peak location which also shifts a bit eastward with time. The developed cores faded with the decrease in IC pulses. CG pulses are found to be concentrated in the precipitation core region just before maximum ground precipitation.

Next, we have analyzed the temporal evolution of high altitude and ground PV as well as the TL, IC, and both +CG and -CG rates. Depending on the lightning distribution (or, lightning core area), we selected the area (range of the cell in SN and WE direction) of both the cells with time and calculated the above-mentioned parameters. Figure 4(a) shows the time series of high altitude (7-10 km) PV (solid blue line) and IC (black dashed line) and CG (red dashed line) pulse rates per 5 min for the 2nd cell (C2). The peak of IC (around 350 pulses/5 min) and PV around 7-10 km occurred simultaneously at 14:50 JST, whereas the ground PV peak (blue solid) occurred around 10 min later than the IC peak (black dashed) as shown in Figure 4(b). The peak CG (53 pulses/5 min, red dotted line) was observed 5 min before the peak of the ground precipitation. A similar time delay between rapid IC increase and ground precipitation is also observed for cell 1.

3.2 Correlation between lightning and precipitation

We have carried out a cross-correlation analysis between different lightning rates and PV (normalized cross-correlation between IC rate and high-altitude PV, IC rate and ground PV, CG rate and ground PV for the same time series) during the entire storm period. After cross-correlation, and considering the resultant time lag, the maximum correlation coefficients have been calculated. Figure 5(a) shows the cross-correlation function of IC vs high-altitude PV for the second cell and Figure 5(b) shows the scatter plot and maximum correlation coefficient of the same. Higher altitude PV and IC rate showed a high correlation (correlation coefficient, R=0.95) and no time lag. Similarly, for cell 1, max cross correlation between IC and (7-10km)

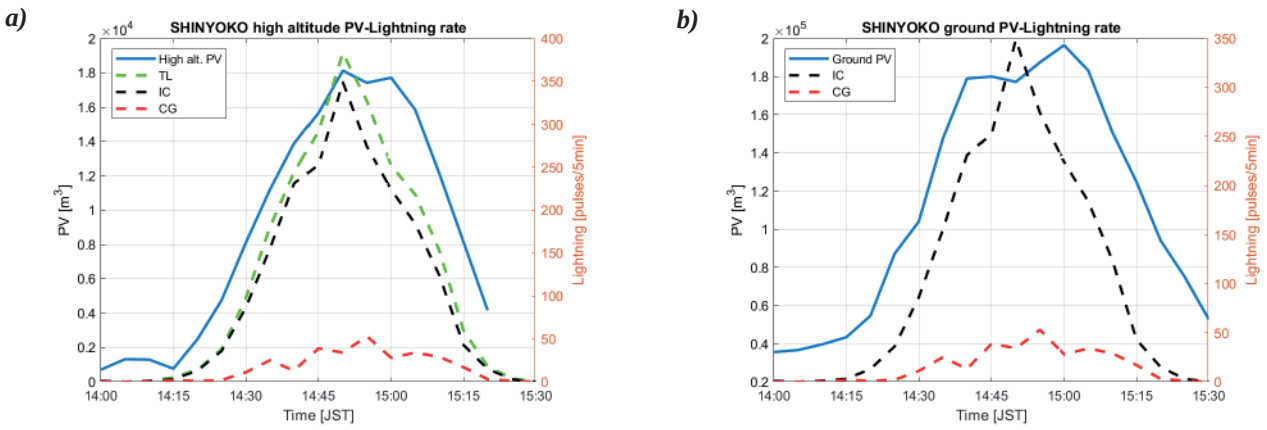

Figure 4. Temporal evolutions of (a) high-altitude PV and TL, IC, CG pulse rates, and (b) ground PV and IC, CG pulse rates.

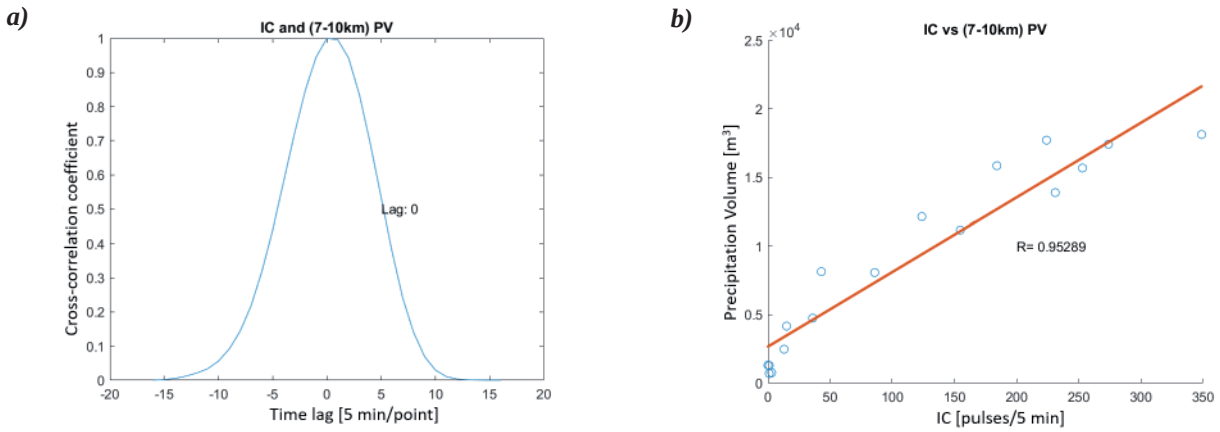

Figure 5. (a) Cross-correlation coefficient between IC and high-altitude PV for cell 2, and (b) relationship between IC [pulses/5min] and high-altitude PV.

PV is observed to be 0.96 (not in figure). These R-values, calculated for individual cells (selected according to the TL distribution) of a smaller spatial scale are significantly higher than the correlation coefficient (0.84) calculated for IC (as well as TL) and ground PV, considering the entire storm in the previous study [10]. Moreover, a positive lag (lag =1 i.e., time lag = 5min) between ground PV and IC rate is also observed which indicates IC pulses are 5 ~ 10 min ahead of ground PV for the entire TS activity. Figure 6(a) represents the cross-correlation function of negative CG vs ground PV and Figure 6(b) shows the scatter plot and maximum correlation coefficient for the same. The ground PV is observed to be more correlated with -CG (R=0.88) than +CG (R=0.75, and the time lag between them is shorter than 5 min. Again, this correlation coefficient value is also much higher than the previous study (for CG and ground rainfall, R = 0.40).

4. Discussion

Yuan and Qie [12] showed a relatively stable relationship and high correlation (>0.7) between ice-phase precipitation (7-11 km) and lightning frequency. Though for the complete storm system, the ground precipitation correlates more with TL [10], the present study showed for individual cells of the same storm system, higher altitude precipitation (7-10 km) correlates more with IC. Instead of considering the entire storm, consideration of a smaller spatial scale (cell scale) and higher altitude precipitation results in significant improvement in the cross-correlation (from 0.84 to 0.95). Rapid intensification of the core at higher altitudes appears with more IC occurrence which indicates greater charge separation, thus strong updraft causing more ice particle collisions during the developing stage of a cell. Liu *et al* [8] showed continuous tracking of TL data, especially IC lightning enables tracking and prediction of different properties of high-impact weather events. For this particular event, consideration of the total storm scale resulted in only 2 min lead time [10], whilst we showed that individually for both the cells, the peak of IC (or, IC lightning jump) occurs nearly 5~10 min earlier than peak ground PV which may be used as a precursory parameter for short-term prediction of maximum ground rainfall. Besides the multicellular nature, we need to consider the correlation of merging-separation between the cells with lightning distribution in the TS life cycle and thus further analysis with more events is required.

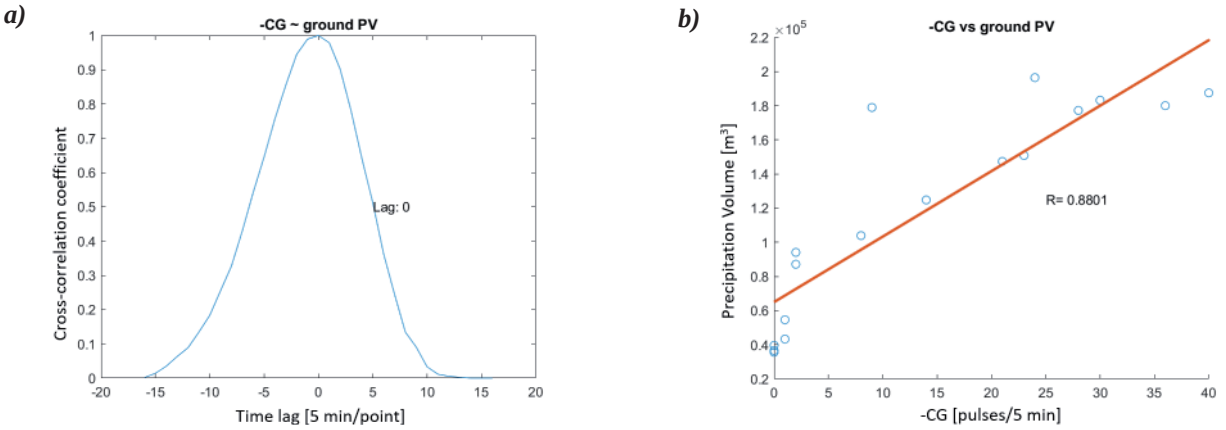

Figure 6. (a) Cross-correlation coefficient between -CG and ground PV for cell 2, and (b) relationship between CG [pulses/5min] and ground PV.

5. Acknowledgments

We acknowledge the support from the Ministry of Education, Culture, Sports, Science, and Technology (AiQuSci Scholarship). The authors are grateful to the Ministry of Land, Infrastructure, Transport and Tourism for providing XRAIN data and also to the KDDI foundation for supporting partially this research project. The authors also thank P. Le Floch and E. DiGangi of EN, Tada Farm, Noshiro City Children's Center, Niigata Science Museum, NAOJ Mizusawa, JAIST, Gunma Univ., Rissho Univ., ISEE (Nagoya Univ.), NIT Tsuyama College, Kochi Univ., Ama town, Yamaguchi Univ., Tokai Univ. for their help JTLN observations in Japan.

6. References

1. Nayak, K. Dairaku, I. Takayabu, A Suzuki-Parker, N. N. Ishizaki, "Extreme Precipitation Linked to Temperature Over Japan: Current Evaluation and Projected Changes With Multi-model Ensemble Downscaling," *Climate Dynamics*, **51**, 2018, pp. 4385–4401.

2. Pineda, J. Bech, T. Rigo, J. Montanyà, "A Mediterranean Nocturnal Heavy Rainfall and Tornadic Event. Part II: Total Lightning Analysis," *Atmospheric Research*, **100**, 2011, pp. 638–648.

3. Farnell, T. Rigo, N. Pineda, "Lightning Jump as A Nowcast Predictor: Application to Severe Weather Events In Catalonia," *Atmospheric Research*, **183**, 2017, pp. 130–141.

4. Sun, J. Chai, L. Leng, G. Xu, "Analysis of Lightning and Precipitation Activities in Three Severe Convective Events Based on Doppler Radar and Microwave Radiometer over the Central China Region," *Atmosphere*, **10**(6), 2019, p. 298

5. Y. Wang, S.A. Liao, "Lightning, Radar Reflectivity, Infrared Brightness Temperature, and Surface Rainfall During The 2–4 July 2004 Severe Convective System Over Taiwan Area," *Journal of Geophysical Research*, **111**, 2006, D05206.

6. Farnell, T. Rigo, "The Lightning Jump Algorithm for Nowcasting Convective Rainfall in Catalonia," *Atmosphere*, **11**(4), 2020, p. 397

7. Gungle, E. P. Krider, "Cloud-to-ground Lightning and Surface Rainfall in Warm-season Florida Thunderstorms," *Journal of Geophysical Research: Atmospheres,* **111**, 2006, D19203

8. Liu, C. Sloop, S. Heckman, "Application of Lightning in Predicting High Impact Weather," OBS/IMO/TECO-2014

9. A. Rakov and M. A. Uman, "*Lightning: Physics and Effects"*, Cambridge: Cambridge University Press, 2003

10. Ogawa, Y. Hobara, H. Iwasaki, S. Heckman, M. Stock, "Statistical Study of The Relationship Between Total Lightning and Heavy Rainfall," 16th International Conference on Atmospheric Electricity, Nara, Japan, 2018

11. T. Maesaka, "Operational Rainfall Estimation by X-band MP Radar Network in MLIT, Japan," Environmental Science, September, 2011

12. T Yuan, X. S. Qie, "Study on Lightning Activity and Precipitation Characteristics Before and After the Onset of The South China Sea Summer Monsoon," *Journal of Geophysical Research*, **113**, 2008, D14101.

A Bayesian k-vector Estimation Method for Electromagnetic Waves in Magnetized Cold Plasma

Yuji Tanaka[1], Mamoru Ota[2], Shoya Matsuda[3], and Yoshiya Kasahara[3]

[1] Division of Electrical Engineering, Graduate School of Engineering, Kyoto University, Kyotodaigaku-Katsura, Nishikyo-ku, Kyoto, Kyoto, Japan; e-mail: tanaka.yuji.2m@kyoto-u.ac.jp

[2] Department of Electrical and Control Systems Engineering, National Institute of Technology, Toyama College, 13 Hongo-machi, Toyama, Toyama, Japan; e-mail: m-ota@nc-toyama.ac.jp

[3] Division of Electrical Engineering and Computer Science, Graduate School of Natural Science and Technology, Kanazawa University, Kakuma, Kanazawa, Ishikawa, Japan; e-mail: matsuda@staff.kanazawa-u.ac.jp; kasahara@staff.kanazawa-u.ac.jp

Abstract

Using the plasma wave characteristics and remote sensing technology, the k-vector direction of plasma waves can provide important information for understanding the global features of space plasma. In this study, we proposed a Bayesian k-vector estimation method in magnetized cold plasma based on the wave distribution function method. The proposed method can be applied to various types of sensors with easy visualization and calculation of the estimation accuracy. We verified the effectiveness of the proposed method through simulations.

1. Introduction

The analysis of plasma waves obtained from in-situ observations through scientific satellites is effective for understanding the physics of near-Earth space and space plasmas in general. To measure plasma waves in bands from a few Hz to several tens of kHz, a scientific satellite is generally equipped with orthogonally aligned dipole antennas and a tri-axis search coil (e.g. [1, 2]). The k-vector direction of plasma waves, through the use of plasma wave characteristics and remote sensing technology, provides key information for understanding the global features of space plasma (e.g. [3]).

The k-vector direction is generally estimated using a spectral matrix, which is the correlation matrix of the electromagnetic field. Ideally, determining the k-vector direction including the absolute direction requires the observation results of at least 5 electromagnetic field components. However, estimation of the k-vector direction is often needed when some sensors are ineffective due to sensor damage or some constraints of the scientific satellites. Moreover, the k-vector direction should be estimated with different sensor noise levels. In addition, the extent of estimation accuracy depends on not only the type of sensors but also the averaging number of the spectral matrix. The extent of estimation accuracy should be calculated to realize the detailed propagation analysis.

In this study, we proposed a Bayesian k-vector estimation method in magnetized cold plasma based on the wave distribution function (WDF) method [4, 5]. By introducing the WDF method and the noise integration kernel (NIK) at different sensor noise levels [6], the proposed method can be applied to various types of sensors. In this study, the proposed method adopts the Bayesian inference under the assumption that the number of arriving quasi-plane waves is 1, and it can visualize, and easily calculate the corresponding estimation accuracy.

2. Bayesian k-vector Estimation Method for Electromagnetic Waves in Magnetized Cold Plasma

Our proposed method can be used to visualize the extent of estimation accuracy by calculating the posterior distribution of each k-vector direction under the assumption that the number of arriving quasi-plane waves is 1.

The observation model of the spectral matrix $S(\omega,\theta,\phi)$ can be expressed as:

$$S(\omega,\theta,\phi)=\varepsilon\Sigma+fa(\omega,\theta,\phi)a^{\mathrm{H}}(\omega,\theta,\phi)\ , \qquad (1)$$

where $\varepsilon\geq 0$ is the noise level, the superscript H represents the complex conjugate transpose symbol, Σ is the NIK based on the ratio of sensor noise levels [6], and $f\geq 0$ is the energy of the arriving waves (WDF), and $a(\omega,\theta,\phi)\in\mathbb{C}^D$ (D is the number of sensors) is the amplitude and phase relation (known as the steering vector [7]) at the direction of arrival (θ,ϕ) with a central angular frequency ω. The effect of cold plasma is included in $a(\omega,\theta,\phi)$ which is uniquely determined from a priori information such as plasma density and background magnetic field intensity.

The proposed method considers the probabilistic model for parameters θ,ϕ,f, and ε and the estimated value of the spectral matrix $\hat{R}$ using the observation signals.The joint probability distribution $p(\hat{R},\varepsilon,f,\theta,\phi)$ can be expressed as:

$$p(\hat{R},\varepsilon,f,\theta,\phi)= \qquad (2)$$

$$p(\hat{R}\mid\varepsilon,f,\theta,\phi)p(\varepsilon\mid\theta,\phi)p(f\mid\theta,\phi)p(\theta)p(\phi),$$

where $p(\hat{R}\mid\varepsilon,f,\theta,\phi)$ $p(\varepsilon\mid\theta,\phi)$, $p(f\mid\theta,\phi)$ $p(\theta)$ and $p(\phi)$ show the likelihood distribution of $\hat{R}$ and the prior distributions of ε , f , θ and ϕ respectively.

From N independent observations $x(\nu\Delta T)\in\mathbb{C}^D$ $(\nu=1,\ldots,N)$ ΔT the sampling period), $\hat{R}$ can be expressed using sample matrix inversion [7] as:

$$\hat{R}=\frac{1}{N}\sum_{\nu=1}^{N}x(\nu\Delta T)x^{\mathrm{H}}(\nu\Delta T). \qquad (3)$$

We set the likelihood distribution of $\hat{R}$ to follow a D-dimensional complex Wishart distribution, with $N(\geq D)$ degrees of freedom as given by:

$$p(\hat{R}\mid\varepsilon,f,\theta,\phi)\propto\frac{\left[\det(\Sigma)\right]^N}{\left[\det(\hat{R})\right]^{N-D}}\cdot$$

$$\frac{\exp\left[-N\cdot\mathrm{tr}\left(\left(\varepsilon\Sigma+fa(\omega,\theta,\phi)a^{\mathrm{H}}(\omega,\theta,\phi)\right)^{-1}\hat{R}\right)\right]}{\varepsilon^{ND}\left[\det\left(I_D+\frac{f}{\varepsilon}\Sigma^{-1}a(\omega,\theta,\phi)a^{\mathrm{H}}(\omega,\theta,\phi)\right)\right]^N}\ , \qquad (4)$$

where $\det(\cdot)$ is the determinant and $\mathrm{tr}(\cdot)$ is the sum of diagonal components (trace) [8, 9].

Our proposed method assumes that $p(\varepsilon\mid\theta,\phi)$ $p(f\mid\theta,\phi)$ $p(\theta)$ and $p(\phi)$ are noninformative priors, and the posterior distribution $p(\theta,\phi\mid\hat{R})$ can be expressed as:

$$p(\theta,\phi\mid\hat{R})\propto\int_0^\infty\int_0^\infty p(\hat{R}\mid\varepsilon,f,\theta,\phi)\,\mathrm{d}f\,\mathrm{d}\varepsilon$$

$$\propto\frac{1}{\eta(\theta,\phi)\,p_{\mathrm{beta}}(r_N(\theta,\phi)\mid N,L_N+1)}\cdot$$

$$\left[1-L_N\sum_{\ell=0}^{N-2}\frac{p_{\mathrm{beta}}(r_N(\theta,\phi)\mid\ell+1,L_N+1)}{(L_N+\ell)(L_N+\ell+1)}\right], \qquad (5)$$

where $\Gamma(\cdot)$ is the Gamma function and

$$\eta(\theta,\phi)=a^{\mathrm{H}}(\omega,\theta,\phi)\Sigma^{-1}a(\omega,\theta,\phi)\ , \qquad (6)$$

$$p_{\mathrm{beta}}(r_N(\theta,\phi)\mid\alpha,\beta)=\frac{\Gamma(\alpha+\beta)}{\Gamma(\alpha)\Gamma(\beta)}r^{\alpha-1}(1-r)^{\beta-1}, \qquad (7)$$

$$r_N(\theta,\phi)=\frac{a^{\mathrm{H}}(\omega,\theta,\phi)\Sigma^{-1}\hat{R}\Sigma^{-1}a(\omega,\theta,\phi)}{\mathrm{tr}(\Sigma^{-1}\hat{R})\cdot\eta(\theta,\phi)}, \qquad (8)$$

$$L_N=N(D-1)-1. \qquad (9)$$

We can see the extent of estimation accuracy visually by checking the posterior distribution $p(\theta,\phi\mid\hat{R})$. We can easily calculate the estimated values of θ and ϕ denoted as $\hat{\theta}$ and $\hat{\phi}$ respectively), which can be expressed as:

$$\hat{\theta}\approx\sum_{m=1}^{M}\theta_m P(\theta_m,\phi_m\mid\hat{R}), \qquad (10)$$

$$\hat{\phi}\approx\sum_{m=1}^{M}\phi_m P(\theta_m,\phi_m\mid\hat{R}), \qquad (11)$$

$$P(\theta_m,\phi_m\mid\hat{R}):=\frac{p(\theta_m,\phi_m\mid\hat{R})}{\sum_{m'=1}^{M}P(\theta_{m'},\phi_{m'}\mid\hat{R})}, \qquad (12)$$

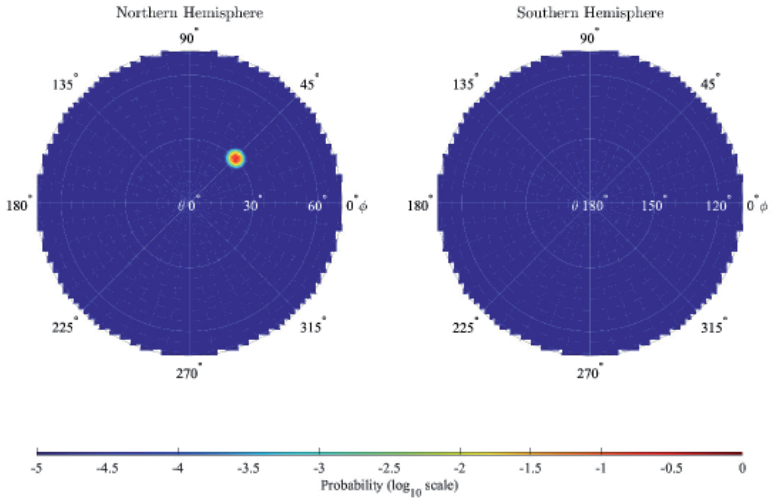

Figure 1: Estimation results of the proposed method with $D=6$ (the electromagnetic field components) and $N=16$

where (θ_m,ϕ_m) (m = 1,…, M) is the discretized direction of arrival, and M is the number of the grids. We can also easily calculate the variances of θ and ϕ denoted as σ_θ^2 and σ_ϕ^2 respectively) by:

$$\sigma_\theta^2 \approx \sum_{m=1}^{M}\left(\theta_m-\hat{\theta}\right)^2 P\left(\theta_m,\phi_m \mid \hat{R}\right), \tag{13}$$

$$\sigma_\phi^2 \approx \sum_{m=1}^{M}\left(\phi_m-\hat{\phi}\right)^2 P\left(\theta_m,\phi_m \mid \hat{R}\right). \tag{14}$$

3. Evaluation through Simulations

We conducted relevant simulations using the spectral matrices estimated from the pseudo-observed signals to simulate different numbers of sensors D and averaging numbers N of the spectral matrix.

3.1 Evaluation Specifications

The pseudo-observed signal was generated as a narrow-band signal with thermal noise. Considering the case where the electromagnetic field sensor is placed in the positive direction of the x-, y- and z- axes, with the z-axis being parallel to the external magnetic field.

The pseudo-observed signal $x(t,\omega)\in\mathbb{C}^D$ can be expressed as:

$$x(t,\omega)=s(t)\,a(\omega,\theta_s,\phi_s)+n(t). \tag{15}$$

Here, $s(t)$ is the complex amplitude in the direction of arrival (θ_s,ϕ_s) following a zero-mean complex Gaussian

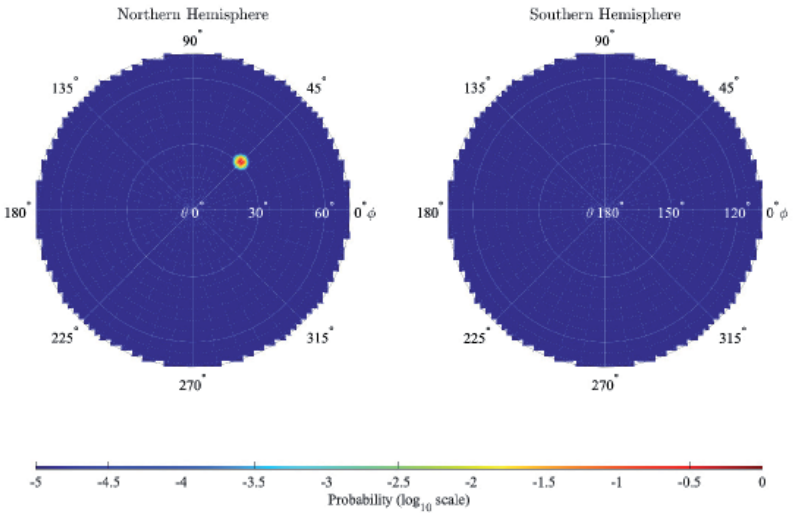

Figure 2: Estimation results of the proposed method with $D=6$ the electromagnetic field components) and $N=32$

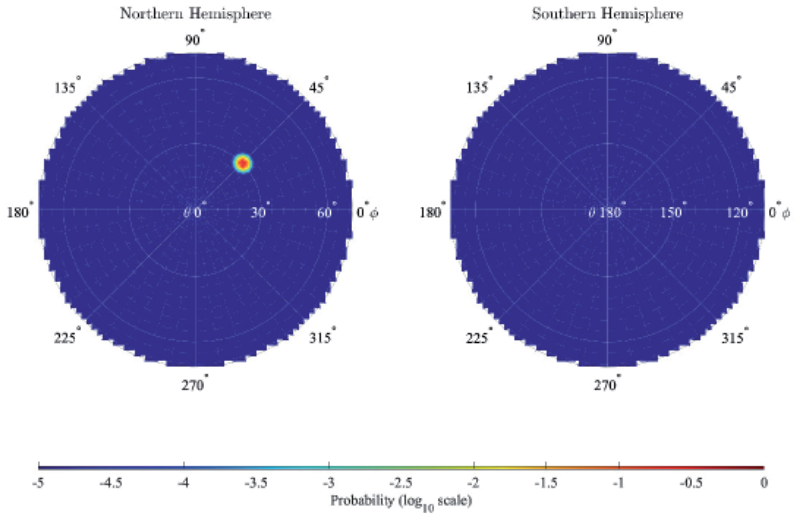

Figure 3: Estimation results of the proposed method with $D=5$ (without the E_z component)

process with a variance of σ_s^2 and $n(t) \in \mathbb{C}^D$ is the thermal noise applied to each channel of the electromagnetic field sensor, following a zero-mean complex Gaussian process with a covariance matrix of εI_D where I_D is the identity matrix of an order of D. We set the direction of arrival θ_s and ϕ_s as 30° and 45° respectively, and set the signal-to-noise ratio (SNR) parameter σ_s^2 / ε as 20 dB. We also assumed that $s(t)$ and $n(t)$ are uncorrelated. The estimated value of the spectral matrix $\hat{R}$ was calculated from Equation (3) using the generated pseudo-observed signal $x(\nu\Delta T, \omega)(\nu = 1, ..., N)$ obtained from Equation (15). To obtain the steering vector $a(\omega, \theta, \phi)$, we set the propagation mode to the R-X mode, the frequency $\omega / 2\pi$ to 1.000 kHz, the plasma frequency to 6.655 kHz, and the cyclotron frequency of electrons to 3.540 kHz. In the simulation setup, the refractive index was 4.8 and the SNR of the electric field and the magnetic field were 7.6 and 19.7 dB, respectively. Then, we used Equation (5) to visualize the extent of estimation accuracy and calculated Equations (10) to (14) by using the calculated $\hat{R}$. We discretized the direction of arrival (θ_m, ϕ_m) $(m = 1,..,M)$ using Appendix A in Tanaka *et. al* [6] with the number of the grids $M = 5,704$.

We conducted simulations with different numbers of sensors including $D=6$ (the electromagnetic field components) and $D=5$ (without E_z or $Z_0 H_z$) where H_z is multiplied by the characteristic impedance of vacuum, denoted as Z_0 in order to convert the dimension of the magnetic field to match that of the electric field. Even when $D=5$, the absolute *k*-vector direction can still be estimated by Faraday's law, but note that the SNR of $Z_0 H_z$ was higher than that of E_z in our simulation setup. We set N as 16 and 32 (two patterns) to check if the extent of estimation accuracy would increase by increasing N.

3.2 Simulation Results

The estimation results of the proposed method can be found in Figures 1 to 4. More specifically, the estimation results of the electromagnetic field components with the averaging number $N=16$ and 32 are shown in Figures 1 and 2, respectively. The electromagnetic field components without E_z and $Z_0 H_z$ are shown in Figures 3 and 4, respectively. The radius of the estimation results represents the zenith angle θ and the circumference angle of the estimation results represents the azimuth angle ϕ. The posterior probability of the proposed method $P(\theta_m, \phi_m \mid \hat{R})$ $(m = 1,\ldots, M)$ is represented by different colors from blue to red. The parameters from Equations (10) to (14) in Figures 1 to 4 are summarized in Table 1.

As shown in Figure 1, it can be found that the peak of $P(\theta_m, \phi_m \mid \hat{R})$ was around the true value $(\theta_s, \phi_s) = (30^\circ, 45^\circ)$,

Table 1: Parameters calculated from Equations (10) to (14)

Specification	$\hat{\theta} \pm \sigma_\theta [^\circ]$	$\hat{\phi} \pm \sigma_\phi [^\circ]$
Case in Figure 1	29.52 ± 1.05	44.01 ± 2.18
Case in Figure 2	30.26 ± 0.62	45.05 ± 1.17
Case in Figure 3	29.68 ± 1.01	44.36 ± 2.08
Case in Figure 4	26.37 ± 2.75	45.75 ± 7.91
True value	30	45

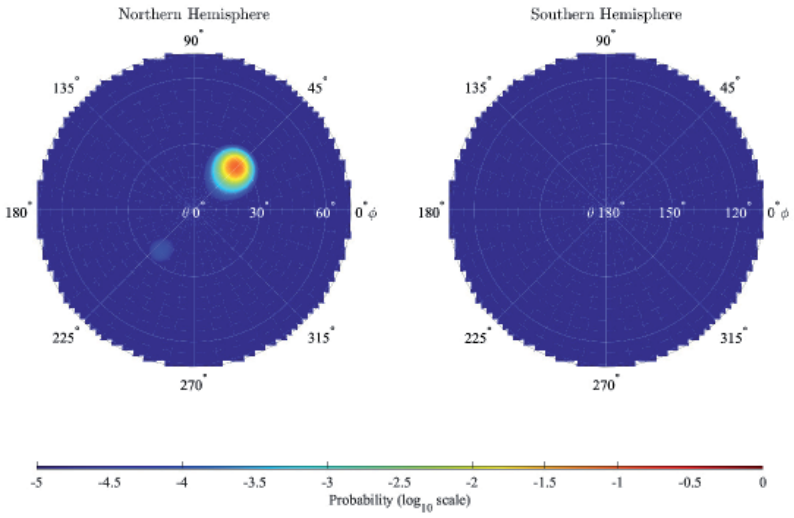

Figure 4: Estimation results of the proposed method with $D=5$ (without the Z_0H_z component) and $N=16$

indicating that the proposed method can correctly visualize the extent of estimation accuracy.

In Figure 2, it was shown that the peak of $P(\theta_m,\phi_m|\hat{R})$ was sharper than that in Figure 1. From Table 1, it was also found that the estimated value $\hat{\theta}$ and $\hat{\phi}$ in Figure 2 improved by 0.2 and 1.0 deg, respectively. Moreover, the standard deviations σ_θ and σ_ϕ in Figure 2 decreased by 0.4 and 1.0 deg, respectively. These findings indicated that when the averaging number *N* increased, the extent of estimation accuracy also increased accordingly.

As shown in Figure 3, it was found that the estimation results were almost the same as those in Figure 1. Comparatively, the peak of $P(\theta_m,\phi_m|\hat{R})$ in Figure 4 demonstrated a broader peak, and the errors of the estimation values and the variances of θ and ϕ were larger, as shown in Table 1. This indicated that the proposed method can demonstrate the importance of Z_0H_z in the simulation setup, as it showed a higher SNR than E_z both visually, and numerically.

4. Summary and Future Work

In this study, we proposed the Bayesian *k*-vector estimation method in magnetized cold plasma based on the WDF method. Our proposed method was found robust under different sensor noise levels since the NIK can estimate *k*-vector direction even when the number of sensors is very few, due to the adoption of the Bayesian inference. We verified that the proposed method can visualize and calculate the extent of estimation accuracy and identify which sensor is important for estimation.

Our future work is to evaluate the proposed method when the noise levels are different among the sensors, or the number of the sensors is less than 5.

5. Acknowledgments

This research was partially supported by the Grant-in-Aid for Scientific Research from the Japan Society for the Promotion of Science (Grant Number: 21H01146). This research was also financially supported by the Support for Pioneering Research Initiated by the Next Generation program by the Japan Science and Technology Agency (Grant Number: JPMJSP2135). The authors would like to thank Enago (www.enago.jp) for the English language review.

6. References

1. C. A. Kletzing, W. S. Kurth, M. Acuna, R. J. MacDowall, R. B. Torbert, T. Averkamp, D. Bodet, S. R. Bounds, M. Chutter, J. Connerney, D. Crawford, J. S. Dolan, R. Dvorsky, G. B. Hospodarsky, J. Howard, V. Jordanova, R. A. Johnson, D. L. Kirchner, B. Mokrzycki, G. Needell, J. Odom, D. Mark, R. Pfaff, J. R. Phillips, C. W. Piker, S. L. Remington, D. Rowland, O. Santolik, R. Schnurr, D. Sheppard, C. W. Smith, R. M. Thorne and J. Tyler, ``The Electric and Magnetic Field Instrument Suite and Integrated Science (EMFISIS) on RBSP,'' *Space Science Reviews*, **179**, 1, November 2013, pp. 127-181.

2. Y. Kasahara, Y. Kasaba, H. Kojima, S. Yagitani, K. Ishisaka, A. Kumamoto, F. Tsuchiya, M. Ozaki, S. Matsuda, T. Imachi, Y. Miyoshi, M. Hikishima, Y. Katoh, M. Ota, M. Shoji, A. Matsuoka and I. Shinohara, ``The Plasma Wave Experiment (PWE) on Board the Arase (ERG) Satellite,'' *Earth, Planets and Space*, **70**, 1, November 2013, pp. 86.

3. O. V. Agapitov, D. Mourenas, A. V. Artemyev, F. S. Mozer, G. Hospodarsky, J. Bonnell and V. Krasnoselskikh, ``Synthetic Empirical Chorus Wave Model from Combined Van Allen Probes and Cluster Statistics,'' *Journal of Geophysical Research: Space Physics*, **123**, 1, January 2018, pp. 297-314.

4. L. R. O. Storey and F. Lefeuvre, ``The Analysis of 6-Component Measurements of a Random Electromagnetic Wave Field in a Magnetoplasma - I. The Direct Problem,'' *Geophysical Journal International*, **56**, 2, February 1979, pp. 255-269.

5. L. R. O. Storey and F. Lefeuvre, ``The Analysis of 6-Component Measurements of a Random Electromagnetic Wave Field in a Magnetoplasma - II. The Integration Kernels,'' *Geophysical Journal International*, **62**, 1, July 1980, pp. 173-194.

6. Y. Tanaka, M. Ota and Y. Kasahara, ``Noise Integration Kernel Design for the Wave Distribution Function Method: Robust Direction Finding With Different Sensor Noise Levels,'' *Radio Science*, **56**, 9, August 2021, pp. e2021RS007291.

7. H. L. Van Trees, *Optimum Array Processing*, New York, United States, Wiley-Interscience, 2002.

8. P. Shaman, ``The Inverted Complex Wishart Distribution and Its Application to Spectral Estimation,'' *Journal of Multivariate Analysis*, **10**, 1, March 1980, pp. 51-59.

9. Y. Tanaka, M. Ota and Y. Kasahara, ``Identification Approach of Arriving Wave Model Based on Likelihood Ratio Test With Different Sensor Noise Levels,'' *Radio Science*, **57**, 8, July 2022, pp. e2022RS007427.

Et Cetera

Tayfun Akgül
Istanbul Technical University
Dept. of Electronics and Communications Engineering
Telecommunications Division
80626 Maslak Istanbul, Turkey
Tel: +90 212 285 3605; Fax: +90 212 285 3565
E-mail: tayfunakgul@itu.edu.tr.

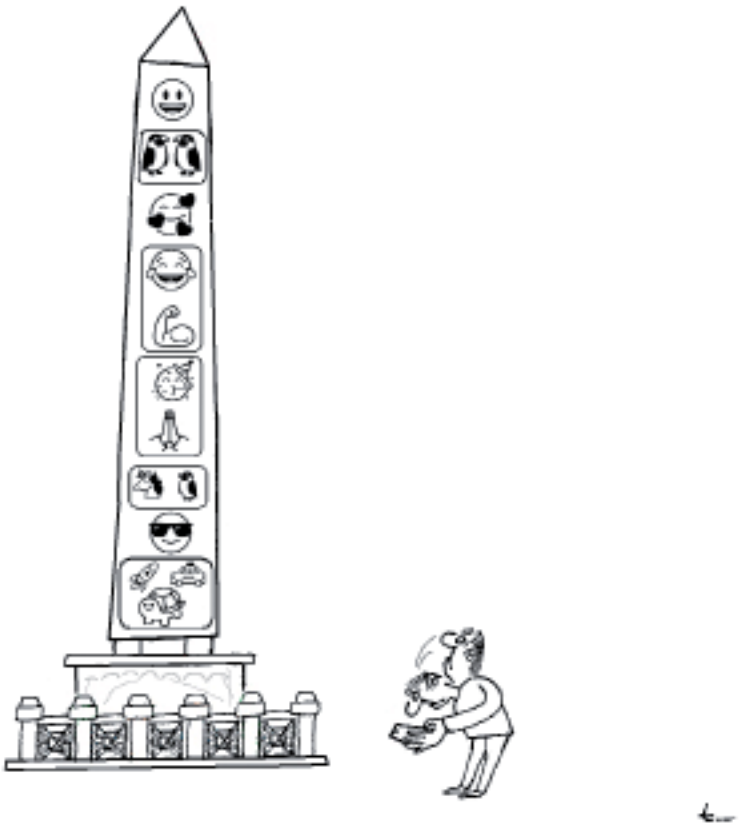

In Memoriam: Dr. Ljiljana R. Cander

Dr. Ljiljana R. Cander suddenly passed away March 16, 2022, after a life devoted and dedicated to science. She was born on June 17, 1946, in Nishka Banja, former Yugoslavia. After moving with her family to Grocka, she was awarded a BSc in Electrical Engineering in 1970, an MSc in Plasma Physics in 1974, and a PhD in Ionospheric Research at Belgrade University in 1984.

She started her scientific career at the Geomagnetic Institute of Grocka, finishing up at the Rutherford Appleton Laboratory (RAL) in the UK, where she spent a great part of her working life. Starting in 1993, she worked in collaboration with the late Peter Bradley in RAL's Radio Communications Research Unit. She became an RAL staff member in 1997, also obtaining British citizenship. She settled to live in Wantage, a small Oxfordshire town where many other RAL staff also lived.

Her principal subjects of interest and research dealt with observation and investigation of the upper atmosphere, particularly connected with the terrestrial ionosphere, its temporal and spatial variability, its medium-term prediction, and forecasting models.

She had one sabbatical year from 1985 to 1986, at Istituto Nazionale di Geofisica in Rome working in traveling ionospheric waves. After that she was extremely active in several European projects, especially a series of ionospheric projects supported by the European Cooperation in Science and Technology (COST) program: the COST 238 PRIME Project (Prediction Retrospective Ionospheric Mapping over Europe); the COST 251 IITS (Improved Quality in Ionospheric Telecommunication); the COST 271 action entitled Effects of Upper Atmosphere on Earth and Satellite Communications as Vice Chair; and finally the COST 296 action entitled MIERS (Mitigation of Ionospheric Effects on Radio Systems) as Chair. She was also active in several space-weather activities sponsored by ESA, in particular the ESA Space Weather Working Team, where she served as spokesperson for the Topical Group on Ionospheric Effects from 2004 to 2007. She brought to these projects an appreciation of the different temperaments and outlooks within a wide-ranging group of European scientists, and helped to foster collaboration between ionospheric radio scientists from so many different countries.

During her time working in RAL's Radio Communications Research Unit, she led a wide range of studies covering ionospheric measurements and forecasting, and the impact of space weather on communications systems. Perhaps most importantly, she was a member of the Ionospheric Expert Team that supported the work of ESA and European industry to understand the critical role of the ionosphere in determining the performance of EGNOS, the satellite-based augmentation system that underpins the accuracy and reliability of GNSS services in Europe. She participated in many international conferences, especially the European Geophysical Union and the International Reference Ionosphere, contributing with relevant original works. She was one of the organizers of the course of the International School of Geophysics on Ionospheric Physics and Propagation, held at the "Ettore Majorana" Foundation and Centre for Scientific Culture in Erice, Italy (September 24-29, 2004). She was also a lecturer of the course on "Ground and Space-Based Instruments for Future Research in Solar-Terrestrial Physics Ground and Space-Based Instruments for Future Research in Solar-Terrestrial Physics," organized by the International School of Space Science at L'Aquila, Italy, on June 6-10, 2016.

Following her nominal retirement in 2006, she retained her affiliation with RAL through a Visiting Scientist appointment, and continued to live and enjoy life in Wantage. She would often visit the RAL site to meet with colleagues, though this became less frequent in later years as her health made it more difficult to visit. Nonetheless, she made great use of the Internet and continued to collaborate with colleagues both at RAL and around the world, right up to her passing in 2022. In fact, her transition to retirement was the most scientifically productive phase of her life, as she published a wealth of papers in refereed journals, and her citation rate rose accordingly. Her professional interests were still on ionospheric studies and applications, including propagation prediction and space weather. Dr.-Ing. Lj. R. Cander was Space Science Editor for Springer's journal *ActaGeofisica*, and a Fellow of the Electromagnetics Academy, USA.

She was co-author of more 200 papers published in the international scientific literature. The last years of her life were mainly dedicated to writing two books. The first one was entitled *Ionospheric Prediction and Forecasting*, and the second one was *Ionospheric for Space Weather*. These have been recently been published by Springer-Verlag.

Finally, she was a cultured woman, loving literature, music, and fine arts, a curious woman loving to travel in Mediterranean countries such as Italy, and in the last times, in Cyprus.

Bruno Zolesi
E-mail: bruno.zolesi@ingv.it

Mike Hapgood
E-mail: mike.hapgood@stfc.ac.uk

In Memoriam: Patricia Doherty

Patricia Doherty, Director and Senior Research Scientist at Boston College's Institute for Scientific Research (ISR), and an internationally recognized leader in space weather and its impact on global navigation systems, died on July 14, 2022. She was 72.

Ms. Doherty joined Boston College and the ISR in 1989 as a Research Scientist. She was named ISR co-Director in 2005. She became the Director in 2008, leading an internationally recognized research center conducting theoretical and experimental studies of space physics, space chemistry, solar-terrestrial research, space weather, and astrophysical studies. She also was a Fellow of the Institute of Navigation (ION) and of the African Geophysical Society.

Ms. Doherty, whose research interests focused on the ionosphere, space weather, and the Global Positioning Satellite System (GPSS), contributed to more than 80 peer-reviewed scholarly articles. Specific research initiatives during her career included radio wave propagation, focusing on ionospheric effects in satellite-based navigation, including satellite-based augmentation systems and the Federal Aviation Administration's Wide-Area Augmentation System.

She was also a leader among the global community of space science researchers. At the time of her death, she was Vice President of the International Union of Radio Science (URSI), and former Chair of URSI's Commission G, Ionospheric Radio and Propagation. She was a past President of the Institute of Navigation and current Chair of the organization's Satellite Division, the world's premier professional society dedicated to the science of positioning, navigation, and timing. She also served as the Scientific Secretary to the Scientific Committee on Solar-Terrestrial Physics (SCOSTEP), an interdisciplinary body of the International Council for Science, was Boston College's representative to the Universities Space Research Association, and was a member of the USRA Board of Trustees. She developed a formal collaboration with the Abdus Salam International Theoretical Center for Physics (ICTP) in Trieste, Italy, to hold annual educational workshops on the applications of GNSS technology for space science, providing opportunities focused on students from developing nations.

Ms. Doherty was recognized for her scientific research and her outreach activities throughout her career, including the 2018 Carrington Education and Outreach Award of the 130,000-member American Geophysical Union. Other honors included ION's Burka Award in 1995, the organization's Distinguished Service Award in 2015, and ION's 2014 Captain P.V.H. Weems Award for her service to the organization and her efforts to promote advanced navigation research throughout the world.

Patricia actively promoted research and education in the science of navigation in developing countries, organizing workshops and conferences around the world. For more than a decade, she lent her expertise to the International Space Weather Initiative (ISWI) community, giving presentations, organizing meetings, and promoting outreach and capacity-building in non-industrialized nations. Since 2019, she served on the ISWI Secretariat as the Meeting Coordinator, and organized and participated in many successful meetings in Asia, Europe, Africa, and both North and South America. It was through ISWI that she discovered a true passion for improving diversity and inclusion in the community, especially advocating for and encouraging women in science and engineering. Combined with her collaboration with ICTP, this activity led to a sustained interest in the education and advancement of young professionals in Africa that earned her the endearing and enduring nickname "Mama Africa" in the African geophysics community.

Those who were fortunate enough to work with Pat know that her scientific, organizational, and administrative skills were exceeded only by her qualities as a human being. She was generous, patient, and caring in her interactions with people and led by character and example. No matter the circumstance, Pat had a smile and kind, encouraging word for everyone. She will be greatly missed by those she left behind, but never forgotten.

Ms. Doherty is survived by her husband, Charles, her children, Karen M. Stickney and Brian J. Doherty, and many other relatives.

To learn more about Pat's amazing journey in her own words as a pathfinder for women in science, please read her short autobiographical sketch, P. H. Doherty, "Oh the Places You Will Go…," *URSI Radio Science Bulletin*, No. 367, December 2018, pp. 22-24, doi: 10.23919/URSIRSB.2018.8627411.

Keith Groves
Boston College
E-mail: keith.groves@bc.edu

In Memoriam: Robert Crane

Robert K. (Bob) Crane passed in Newport, NH, on November 30, 2022, at the age of 86. Nature lover, outdoorsman, history buff, and radio propagation researcher extraordinaire, Bob contributed to the scientific community with a remarkable breadth of experimental and theoretical studies in ionospheric and tropospheric radio propagation, within a variety of professional venues. Among his affiliations were the Mitre Corporation, MIT Lincoln Laboratory, Environmental Research & Technology, Dartmouth College's Thayer School of Engineering, and the University of Oklahoma (where he attained Professor Emeritus status in both electrical engineering and meteorology). Among many professional distinctions, he was an IEEE Life Fellow and a certified consulting meteorologist of the American Meteorological Society.

Bob served for six years as international Chairman of URSI and was an officer of the URSI/US National Committee for fifteen years. He represented the United States numerous times in the Radiocommunication Sector of the International Telecommunication Union (ITU), and was responsible for writing many sections of then in-force ITU Radio Regulations. Bob worked in India under United Nations sponsorship with members of the Indian space program, in Australia on a month-long IEEE lecture tour, and also worked in Peru. Bob wrote two textbooks still used by college students and researchers today: "Electromagnetic Wave Propagation Through Rain" in 1996 and "Propagation Handbook for Wireless Communication System Design" in 2003.

Bob had a unique capability for adapting large existing measurement facilities to pioneering radio propagation research. He monitored low-orbit US Navy navigation satellites with the 46m MIT Millstone Hill radar to estimate the variance and spectra of ionospheric angle-of-arrival and Doppler fluctuations. High-powered L-band and UHF radars at Kwajalein Atoll (Marshall Islands) were applied for high-resolution spatial and velocity observations of winds in the equatorial troposphere. He used other radar observations to analyze transhorizon propagation, rain-scatter interference, and the spatial structure of rainstorms. When adequate facilities did not exist, Bob built his own, such as his famous Rain-Range Experiment. The experimental studies were accompanied with thorough theoretical assessments and modeling to enable practical application of his research results, often in association with detailed subject-area reviews. His contributions to the understanding of propagation through rain are legend.

Because of the scope, high caliber, and longevity of Bob's research, and his participation in such a broad range of venues, Bob influenced and inspired numerous other practitioners in the field. Reminiscences by a few of his many colleagues are shared here.

Dr. David V. Rogers
Communications Research Centre
Canada, Canada (retired)
Dr. Wolfhard J. Vogel
University of Texas, Austin, USA
(retired)

Reminiscences by Colleagues

Back in 1984 I was working for INTELSAT in Washington, DC. Dave Rogers from COMSAT Labs called me one day and said: There is a meeting in Columbia, MD, to discuss propagation experiments with the NASA ACTS satellite – why don't you join in?

This meeting brought together a good number of well-known people doing propagation research in the US at the time. I went there and was introduced to the chairman, Prof. Bob Crane, whose two-component rain model I had already used. I was pleasantly surprised to meet a soft-spoken but well-humored gentleman. His attitude was to encourage discussion and to get all participants to bring in their experience.

Later I attended numerous NAPEX meetings and always enjoyed his presentations and even more his contributions to the discussion. He had moved to the University of Oklahoma and kept working on improved slant-path propagation prediction models – at the same time investigating the requirements for equipment up-time to arrive at valid statistics for rainfall rate and beacon attenuation. I got involved in the work of the propagation Study Group of ITU-R and noticed that Bob Crane's prediction models were considered most reliable and, combined with the rain climatic zones, most universally applicable.

The propagation community is indebted to Bob Crane for his great contributions to understanding the relationship between rain and atmospheric microwave attenuation.,I will always keep Bob in good memories.

Bertram Arbesser-Rastburg
SpaceTec Partners; ESA/ESTEC Electromagnetics &
Space Environment Div. (retired)
Former Chair, ITU-R Study Group 3

I became acquainted with Bob many years ago at a NASA Propagation Experimenters (NAPEX) meeting. This turned into a long-lasting friendship as I started managing the program. From the onset, it was clear that Bob was a world class expert in the field. Bob's contributions to slant path propagation modelling and analysis were numerous, which received ample acknowledgment from his peers. The U.S. satellite industry organizations were heavy users of the NASA Propagation Handbooks during the 80's and 90's and beyond. Since Bob's contributions to these handbooks and the related literature were substantial and high-quality, his name was well known among slant-path propagation enthusiasts.

On the personal note, I have many good memories with Bob, particularly on our ITU trips to Geneva. Bob was very knowledgeable on Switzerland, its geography and points of interest. He took me to most interesting parts of the country and the Swiss Alps; which, without him, I would not have been able to see on my own. I also enjoyed very much working with Bob; in addition to being a great expert in the field, he had good taste and good humor that he liked to share.

Faramaz Davarian
Jet Propulsion Laboratory
NASA Propagation Program
Lunar Communication Terminal

I worked with Bob Crane since my earliest days at NASA and later through the years at various projects. He was a role model for me, one of the few engineers in the country at that time dedicated to radiowave propagation and its effect on communications. I went on to make that the focus for my career also. I remember when Bob was at Environmental Research & Technology and I was a young engineer at NASA Goddard, we funded a program with Bob for propagation research, and Bob developed something later called the Crane Global Model, which became the first propagation model, based on the use of geophysical data, to provide a self-contained rain attenuation prediction procedure for global application. The procedure later evolved into the Crane Two-component Rain Model, which further enhanced rain attenuation prediction. These models served as the basis for many other propagation models over the years and to this day, which further increased our knowledge of radio science and space communications. Bob's legacy is solid, and those of us who had the pleasure of knowing and working with him are better for it.

Louis J. Ippolito
USNC-URSI Commission F
ITU-R Study Group 3

My first interaction with Bob Crane was at the 1975 USNC/URSI meeting in Boulder, CO, as a Communications Research Centre Canada (CRC) postdoc. My paper with Rod Olsen, my CRC mentor into the radio propagation arena, estimated propagation delays in rain to assess any influence on (≈ 14ns) guard-time objectives for TDMA satellite systems. We adopted delay/attenuation ratios to couple rain delay to (better-founded) rain attenuation, which also damped raindrop-size distribution effects, quite cleverly I thought. Bob was not that impressed, noting (correctly) that rain delay is small compared to clear-air delay. Still, dialogue with such an eminent figure was stimulating, and our analysis (with Dan Hodge, Ohio State) of the $A = aR^b$ attenuation-rainrate formalism, introduced at the 1976 Amherst, MA, meeting, had more cachet. Naturally, we leveraged Bob's pioneering work on radio propagation through rain. As our paths continued to intersect, Bob and I became friends. Bob was in Geneva at my first ITU meeting in 1981 to educate me in those initially-perplexing proceedings. For NASA's Advanced Communications Technology Satellite (ACTS) propagation program, Bob and I served as the Working Group chairs, motivating further collaboration and an extraordinary benefit as Bob's coauthor on several papers. It was a privilege to work with such a master.

David V. Rogers
Former Vice-Chair, ITU-R Study Group 3

I met Bob Crane in the early 1970s, as I was starting out to measure the propagation effects of rain over terrestrial and satellite paths at centimeter wavelengths at the University of Texas at Austin. Attending appropriate sessions at URSI and IEEE conferences to learn what others were doing and also to present my own results, Bob often had calm words of encouragement and guidance about the requirements for statistically meaningful data. I always looked forward to having him participating in a session.

Later on, when NASA established the NAPEX (NASA Propagation Experimenters) Group managed through JPL, I got to know Bob on a more personal level. At one of our group meetings, he presented a report on his work and travel in India and it became clear that he very much included his family in his adventures, setting an example for all of us.

After visits to his homes in New Hampshire and Oklahoma, experiencing their organization and ambiance and chatting about his various collections, I realized that Bob had the uncanny ability to see the forest and not just the trees. His love for nature and its variability must have enabled him to create the important holistic propagation models that he is rightfully known for.

Wolfhard Vogel
Former Chair, USNC-URSI Commission F

James C. Lin
University of Illinois at Chicago
851 South Morgan Street, M/C 154
Chicago, IL 60607-7053 USA
E-mail: lin@uic.edu

Research in High-Power Microwave Weapons

James C. Lin

University of Illinois at Chicago
851 S. Morgan St. (M/C 154)
Chicago, IL 60607 USA
E-mail: lin@uic.edu

The incidents of sonic attacks on diplomatic personnel in Havana, Cuba, may likely remain a mystery until some culprit(s) are caught in the act [1]. The one-time diplomatic affair, Havana Syndrome, has apparently transformed into a weapons research program in the United States [2]. Indeed, it appears that research in high-power microwaves has persisted worldwide, including some of the major military powers [3, 4].

An issue that has surfaced concerning the Havana Syndrome involves whether the microwave auditory effect can be exploited as a directed-energy weapon. Indeed, if the microwave auditory effect is weaponized at sufficiently high powers, aside from microwave-pulse-induced sonic attacks, the high-power microwave pulses could produce putative lethal and non-lethal damage to brain tissues by the reverberating sonic shock waves.

A US National Academies of Sciences, Engineering, and Medicine (NASEM) study committee [5] concluded that among the mechanisms the study committee considered, the most plausible mechanism to explain the accounts – especially in individuals with distinct early symptom – appears to be directed, pulsed microwave energy. It reaffirmed the hypothesis first proposed in late 2017 and discussed at the two-day NASEM meeting in early 2020.

Many scientists and researchers, in and outside the US government, are of the thinking that the microwave auditory effect – induced by a targeted beam of high-peak-power pulsed microwave radiation – is the most likely scientific explanation for the Havana Syndrome.

The resilience of the Havana Syndrome and its impact within governmental circles has been amazing. Speculation and hypothesized causes are being vigorously discussed five years since it was first reported. Over that period, about 200 US personnel have reported similar attacks while working in places like Havana, Guangzhou, London, Moscow, Vienna, and Washington, DC, to name a few. There have increasing discussions on the capability of high-power-pulsed microwave radiation as a directed-energy weapon in military operations [5].

Apparently, the US military has maintained some interest in the topic of the microwave auditory effect. Some years ago, the US Navy awarded a research contract entitled "Remote Personnel Incapacitation System" through

its small business innovative research program [6, 7]. The goal of the project was to design and build a prototype non-lethal weapon based on the microwave auditory effect. The transient personnel incapacitation system was dubbed MEDUSA (Mob Excess Deterrent Using Silent Audio). The weapon relied on a combination of pulse parameters and pulse power to raise the auditory sensation to the "discomfort" level to deter personnel from entering a protected perimeter. While the status or outcome of this project may be privileged, there are indications that hardware was built, and power measurements were taken to confirm the required pulse parameters enabling observation of the desired microwave auditory effect, as expected.

It is noteworthy that in December 2020, the US government announced a research program to develop low-cost, low-weight, small-size wearable microwave-weapon-exposure detectors [8]. All indications suggest the research program is currently in progress. Furthermore, the announcement acknowledged that directed-energy weapons, including microwave weapons, are a growing threat to soldiers on the battlefield. It also suggested that the determinants of a microwave weapon's antipersonnel effects are multi-factorial, and associated injuries may be situational dependent. Evidently, there is the conviction that some major military powers possess the capabilities of fielding high-power microwave sources such as those that appear to have been used in Cuba and elsewhere. It appears that the research program has been put into place as advertised. Indeed, there are reports suggesting that research in high-power microwaves continues worldwide, including some of the major military powers.

The recent report from some joint research conducted by the US Air Force and US Army suggests that relevant investigations may be ongoing within their institutions, as well. A computer simulation study showed that for certain high-power microwave-pulse exposures, substantial acoustic pressure may occur within the brain that may have implications for neuropathological consequences [9]. Although the required power densities were high, they were achievable with current high-power commercial and military microwave systems operating under pulsed conditions. Significantly, they were within the permissible limits of currently promulgated safety standards, which confirmed the conclusion of an earlier study [10]. Furthermore, the study showed that to generate tissue-injuring levels of high-power-microwave-induced acoustic pressures inside the human brain, the theoretical microwave-pulse-induced temperature elevation would be no more than 1°C, which is "safe" according to currently promulgated RF and microwave safety protection guidelines [11, 12].

The required microwave technology is mature and in general, commercially available in many developed countries or within major military powers. Longer distances and higher-power scenarios would require more bulky equipment and sophisticated aiming devices, but "packable" equipment is possible for closer-range non-lethal applications [3]. This would not preclude the use of a much-higher-power microwave weapon located at a farther distance from the intended targets to raise the auditory sensation to the "discomfort" levels. Existing hardware could also be optimized to meet some specific requirements in covert or finely targeted operations.

A recent article [2] noted that the US Air Force Research Laboratory (USAFRL) confirmed plans to establish a new center for research into directed energy, such as high-power electromagnetic (including microwave) energy applied to destroy specific targets, in collaboration with the University of New Mexico (UNM). Apparently, UNM has been engaged with the USAFRL on directed-energy microwaves systems for more than 30 years. The new center is in the early planning stages. It is seeded by a $2.4 million, four-year cooperative partnership agreement between UNM and USAFRL. It is expected that the center will go into full operation by 2025. It will enable researchers to study and develop next-generation capabilities in the increasingly competitive directed-energy technology arena.

The program appears to be an integral part of the strategy contained in the US Department of Defense's Directed Energy Futures 2060 report, released in August 2021 [13]. The report defines visions for directed energy and some aspects of electronic warfare with respect to technology development, military utility, and weapons proliferation. The report further mentions that the US is moving aggressively to retain leadership in directed energy, which it describes as focused beams of electromagnetic energy that can be used to disrupt or harm humans, devices, missiles, vehicles, and other targets. It suggests that the technology is less costly than traditional kinetic systems and can result in less collateral damage. It declares that the technologies are approaching or have passed a tipping point for the criticality of directed-energy capabilities as applied to the successful execution of military operations for the United States.

References

1. J. C. Lin, "Mystery of Sonic Health Attacks on Havana-Based Diplomats," URSI *Radio Science Bulletin*, No. 362, September 2017, pp. 102-103.

2. B. Vincent, "Air Force to Build New Center to Study and Enhance Directed Energy Capabilities," NextGov, November 10, 2021 https://www.nextgov.com/emerging-tech/2021/11/air-force-build-new-center-develop-and-study-directed-energy-capabilities/186737/, accessed on November 11, 2021.

3. J. Borger, "Microwave Weapons that Could Cause Havana Syndrome Exist, Experts Say," *The Guardian,* https://www.theguardian.com/science/2021/jun/02/microwave-weapons-havana-syndrome-experts.

4. J. C. Lin, *Auditory Effects of Microwave Radiation*, Springer, Switzerland, September 2021.
5. National Academies of Sciences, Engineering, and Medicine, *An Assessment of Illness in U.S. Government Employees and Their Families at Overseas Embassies*, Washington, DC, The National Academies Press. https://doi.org/10.17226/25889, December 2020.

6. Navy SBIR, "Remote Personnel Incapacitation System," http://www.navysbirprogram.com/NavySearch/Summary/summary.aspx?pk=F5B07D68-1B19-4235-B140-950CE2E19D08, last accessed in August 2020.

7. J. C. Lin, "The Havana Syndrome and Microwave Weapons," *IEEE Microwave Magazine*, **22**, 11, November 2021, pp. 13-14.

8. DHA211-005, "Wearable RF Weapon Exposure Detectors," DoD 2021.1 SBIR Solicitation, https://www.sbir.gov/node/1841633, last accessed on January 15, 2021.

9. A. M. Dagro, J. W. Wilkerson, T. P. Thomas, B. T. Kalinosky, and J. A. Payne "Computational Modeling Investigation of Pulsed High Peak Power Microwaves and the Potential for Traumatic Brain Injury," *Science Advances*, **7**, 44, October 2021, pp. 1-10.

10. J. C. Lin, "Sonic Health Attacks by Pulsed Microwaves in Havana Revisited," *IEEE Microwave Magazine*, **22**, 3, March 2021, pp. 71-73.

11. IEEE, "Standard for Safety Levels with Respect to Human Exposure to Electric, Magnetic, and Electromagnetic Fields, 0 Hz to 300 GHz," (Revision of IEEE Std C95.1-2005/ Incorporates IEEE Std C95.1-2019/ Cor 1-2019), 4 October 2019, pp. 1-312.

12. ICNIRP, "Guidelines for Limiting Exposure to Electromagnetic Fields (100 kHz to 300 GHz)," *Health Phys*., **118**, 5, 2020, pp. 483-524.

13. DOD, "Directed Energy Futures 2060: Visions for the Next 40 Years of U.S. Department of Defense Directed Energy Technologies," Washington DC, August 2021.

Nosherwan Shoaib
Research Institute for Microwave and Millimeter-Wave Studies (RIMMS)
School of Electrical Engineering and Computer Science (SEECS)
National University of Sciences and Technology (NUST)
H-12, Islamabad, Pakistan
E-mail: nosherwan.shoaib@seecs.edu.pk

Recap of Commissions HGE Meet the Experts Session

Conveners: Miroslav Hanzelka (H), Claudia Martinez (H), Bruce Fritz (G), and Chaouki Kasmi (E)

Commission H led a joint session with Commissions E and G at the 2022 AT-AP-RASC meeting entitled "Meet the Experts." The session was designed especially to give early career scientists an opportunity to hear the career perspectives from three established researchers in their respective fields. Each expert gave a 20 minute presentation about their experiences and thoughts on the present state of the field, as well as where the future of the research field is headed. The formal presentations were then followed by an hour of questions from the audience.

The first speaker, Prof. Cathryn Mitchell from the University of Bath, UK, gave a talk titled "From Aberystwyth to Hunga Tonga – Lessons in Ionospheric Imaging." One of her overarching themes was that science often happens in "strides and shuffles." She used three key examples from her career to illustrate the key moments that really catapulted both her and the science forward. From one of her first major publications on ionospheric tomography using GPS receivers, to revelations made as a result of the Halloween 2003 storm, and finally on to the current lessons being learned from the January 2022 Hunga Tonga volcanic eruption, Prof. Mitchell has been able to make the most of these formative moments. She advised the audience to keep learning, even re-reading papers to find new insights, all in an effort to be ready for the next big wave of exciting developments that are bound to come our way.

The second speaker, Prof. Craig Rodger from the University of Otago, NZ, gave a talk titled "Reflections on Current Questions in the Van Allen Radiation Belts, Electron Precipitation, and Space Weather." He used his experience with research in magnetospheric physics to talk about the impacts he sees on everyday society and the critical importance of what we do in our research. Prof. Rodger also advocated for the next generation of science that will be enabled by the proliferation of new technology, perhaps enabled by multi-point measurements from swarms of CubeSats, that could drive upcoming discoveries and innovation in geospace research. Finally, he wrapped up with the observation that good science can be done by anyone from anywhere, and that the best implementation of research often comes from a diverse group of collaborators who can bring a variety of backgrounds.

The third speaker, Dr. Felix Vega from the Technology Innovation Institute in Abu Dhabi, UAE, gave a talk titled "From Plasma Science to High-Power Microwave Engineering." He provided a unique insight into the technology being developed in the field of high-power microwave sources, and how that will help to drive the advances we seek in our research community. Dr. Vega illustrated the wide range of power systems that have been developed over the past 100 years, and the wide range of expertise from different disciplines needed to put together a functioning system. Finally, he foresaw a future where new technology opens up entirely new channels for

geospace research by enabling tools that were not available to generations before.

The Q&A session featured a wide range of insightful questions from the audience to the speakers, including questions that spanned from specific research issues to career planning and the nature of a research-inspired profession. Some highlights of the experts' responses are featured here. First, space weather impacts are a real risk to modern society that are starting to gain more and more attention outside our scientific community. It will be partly our responsibility to both educate the public and then develop the technology to predict/prevent the negative effects on human society. Space weather will in fact be a good way to continue advocating for the large (expensive) missions we rely on for science, but that shouldn't preclude the idea that exploration of our natural geospace environment and solar system is still a fundamentally exciting prospect. Finally, the internal excitement we feel as scientists can be the passion that drives us forward in our careers. It can be hard to plan out a future when opportunities for both funding and scientifically interesting events come and go, but the natural curiosity about whatever interests you have can be a guiding force to help you along the way to take advantage of the opportunities when they present themselves, wherever that may take you. There may be many paths to choose from throughout your career, from academia to industry, and your inherent interest in what you do can help prepare you to maximize whatever opportunities come your way.

All in all, the session was a huge success and we are very grateful to our experts for providing their time and input. We look forward to similar opportunities in the future, and are excited for the 2023 GASS in Sapporo, Japan!

Asta Pellinen-Wannberg
Umeå University, Department of Physics and
Swedish Institute of Space Physics
S-90187 Umeå, Sweden
Tel: +46 90 786 7492
E-mail: asta.pellinen-wannberg@umu.se

Progress within Women in Radio Science - WIRS

This will be my very last WIRS Column in the Radio Science Bulletin. I feel a little bit sad to leave this platform, but I am also happy to see that the work continues in a much broader front such as WIRS Chapters in different countries and WIRS events and sessions on several URSI meetings. Still, we have a lot of work do to.

This time I will give a short summary of what has happened within the WIRS forum at URSI. The WIRS Column started after a dialogue between the Dr Ross Stone, the Editor of the Radio Science Bulletin and me as a quite new Senior Associate Editor on an editorial meeting at the First URSI Atlantic Radio Science Meeting AT-RASC on Gran Canaria in 2015. This situation when Ross told me to do something is very nicely described in the section "Anecdotes and Fun Facts" in Porter et al., [2022].

I thank Ross for all the support and help to the WIRS Column during the years and feel very sorry that Ross is not anymore among us. Together we have profiled about twenty female researchers both active in mid-career and still hard-working retired ones as well as young scientists with babies. Their stories show that the circumstances for doing science vary greatly in different parts of the world. Some female scientists do not even dare to write about their work due to various reasons. Those stories have not been narrated.

I also thank Professor Piergiorgio Uslenghi, the current President of URSI and a wise man, who asked me to organize the first WIRS Workshop at the Second AT-RASC meeting in 2018. The key to make such an event interesting for a broader public than just a few female researchers was to have an attractive presentation. Dr Anthea Coster's talk about how Lise Meitner was helped to escape from Nazi Germany supported by Anthea's grandfather was a success followed by intensive discussions to a glass of wine.

Professor Patricia Doherty was the second female Vice President to be elected in URSI history. We were all very sad to receive the message that she suddenly passed away in July 2022. She had recently been engaged to work towards enhancing the role of women in URSI by encouraging the development of Women in Radio Science Chapters in the member countries. I greatly appreciate Pat for her initiative announced on the International Day of Women and Girls in Science to encourage the formation of WIRS Chapters in URSI member countries. The goal is to promote the work and leadership and provide mentorship to women in all phases of their career in Radio Science. URSI authorized a contribution of 500 € in each triennium for each WIRS Chapter to support their events.

The United States National Committee for the International Union of Radio Science (USNC-URSI) formed the very first WIRS Chapter in 2019. The founding members, activities and social program of the Chapter is presented by its Chair Professor Reyhan Baktur [Baktur, 2020]. WIRS Chapters have now been formed in at least Italy, Poland, Czechia, France, Japan, Egypt, United Kingdom and Sweden.

By today there have been several WIRS events at URSI meetings, even though the Covid pandemic probably disturbed the progress. At URSI-GASS 2021 in Rome there were several sessions, talks and wrap-up, Women's contributions in inverse em problems and a Celebration of Women in Radio Science over the 100 Year History of Commission B. At the AT-AP-RASC 2022 WIRS event on Gran Canaria Jocelyn Bell Burnell gave a talk virtually. During the URSI-GASS 2023 in Sapporo there will be a Tribute to Pat Doherty, WIRS Chapters Workshops, several invited keynote talks and other scientific talks in session marked with W.

I gave an invited General Lecture "The Radio Physics of Meteors: High Resolution Radar Methods Offering New Insights" at the URSI-GASS 2011 in Istanbul. It was a great honour, but I did not understand at that time how unique it was. Afterwards I realized that there has not been many - if any other - ordinary General Lectures given by female researchers at the URSI Flagship Meetings. It cannot be so that I would be the only female scientist worth such a merit to my CV, not even from the statistical point of view. There are many more important topics and several successful female scientists to be invited to give such lectures in fair competition with all others. The current problem might be that there are not enough wise scientists to remember to suggest them.

To reach genuine equal opportunities it is important that younger people see all kind of individuals that look like themselves in different posts. Then every young person can dream of reaching such roles or careers and we do not need to keep such a noise about leaving women outside. I hope that the URSI WIRS Chapters can contribute to improved diversity in Radio Science at all levels by offering mentorship to their members at all stages of their careers. I am also looking forward to seeing more competent women among the URSI Officials.

1. Baktur, R. (2020). Women in Radio Science (WIRS): The Newest Chapter of USNC-URSI, Radio Science Bulletin, 375, 69-74.

2. Porter, E., Quimby, J., Popovic, Z., and Baktur, R., (2022). Finding Kinship in the Women in Radio Science Chapter, IEEE Antennas & Propagation Magazine, *10.1109/MAP.2022.3178670*

Ionospheric effects of the Hunga Tonga Volcanic Eruption of 15 January 2022

Tobias G. W. Verhulst[1], Giorgiana De Franceschi[2], and Claudio Cesaroni[2]

[1] Royal Meteorological Institute of Belgium Geophysical Center
Rue du Centre de Physique 1, 5670 Viroinval, Belgium
E-mail: tobias.verhulst@oma.be

[2] Istituto Nazionale di Geofisica e Vulcanologia, Italy
Via di Vigna Murata 605, 00143 Rome, Italy

During the AT-AP-RASC 2022, a special session was organized dedicated to the ionospheric effects of the exceptional January 2022 eruption of the Hunga volcano in Tonga. This spectacular event is likely of interest to a wider audience within URSI, outside of only the ionospheric research community. We therefore give here an overview of the various contributions presented during this session. Of course, this is only a brief summary, and interested readers are invited to explore the different publications listed among the references for more detailed insights.

1. Introduction

On January 15, 2022, a major eruption took place at the volcano located between the Hunga Tonga and Hunga Ha'apai islands in Tonga, which we will here simply call the "Hunga volcano" [1]. This eruption came after about a month of ongoing activity, and destroyed the land bridge that earlier formed between the two islands [2]. The VEI [volcanic explosivity index] of the eruption was rated as 5, but the explosive energy released was very large for an eruption of this size [3]. This exceptionally powerful explosion was explained by the interaction with sea water, as this was an eruption of a largely submarine volcano. According to different criteria, this was the largest volcanic eruption in terms of explosive power since the 1883 Krakatoa event (see, among others, [4, 5]).

It is well known that large a volcanic eruption can produce wave-like disturbances in the atmosphere propagating up to the height of the ionosphere, above 100 km altitude [6, 7]. Such traveling ionospheric disturbances (TIDs) can be generated through several different physical mechanisms, including shock waves, acoustic waves, Lamb waves, gravity waves, and infrasound, and several of these types of waves can be simultaneously present. Furthermore, a major eruption can also cause other geophysical phenomena such as tropospheric disturbances or, in some cases, tsunamis, which can in turn also affect the ionosphere [7]. The 2022 Hunga volcanic eruption did indeed produce both tsunamis [8] as well as atmospheric pressure waves that traveled around the globe multiple times [9].

This eruption was the most explosive eruption in the era for which ionospheric observations are available, and therefore provides a unique opportunity to study the ionospheric effects of volcanic eruptions in detail.

The URSI AT-AP-RASC conference, held in Gran Canaria from 29 May to 3 June, was to our knowledge the first major meeting were ionospheric observations pertaining to this event could be presented. For this purpose, a special session was organized, chaired by G. De Franceschi and C. Cesaroni, and featuring eight invited contributions. The list of papers presented in this session is given below. Far from being exhaustive, here we provide an overview and summary of the various results discussed in these presentations.

The contributions to the special session were:

- Elvira Astafyeva, "How the 15 January 2022 Hunga Tonga–Hunga Ha'pai Volcano Eruption Shook the Ionosphere" (associated publication [10]).
- Tobias Verhulst, "Multi-Instrument Detection in Europe of Ionospheric Disturbances Caused by the 15 January 2022 Eruption of the Hunga Volcano" [11].
- David Themens, "Global Propagation of Ionospheric Traveling Disturbances Associated with the 2022 Tonga Volcanic Eruption" [12].
- Manuel Hernández-Pajares, "Study of Potential Ionospheric Signatures Associated to 2022 Tonga

Volcano Eruption and Tsunami from LEO- and Ground-Based GNSS Data."

- Angelo de Santis, "A Multi-Parametric and Multi-Platform Approach to Study the Effects in Atmosphere and Ionosphere of the 2022 Hunga Tonga-Hunga Ha'apai Larger Eruptions" [13].

- Boris Maletckii, "Ionospheric Near Real Time Look on Hunga Tonga-Hunga Ha'apai Eruptions via GNSS [14].

- Juha Vierinen, "Ionospheric Perturbations Caused by the Tonga January 2022 Volcanic Eruption" [15].

- Léo Martire, "Real-Time Ionospheric Monitoring of the 2022 Tonga Eruption.

2. Results Presented at the Conference

As the eruption occurred on a remote and uninhabited island, one of the major issues faced in any study relating to it was the paucity of available observations. Even determining the exact onset time of the event was therefore difficult. E. Astafyeva et al. [10] used total-electron-content (TEC) data, obtained from GNSS receivers located on various Pacific islands surrounding the volcano, to reconstruct some of the details of the eruption. They calculated the velocity with which TIDs traveled outward from the volcano, and from this the timing of the eruption was reconstructed. It was demonstrated that there was first a smaller explosion at 04:03 UT, followed at 04:16 UT by two major events, succeeded again by two smaller ones. This was in agreement with the estimation from satellite imagery of the time of the main event, around 04:15 UT.

In related work presented by B. Maletckii, a method was demonstrated that allowed performing such analysis in near-real-time [14]. Because of the unique characteristics of disturbances produced near the site of the volcano, this technique could be employed to continuously monitor the TEC for eruptions. Since TEC observations are available covering most of the globe, this method could be used for early warning and first characterization of eruptions occurring at remote locations where no local monitoring was available. A similar effort was presented by L. Martire, who demonstrated the use of the GUARDIAN early warning system for natural hazards, currently under development by NASA, but soon to be publicly released. This system uses data from a different set of GNSS receivers, but relies on similar principles to detect in near-real time the occurrence of volcanic eruptions, as well as earthquakes and tsunamis, by monitoring disturbances in TEC.

Another interesting observation from Martire's presentation was the detection of a general depletion of the ionospheric plasma in the immediate vicinity of the eruption, in addition to the various waves generated. This was likely associated with the heating and uplift of the entire atmosphere-thermosphere system in this region, but the precise process remains to be investigated.

In both the works of D. Themens et al. [12] and Zhang et al. [15] (the latter presented by J. Vierinen), the TEC was analyzed on a global scale. These papers clearly demonstrated that the eruption generated a spectrum of TIDs with very different characteristics. Close to the site of the eruption, large-scale, likely acoustic waves were seen with speeds over 700 m/s, even up to 1000 m/s. However, these disturbances dissipated within a few thousand kilometers. Lamb wave fronts propagated outwards with speeds between 300 m/s and 350 m/s. These were the waves that circled the globe multiple times, as shown in [15]. Finally, the Lamb wavefront was followed by a train of medium-scale TIDs associated with gravity waves.

Themens' presentation focused on selected regions where dense coverage of GNSS receivers provided high-resolution data. The propagating waves could be tracked moving from one region to the other, with consistent propagation velocities. The work showed by Vierinen took the approach of constructing keograms, showing the disturbance as a function of time since and distance from the eruption, both for the region around the volcano and for the entire globe. The results obtained through both methods were in good agreement. It was confirmed that the ionospheric disturbances encircled the planet at least three times, similar to what was seen in the troposphere.

One of the issues pointed out in Themens' contribution was the anisotropy of the ionospheric disturbances, particularly evident in the large-scale TIDs close to the volcano. M. Hernández-Pajares discussed this aspect further, using TEC measurements from ground stations combined with those from LEO satellites, employing the analysis techniques recently published in [16]. Traditional keograms display disturbances only as a function of radial distance from the source, and therefore are not suitable to analyze anisotropies. In his presentation, Hernández-Pajares therefore showed "North-East-West-South" keograms, depicting the propagation of the disturbances separately by quadrant. This provided additional details on the anisotropic behavior of the TIDs.

A. De Santis presented observations from a wide range of platforms – seismic and magnetic data from ground observatories, ionosonde observation from Australia, and meteorological parameters and TEC from various satellites – and covering a wider area, including some measurements from Europe [13]. This contribution included observations from the period leading up to the major eruption on January 15. For some time before this final cataclysmic eruption, there had been an increase in seismic activity around the volcano as well as intermittent minor eruptions. By investigating the disturbances in satellite measurements during this period, potential signs of an approaching major eruption could be identified.

Finally, the work by T. Verhulst et al. [11] focused on observations of the ionospheric reaction to this event from Europe, the very "far-field" region for this event. Here, far more observations were available than in the region of the volcano itself: there was a dense coverage of GNSS receivers providing TEC data and the area was covered by several ionosonde observatories. This allowed for the detection and tracking of the TIDs as they proceeded to the antipode of the eruption, located in Algeria, followed by a wavefront appearing to emanate from the antipode.

Some of the types of TIDs observed closer to the eruption site dissipated well before reaching Europe. Nevertheless, the combination of ionograms, plasma-drift measurements, TEC data, and in-situ electron-density measurements revealed that several different disturbances were affecting the ionosphere concurrently, even at this distance. Various features were observed in MUF data, electron-density contours, TEC, in-situ electron-density measurements, and plasma drifts, with different data sets not always showing similar features. This was interpreted as different types of waves affecting different observations, showing the importance of combining data from all available platforms to obtain a full picture of the ionosphere's behavior.

3. Conclusions

It is evident from the above that very significant ionospheric disturbances were produced by the eruption of the Hunga volcano. A wide spectrum of traveling disturbances were seen propagating all around the Earth, as well as peculiar features detected in the ionosphere above the volcano, itself.

The contributions to this special session were mostly focused on showing ionospheric observations from various platforms, and how to interpret these as effects of the eruption. In many cases, these observations so far raised more questions than they answered. This is to be expected: eruptions of the scale of the 2020 Hunga volcano eruption are rare, and this event was the first time the ionospheric responses could be observed, certainly in such detail and with decent global coverage.

Some of the open questions were related to associating the signatures in various data sets to particular types of waves, and to specific propagation mechanisms. For instance, the anisotropic propagation of the large-scale disturbances might be due to the influence of the geomagnetic field or the zonal winds, or to a combination of different factors. The disagreement in some cases between measurements from different platforms – e.g., the ionosonde-derived MUF compared to the TEC obtained from GNSS receivers – could be explained by the different measurements being sensitive to, respectively, the secondary waves propagating in the vertical direction or the passing Lamb wavefront moving in the horizontal direction. However, these hypotheses will have to be further investigated before confident conclusions can be drawn. Moreover, far-field observations revealed the small differences in speed and wavelength between the waves propagating along the longer great-circle segment and those traveling along the shorter great-circle segment.

The effects on the ionosphere directly above the volcano also warrant some further attention. Due to the remote location, data from the immediate area were sparse. Nevertheless, a significant depletion was seen of the plasma above the eruption. The precise process responsible for this effect will probably have to be identified by extensive modeling work of the entire atmosphere-thermosphere-ionosphere system in response to a sudden, large injection of energy. Another relevant factor could be the huge amount of water vapor injected into the atmosphere by the submarine eruption affecting the propagation through the lower atmosphere of the GNSS signals used to estimate TEC. In this case, the tropospheric contribution to the geometry-free linear combination of the dual-frequency GNSS signals cannot be considered non-dispersive, as is usually assumed, causing a non-negligible distortion of the estimation of TEC in the region of the volcano.

One aspect of the ionospheric effects of volcanic eruptions that is of particular practical interest is the possibility of using ionospheric monitoring to provide an early warning when such an event occurs. GNSS receivers are nowadays providing TEC observations around the globe, providing coverage also in the region around volcanoes that are not continuously being monitored by other instruments. A mature technology allowing identification in real-time of the signs of major eruptions, and other natural hazards, in TEC data would therefore be very valuable. More difficult, but potentially of major practical use, is the possible detection during the period leading up to the major eruption of peculiar features that could warn of its coming. The real-time detection and possible forecasting of events like this one will be an important area of progress for the new inter-URSI-Commission working group "Risk and Disaster Management."

It is clear that further study of the collected data will be needed to really understand all aspects of this unique event, and serious efforts in modeling and theoretical work will be required before all observations are explained and understood. The scientific community will likely be revisiting this topic for some time to come.

4. References

1. Global Volcanism Program, "Report on Hunga Tonga-Hunga Ha'apai (Tonga)," (A. E. Crafford and E. Venzke, eds.), *Bulletin of the Global Volcanism Network*, **47**, 2, 2022, doi:10.5479/si.GVP.BGVN202202-243040.

2. T. R. Walter and S. Cesca, and the GFZ-DLR-Geomar Task Force Team, "Caldera Subsidence During the Hunga-Tonga Explosive Eruption?," EGU General Assembly 2022, Vienna, Austria, 23-27 May 2022, EGU22-13590, doi:10.5194/egusphere-egu22-13590, 2022.

3. Global Volcanism Program, "Hunga Tonga-Hunga Ha'apai (243040)" in *Volcanoes of the World, v. 4.11.0 (08 Jun 2022)*, E. Venzke (ed.), Smithsonian Institution, 2013, doi:10.5479/si.GVP.VOTW4-2013.

4. J. P. Terry, J. Goff, N. Winspear, et al., "Tonga Volcanic Eruption and Tsunami, January 2022: Globally the Most Significant Opportunity to Observe an Explosive and Tsunamigenic Submarine Eruption Since AD 1883 Krakatau," *Geosci. Lett.*, **9**, 24, June 2022, doi:10.1186/s40562-022-00232-z.

5. J. Vergoz, P. Hupe, C. Listowski et al., "IMS Observations of Infrasound and Acoustic-Gravity Waves Produced by the January 2022 Volcanic Eruption of Hunga, Tonga: A Global Analysis," *Earth Planet. Sci. Lett.*, **591**, August 2022, doi:10.1016/j.epsl.2022.117639.

6. C. Y. Huang, J. F. Helmboldt, J. Park, T. R. Pedersen, and R. Willemann, "Ionospheric Detection of Explosive Events," *Rev. of Geophys.*, **57**, 1, January 2019, doi:10.1029/2017RG000594.

7. E. Astafyeva, "Ionospheric Detection of Natural Hazards," *Rev. of Geoph.*, **57**, 4, December 2019, doi:10.1029/2019RG000668.

8. A. R. Gusman and J. Roger, "Hunga Tonga – Hunga Ha'apai Volcano-Induced Sea Level Oscillations and Tsunami Simulations," GNS Science Web page, accessed at doi:10.21420/DYKJ-RK41, July 2022.

9. Giles Harrison, "Pressure Anomalies from the January 2022 Hunga Tonga-Hunga Ha'apai Eruption," *Weather*, **77**, 3, March 2022, doi:10.1002/wea.4170.

10. E. Astafyeva, B. Maletckii, T. D. Mikesell et al., "The 15 January 2022 Hunga Tonga Eruption History as Inferred From Ionospheric Observations," *Geophys. Res. Lett.*, **49**, 10, May 2022, doi:10.1029/2022GL098827.

11. T. G. W. Verhulst, D. Altadill, V. Barta et al., "Multi-Instrument Detection in Europe of Ionospheric Disturbances Caused by the 15 January 2022 Eruption of the Hunga Volcano," *J. Space Weath. Space Clim.* (under review), preprint: doi:10.1002/essoar.10510837.3.

12. D. R. Themens, C. Watson, N. Žagar et al., "Global Propagation of Ionospheric Disturbances Associated With the 2022 Tonga Volcanic Eruption," *Geophys. Res. Lett.*, **49**, 7, April 2022, doi:10.1029/2022GL098158.

13. S. D'Arcangelo, A. Bonforte, A. De Santis et al., "A Multi-Parametric and Multi-Layer Study to Investigate the Largest 2022 Hunga Tonga-Hunga Ha'apai Eruptions," *Remote Sensing*, **14**, 15, July 2022, doi:10.3390/rs14153649.

14. B. Maletckii and E. Astafyeva, "Near-Real-Time Analysis of the Ionospheric Response to the 15 January 2022 Hunga Tonga-Hunga Ha'apai Volcanic Eruption," *J. Geophys. Res. – Space Phys.* (submitted), preprint: doi:10.1002/essoar.10511373.2.

15. S.-R. Zhang, J. Vierinen, E. Aa et al., "2022 Tonga Volcanic Eruption Induced Global Propagation of Ionospheric Disturbances via Lamb Waves," *Front. Astron. Space Sci.*, **9**, March 2022, doi:10.3389/fspas.2022.871275.

16. H. Yang, M. Hernández-Pajares, W. Jarmołowski, et al., "Systematic Detection of Anomalous Ionospheric Perturbations Above LEOs From GNSS POD Data Including Possible Tsunami Signatures," *IEEE Trans. Geosci. Remote Sens.*, **60**, June 2022, doi:10.1109/TGRS.2022.3182885.

URSI Conference Calendar

Please note that this calendar is updated to the latest version published on the URSI website at http://www.ursi.org/events.php ***(3 October 2023)***

August 2023

URSI GASS 2023
XXXVth URSI General Assembly and Scientific Symposium 2023
Sapporo, Hokkaido, Japan, 19 - 26 August 2023
Contact: URSI Secretariat, c/o INTEC, Tech Lane Ghent Science Park - Campus A, Technologiepark-Zwijnaarde 126, B-9052 Gent, Belgium, E-mail info@ursi.org

11th URSI Turkish 2023 Scientific Congress and National General Assembly Meeting
Istanbul, Turkey, 31 August - 2 September 2023
Contact: Prof. Özlem Ozgun, ursitr23@gmail.com
https://ursitr23.bogazici.edu.tr/

September 2023

XXXVIII Spanish URSI Committee Symposium
Caceres, Spain, 13-15 September 2023
Contact: Secretaría técnica: sevillacongresos@viajeseci.es ; Secretaría científica: ursi2023@unex.es
https://www.ursicaceres2023.com

Kleinheubacher Tagung 2023
Miltenberg, Germany, 26-28 September 2023
Contact: Prof. Frank Gronwald, Department Elektrotechnik und Informatik, Universität Siegen, Hölderlinstr. 3, 57076 Siegen, E-Mail: kh2023@uni-siegen.de
https://kh2023.edas.info/

October 2023

2023 ICEAA-IEEE APWC dual conference
Venice, Italy, 9-13 October 2023
Contact: Prof. Roberto D. Graglia, Chair of Organizing Committee, Dipartimento di Elettronica e TLC, Politecnico di Torino, Corso Duca degli Abruzzi, 24, 10129 Torino, ITALY, roberto.graglia@polito.it ; and Prof. P. L. E. Uslenghi, Chair of Scientific Committee, uslenghi@uic.edu
http://www.iceaa.net/

ISAP 2023 - 2023 IEEE International Symposium on Antennas and Propagation
Kuala Lumpur, Malaysia, 30 October - 2 November 2023
Contact: isap2023@apmttemc.org
https://isap2023.apmttemc.org/

November 2023

2023 IEEE CAMA - Conference on Antenna Measurements and Applications
Genoa, Italy, 15-17 November 2023
Contact: Christian PICHOT, Université Côte d'Azur, CNRS, LEAT, SophiaTech Campus, 930 Route des Colles – BP 145, 06903 Sophia Antipolis Cedex, France, Tél: +33 4 89 15 44 41, Fax: +33 4 89 15 44 79, christian.pichot@univ-cotedazur.fr ; https://2023ieeecama.org/

December 2023

APMC 2023 - Asia-Pacific Microwave Conference 2023
Taipei, China SRS, 5-8 December 2023
Contact: apmc2023secretariat@tl.ntu.edu.tw , https://www.apmc2023.org

March 2024

EuCAP 2024 - 18th European Conference on Antennas and Propagation
Glasgow, Scotland, United Kingdom, 17 - 22 March 2024
Contact: George Goussetis, EuCAP 2024 Conference Chair, email-service@euraap.org ; http://www.eucap.org

April 2024

EUSAR 2024 - European Conference on Synthetic Aperture Radar
Munich, Germany, 23-26 April 2024
Contact: Prof. Madhu Chandra, Technical University Chemnitz, E-mail madhu.chandra@etit.tu-chemnitz.de and nicolas.parisel@vde.com
https://www.eusar.de/en

May 2024

AT-RASC 2024 - 4th URSI Atlantic / Asia-Pacific Radio Science Meeting 2024
Gran Canaria, Spain, 19-24 May 2024
Contact: URSI Secretariat, c/o INTEC, Tech Lane Ghent Science Park - Campus A, Technologiepark-Zwijnaarde 126, B-9052 Gent, Belgium, E-mail at-rasc@ursi.org
https://www.atrasc.com

August 2025

AP-RASC 2025
Asia-Pacific Radio Science Conference 2025
Sydney, Australia, 17-22 August 2025
Contact: Prof. Paul Smith, Macquarie University, Australia, E- mail paul.smith@mq.edu.au

August 2026

URSI GASS 2026
XXXVIth URSI General Assembly and Scientific Symposium 2026
Krakow, Poland, 15 - 22 August 2026
Contact: URSI Secretariat, c/o INTEC, Tech Lane Ghent Science Park - Campus A, Technologiepark-Zwijnaarde 126, B-9052 Gent, Belgium, E-mail: gass@ursi.org URSI-GASS 2026 Secretariat, Symposium Cracoviense, PL31-511 Kraków, Rakowicka 1/14, Tel. +48 12 4227600; E-mail: ursi2026@symposium.pl, https://www.ursi-gass2026.pl

August 2029

URSI GASS 2029
XXXVIIth URSI General Assembly and Scientific Symposium 2029
Singapore, 11 - 18 August 2029
Contact: URSI Secretariat, c/o INTEC, Tech Lane Ghent Science Park - Campus A, Technologiepark-Zwijnaarde 126, B-9052 Gent, Belgium, E-mail: gass@ursi.org

Information for Authors

Content

The *Radio Science Bulletin* is published four times per year by the Radio Science Press on behalf of URSI, the International Union of Radio Science. The content of the *Bulletin* falls into three categories: peer-reviewed scientific papers, correspondence items (short technical notes, letters to the editor, reports on meetings, and reviews), and general and administrative information issued by the URSI Secretariat. Scientific papers may be invited (such as papers in the *Reviews of Radio Science* series, from the Commissions of URSI) or contributed. Papers may include original contributions, but should preferably also be of a sufficiently tutorial or review nature to be of interest to a wide range of radio scientists. The *Radio Science Bulletin* is indexed and abstracted by INSPEC.

Scientific papers are subjected to peer review. The content should be original and should not duplicate information or material that has been previously published (if use is made of previously published material, this must be identified to the Editor at the time of submission). Submission of a manuscript constitutes an implicit statement by the author(s) that it has not been submitted, accepted for publication, published, or copyrighted elsewhere, unless stated differently by the author(s) at time of submission. Accepted material will not be returned unless requested by the author(s) at time of submission.

Submissions

Material submitted for publication in the scientific section of the *Bulletin* should be addressed to the Editor, whereas administrative material is handled directly with the Secretariat. Submission in electronic format according to the instructions below is preferred. There are typically no page charges for contributions following the guidelines. No free reprints are provided.

Style and Format

There are no set limits on the length of papers, but they typically range from three to 15 published pages including figures. The official languages of URSI are French and English: contributions in either language are acceptable. No specific style for the manuscript is required as the final layout of the material is done by the URSI Secretariat. Manuscripts should generally be prepared in one column for printing on one side of the paper, with as little use of automatic formatting features of word processors as possible. A complete style guide for the *Reviews of Radio Science* can be downloaded from http://www.ips.gov.au/IPSHosted/NCRS/reviews/. The style instructions in this can be followed for all other *Bulletin* contributions, as well. The name, affiliation, address, telephone and fax numbers, and e-mail address for all authors must be included with

All papers accepted for publication are subject to editing to provide uniformity of style and clarity of language. The publication schedule does not usually permit providing galleys to the author.

Figure captions should be on a separate page in proper style; see the above guide or any issue for examples. All lettering on figures must be of sufficient size to be at least 9 pt in size after reduction to column width. Each illustration should be identified on the back or at the bottom of the sheet with the figure number and name of author(s). If possible, the figures should also be provided in electronic format. TIF is preferred, although other formats are possible as well: please contact the Editor. Electronic versions of figures *must* be of sufficient resolution to permit good quality in print. As a rough guideline, when sized to column width, line art should have a minimum resolution of 300 dpi; color photographs should have a minimum resolution of 150 dpi with a color depth of 24 bits. 72 dpi images intended for the Web are generally *not* acceptable. Contact the Editor for further information.

Electronic Submission

A version of Microsoft *Word* is the preferred format for submissions. Submissions in versions of T_EX can be accepted in some circumstances: please contact the Editor before submitting. *A paper copy of all electronic submissions must be mailed to the Editor, including originals of all figures.* Please do *not* include figures in the same file as the text of a contribution. Electronic files can be send to the Editor in three ways: (1) By sending a floppy diskette or CD-R; (2) By attachment to an e-mail message to the Editor (the maximum size for attachments *after* MIME encoding is about 7 MB); (3) By e-mailing the Editor instructions for downloading the material from an ftp site.

Review Process

The review process usually requires about three months. Authors may be asked to modify the manuscript if it is not accepted in its original form. The elapsed time between receipt of a manuscript and publication is usually less than twelve months.

Copyright

Submission of a contribution to the *Radio Science Bulletin* will be interpreted as assignment and release of copyright and any and all other rights to the Radio Science Press, acting as agent and trustee for URSI. Submission for publication implicitly indicates the author(s) agreement with such assignment, and certification that publication will not violate any other copyrights or other rights associated with the submitted material.

Become An Individual Member of URSI

The URSI Board of Officers is pleased to announce the establishment of categories of individual membership of URSI. The purpose of individual membership of URSI is to secure professional recognition of individual radioscientists and to establish their better connection with the URSI Board of Officers, Scientific Commissions, and URSI Member Committees. Three categories of individual membership (URSI Corresponding Member, URSI Senior Member and URSI Fellow) have been established.

URSI Corresponding Membership is the first step into the URSI community and provides:

- Access to the proceedings of URSI Flagship Conferences via the Web site
- Notifications of new editions of URSI publications.

In addition, URSI Senior Members and URSI Fellows benefit from the following:

- Reduced registration fees at URSI Flagship Meetings.
- Reduced registration fees at some meetings organized by partnering organizations such as (but not limited to) IEEE AP-S and EuCAP.
- A page charge reduction from 175 USD to 150 USD for papers published in the URSI journal, Radio Science Letters.
- An invitation to receive their individual membership certificate at an URSI Flagship meeting.

Fellowship is by invitation only; Senior Membership can be by invitation or application. Corresponding Membership is a streamlined, instant process. Details, and an online application for URSI Senior Membership, are available at http://www.ursi.org/membership.php#tab-sectionA1.